united nations
educational, scientific
and cultural
organization

international atomic
energy agency

the
abdus salam
international centre for theoretical physics

SMR 1273 - 8

WORKSHOP ON PLASMA DIAGNOSTICS AND INDUSTRIAL APPLICATIONS OF PLASMAS

12 - 13 OCTOBER 2000

INDUSTRIAL APPLICATIONS OF SMALL PLASMA DEVISES AND RELATED DIAGNOSTICS

Background Information

Jorge FEUGEAS
Rosario Institute of Physics (IFIR)
Bv. 27 de Febrero 210 Bis.
2000 Rosario, Argentina

Surface and Coatings Technology, 70 (1995) 191–195

Changes in the elasticity modulus and mechanical dynamical spectroscopy of nitrogen and argon implanted copper

O. A. Lambri, G. Sánchez and J. Feugeas*

Instituto de Física Rosario (CONICET-UNR), Bv. 27 de Febrero 210 bis, 2000 Rosario (Argentina)

F. Povolo

Comisión Nacional de Energía Atómica, Departamento de Materiales, Av. del Libertador 8250, Buenos Aires (Argentina)

Abstract

The effect of pulsed ion implantation of nitrogen and argon on copper was studied by means of mechanical dynamical spectroscopy.

A new peak of internal friction at about 800 K (grain boundary relaxation), which is not present in unimplanted samples, was found only in nitrogen ion implanted cases.

Nevertheless, a strong increase in the shear modulus was found in the same manner for ion implanted samples with both species of ions.

1. Introduction

Mechanical dynamic spectroscopy (MDS) is one of the important nonmicroscopic techniques used to study defects and their interactions in materials. The method is based on the fact that the presence of the defect causes a local strain which couples to an externally applied stress, giving rise to the observed internal friction. The characteristic temperature dependence of the internal friction, arising from the thermally activated motion of defects, gives information on the parameters characterizing this motion.

Furthermore, the dependence of the elastic modulus on the temperature can be determined simultaneously with the internal friction. This technique has been applied successfully to the study of interstitial and substitutional diffusion, dislocation damping, dislocation-point defect interaction and grain boundary motion [1,2].

Above room temperature, copper may present three peaks of internal friction related to the grain boundary relaxation: low, intermediate and high temperature peaks. The temperature of each one is, approximately, 500, 750 and 1000 K respectively [3]. Furthermore, other peaks at lower temperatures related to the induced stress ordering can be found.

The existence of the latter two of the three peaks mentioned above depends on the heat treatment, the type of structure and the presence of substitutional atoms whereas the first one is always present [3].

In this work we are using the mechanical dynamical spectroscopy technique to study pulsed ion implantation effects on grain boundary motion and elastic shear modulus behavior in copper.

2. Experimental details

2.1. Pulsed ion implantation process

The pulsed ion implantation process is carried out using a dense plasma focus (DPF) [4,5]. It consists of a cylindrical coaxial plasma gun, closed at one end (with a Pyrex insulator between the electrodes) and open at the other end. The interelectrodic space is filled with the working gas (nitrogen, hydrogen, argon, etc.) at low pressure (approx. 300 mTorr).

For ion beam acceleration, an electric discharge is produced between the electrodes, and a pulsed ion beam is obtained. The electric energy (approx. 1 kJ) stored in a capacitor bank is discharged on the electrode system through a spark gap switch. The discharge parameters (gas pressure, charge voltage, etc.) are adjusted to produce the breakdown on the insulator surface. The breakdown generates a current sheath which is composed of electrons and filling gas ions. By interacting with its own magnetic field, the current sheath is accelerated toward the open end of the electrodes, where it collapses as a DPF (1 mm diameter and approx. 4 mm length plasma column) in front of the center electrode. In this region the ion beams are accelerated as a result of the development of the Rayleigh Taylor instability. The total time elapsed from the moment the discharge is produced until

*Author to whom correspondence should be addressed.

0257-8972/95/$9.50
SSDI 0257-8972(94)02271-Q

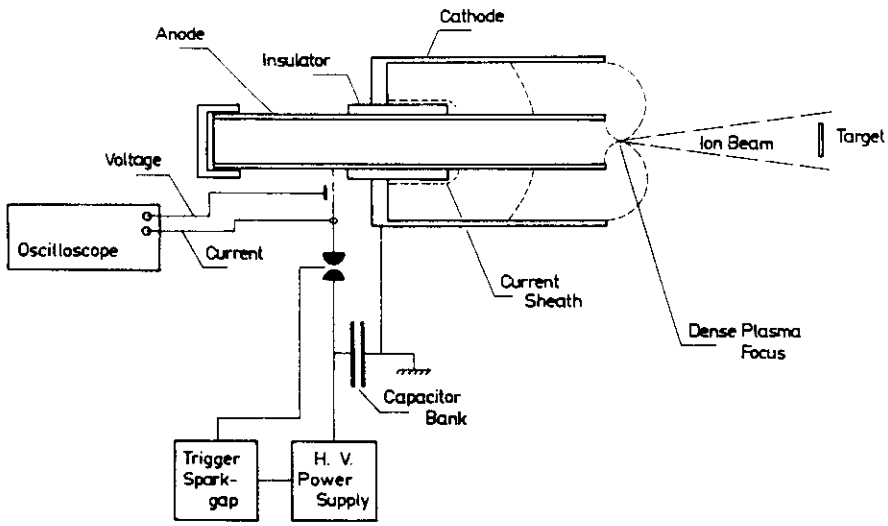

Fig. 1. Pulsed ion implanter.

the acceleration is ended is about 0.8 μs and the ion beam acceleration process lasts about 200 ns. For implantation purposes the target is placed at a distance l in front of the electrodes.

The ion beams have conic geometry with a solid angle of about 40° [6]. The temporal width of an ion beam depends on the distance l focus–target, and can be adjusted between 250 and 500 ns.

The number of ions generated in the DPF is 1×10^{15}, and the fluence at the target position depends on the distance l and can be calculated as

$$f = \frac{1 \times 10^{15}}{\sigma_l} \tag{1}$$

where σ_l is the cross-section of the beam at a distance l from the focus and can be calculated as

$$\sigma_l = \pi(l \tan 20°)^2 \tag{2}$$

Higher fluences are obtained by accumulation of a number n of successive pulses, being the total accumulated fluence $F = nf$.

The beam consists of ions with energy enclosed in a continuous spectrum from 20 keV up to several megaelectronvolts. In the range 20–500 keV the spectral law [7] is

$$\frac{dN}{dE} \propto E^{-3.4} \tag{3}$$

During the interaction of this ion beam with the material target, a fast energy deliverance (high amount of energy in a short time) is produced. As a consequence, high thermal gradients (1000–1500 K μm^{-1} [8,9]), high heating (5–15 K ns^{-1} [8,9]) and cooling rates are developed into the surface layer of the target. Owing to the ion penetration into the targets (range) a thin surface layer of about 1 μm is thermally affected.

2.2. Torsion pendulum of variable moment of inertia

Figure 2 illustrates schematically the torsion pendulum with a variable moment of inertia. It is essentially a traditional torsion pendulum of the inverted type, with some modifications: (a) there are two inertial arms instead of one; (b) the position of the masses in the lower inertial arms, E, can be changed by means of the stepper motor M, the wires H, and the spring K. In fact,

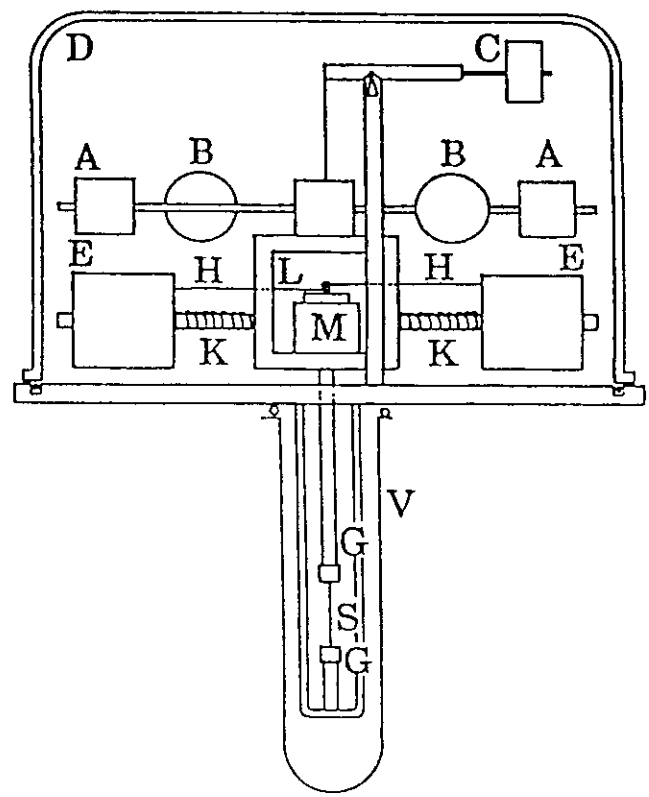

Fig. 2. Torsion pendulum of variable moment of inertia.

by a rotation of M in one sense, the wires H wind up in two small pulleys located on the axis of the motor in such a way that the masses E slide symmetrically toward the axis of the pendulum, compressing the springs K. A rotation of M in the other direction releases the spring which consequently pushes the masses E away from the axis of the pendulum. Then, by acting on M from outside the pendulum, it is possible to change the moment of inertia of the lower arms and to correct the changes in the oscillation frequency with temperature, produced by changes in the shear modulus of the specimen fixed by the grips G, and located in the lower part of the pendulum. The excitation coils B are located in the upper arms and the internal friction and the frequency can be determined, in free decay, sustained and forced oscillations, by recording the oscillations with a normal optical system, including a mirror and a photodiode. L is the main frame which supports the inertial arms, the stepper motor C is a compensation weight that avoids axial stresses on the specimen, and D and V are vacuum chambers which allow measurements in high vacuum. The temperature of the specimen is changed by means of a furnace located around the vacuum chamber V.

The four-arm configuration of the torsion pendulum allows a greater variation in the moment of inertia and consequently a wider correction of the oscillation frequency, according to the material to be tested and the geometry of the specimen.

Finally, the influence of the connecting wire to the stepper motor on the oscillation frequency and on the internal friction was studied carefully. It was concluded that this connecting wire did not influence the results, for the usual values measured in metals and alloys. The influence will be even lower in the case of polymers.

Also, the possibility of measuring at high and low temperatures under turbomolecular pump vacuum up to 10^{-7} Torr [10] is available.

The device is driven by an automatic data acquisition system [11].

2.3. Sample treatment

The samples were made of electrolytic high purity (99.99%) polycrystalline copper, in sheet shape (30 mm × 4.5 mm × 0.3 mm). The internal stress was relieved under two different conditions: (i) annealing condition I: 2 h, 1073 K, 10^{-3} Torr; (ii) annealing condition II: 1 h, 1073 K, 10^{-4} Torr.

Twelve samples were implanted with different total fluences F: (i) implantation condition A: nitrogen—$F = 1 \times 10^{15}$ ions cm^{-2}; (ii) implantation condition B: nitrogen—$F = 2 \times 10^{15}$ ions cm^{-2}; (iii) implantation condition C: argon—$F = 1 \times 10^{15}$ ions cm^{-2}. The fluence F was reached by the accumulation of single beams with fluence $f = 10^{13}$ ions cm^{-2} and 500 ns of pulse.

The twelve samples were tested as indicated in Table 1.

TABLE 1. Sample treatments

No. of samples	Annealing condition	Implanted/ unimplanted	Implantation condition
2	I	U	-
2	I	I	A
2	II	U	-
2	II	I	A
2	II	I	B
2	II	I	C

The MDS measurements were performed under high vacuum in the free decay method through a data acquisition system, increasing the temperature at a rate of 0.5 K min^{-1} in the range 300–1130 K. The natural frequency at room temperature was approx. 0.6 s^{-1}. The maximum shear strain was 4×10^{-5}.

3. Results

Figure 3 shows the MDS spectrum for samples treated under the annealing condition I for the implanted (implantation condition A) and the unimplanted cases.

The internal friction spectrum (IFS) is plotted in curves (a) and (b) for unimplanted and implanted samples respectively. Curves (c) and (d) show the temperature dependence of the shear modulus for unimplanted and implanted samples respectively.

In curve (b) a peak can be seen at about 800 K, not reported in the literature and not present in unimplanted sample measurements (curve (a)). Also an increase in the high temperature background with respect to curve (a) is present in curve (b) (out of range in the plot of Fig. 3).

In the implanted sample, the shear modulus is on average 10% greater than the unimplanted sample.

The measurement results of samples annealed under

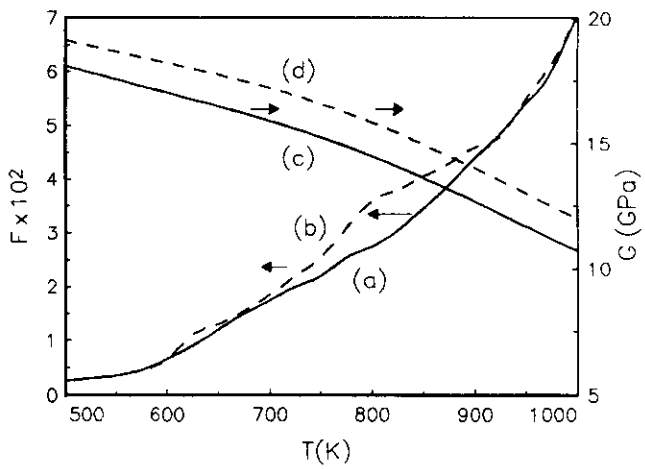

Fig. 3. MDS for implanted samples (1×10^{15} ions cm^{-2}) and unimplanted ones. Annealing condition: 2 h, 1073 K, 10^{-3} Torr.

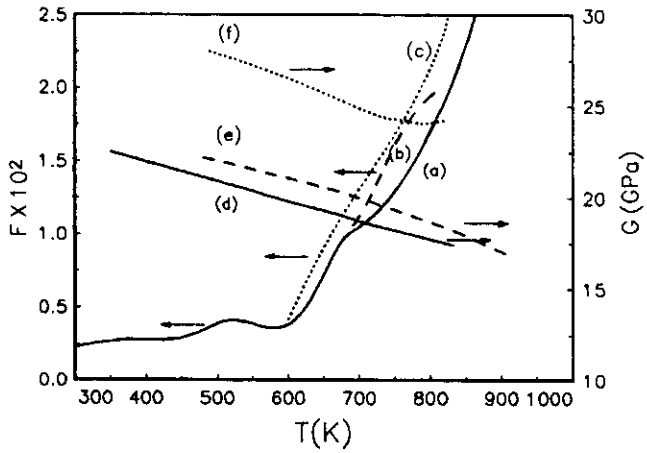

Fig. 4. MDS for implanted samples (1×10^{15} ions cm^{-2}) and unimplanted ones. Annealing condition: 1 h, 1073 K, 10^{-4} Torr.

condition II are shown in Fig. 4. The MDS spectra in the implanted sample, under implantation conditions A and C, and the unimplanted case, can be seen. The IFS of the unimplanted samples, and the implanted ones under conditions A and C, are plotted in curves (a), (b) and (c) respectively. The corresponding temperature dependence of the shear modulus is presented in curves (d), (e) and (f) respectively.

In curve (b), the peak can be seen at about 800 K, repeating the result shown in Fig. 3(b), while no differences can be seen between the argon irradiated and unimplanted samples.

In curves (e) and (f) a rise in the shear modulus of about 10% with respect to curve (d) (unimplanted case) is observed. However, in the case of curve (f) a small increase of about 5% for curve (e) can be observed.

Figure 5 shows the MDS thermal cycling for the implanted sample under condition B, previously annealed under condition II (curve (a) for the IFS and curves (c) for the shear modulus), and the IFS (curve (b)) and the shear modulus (curve (d)) for the unimplanted sample under the same annealing condition.

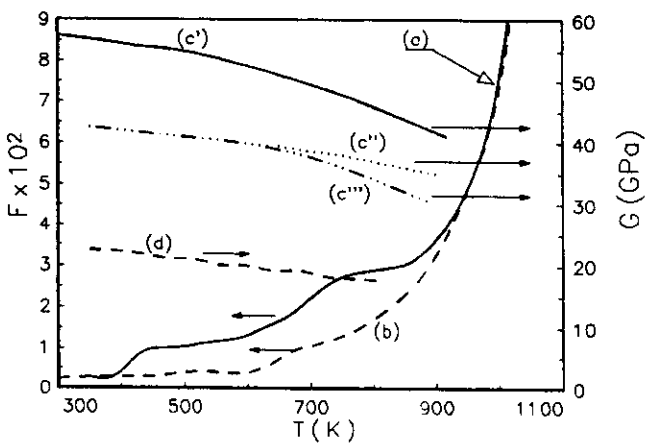

Fig. 5. MDS thermal cycling for implanted samples (2×10^{15} ions cm^{-2}) and unimplanted ones. Annealing condition: 1 h, 1073 K, 10^{-4} Torr.

The IFS (curve (a)) was determined in a running up–running down complete thermal cycle, and in running up 1 week later, showing the same behavior within a 20 a.u. dispersion.

Curves (c'), (c'') and (c''') show the shear modulus measured simultaneously with the IFS shown in the family of curve (a).

A strong modification on the IFS by the ion implantation process can be seen. An increase in the internal friction and a rise in the shear modulus of about 100% is observed as a consequence of the ion implantation process.

Hysteresis effects were not observed in IFS testing. This means that the changes found, generated by the ion implantation on the microstructure of the sample, and successively activated by the temperature, are stable and irreversible in the temperature range measured. A moderate reduction is shown in the values of shear modulus due principally to a recuperation mechanism of the structure. This behavior is not in contradiction with that described in the above paragraph regarding the repetition of the IFS against temperature.

4. Discussion

The IFS tests of the unimplanted samples are in agreement with those reported in the literature. In the cases of unimplanted samples annealed under condition I the three peaks already found [3] at 534, 650 and 950 K were found. Nevertheless, in the cases of unimplanted samples annealed under condition II only two of those peaks, 534 and 650 K, were found [3].

For the IFS tests of implanted samples under condition A, in both cases of annealing, a peak was found at about 820 K which was not present in the unimplanted samples or in the argon irradiated samples. The height of this peak is approx. 1×10^{-2}, in the IFS test of the implanted sample previously annealed under condition I and of only about 3×10^{-3} in the IFS of the implanted sample for annealing condition II.

The mechanism which controls the effect of this peak could be explained on the basis of the sliding of grain boundaries controlled by impurity diffusion [12–14]. Such an impurity could be nitrogen atomic molecules of N–O, nitrogen in doublets or triplets or precipitates.

In the case of the implanted sample under condition B the IFS is increased, but the mechanisms involved are those described previously.

The increase in the shear modulus found could be associated with the introduction of nitrogen atoms in the f.c.c. latice and to the generation of defects in the matrix by ion irradiation.

5. Conclusions

Three important points can been established.

A strong increase in the shear modulus has been found for the implanted samples with respect to the unimplanted ones.

A new peak, absent in the unimplanted samples, has been detected.

Both effects are stable in time and in temperature, inside the range of measurement for the samples implanted with nitrogen and argon. An anomalous behavior related to instability in the elastic shear modulus has been found in the samples implanted with argon at higher temperatures. This effect will be discussed elsewhere [15].

Acknowledgments

This work was partially supported by IAEA (Research Contract No. RC/6477/R1/-RB), and ICTP, Trieste, Italy (TWAS Research Grant No. MP 90–090), National Council of Research, Argentina (CONICET), Antorchas Foundation and Proyecto Multinacional de Investgación y Desarrollo en Materiales AOS-CNEA.

References

1 A. S. Nowick and B. S. Berry, *Anelastic Relaxation in Crystalline Solids*. Academic Press, New York, 1972.
2 B. Purniah, *Ph.D. Thesis*, University of Madras, 1985.
3 G. M. Ashmarin, M. Y. Golubev, N. Y. Naumova and A. V. Shalimova, *Proc. Internal Friction and Attenuation in Solids*, International Academic Publishers, Beijing, 1990, p. 133.
4 J. Feugeas, E. Llonch, C. O. de González and G. Galambos, *J. Appl. Phys., 64* (5) (1988) 2648.
5 J. Feugeas, C. O. de González, C. Gazza, M. Nieto, M. F. Peyronel and G. Sánchez, *Braz. J. Vacuum Appl., 9* (2) (1990) 118.
6 Y. Kondoh, K. Shimoda and K. Hirano, *Jpn. J. Appl. Phys., 20* (2) (1981) 393.
7 W. Stygar, G. Gerdin and F. Venneri, *Nucl. Fus., 22* (9) (1982) 1161.
8 G. Sánchez, G. Grigioni and J. Feugeas, *Surf. Coat. Technol., 70* (1995) 181.
9 J. Feugeas, G. Sánchez, G. Grigioni, C. O. de Gonzalez and A. Pochettino, in G. Bonizzoni (ed.), *Proc. Industrial Applications of Plasma Physics, Varenna, September 1992*, Societa Italiana di Fisica, Rome 1993, p. 551.
10 F. Povolo, B. Molinas and O. Lambri, *Il Nuovo Cimento, 14D* (1992) N2.
11 F. Povolo, O. Lambri, I. Manso and A. Suri, *Report IFIR 3/92*, Internal Report of the Instituto de Física Rosario, 1992.
12 D. Mosher and R. Raj, *Acta Metall., 22* (1974) 1469.
13 R. Raj and M. F. Ashby, *Metall. Trans., 2* (1967) 181.
14 H. J. Frost and M. F. Ashby, *Deformation Mechanism Maps. The Plasticity and Creep of Metals and Ceramics*, Pergamon, New York, 1982.
15 O. A. F. Lambri, G. Sánchez, J. Feugeas and F. Povolo, *Surf. Coat. Technol., 70* (1995) 191.

J. Phys. D: Appl. Phys. 30 (1997) 2917–2922. Printed in the UK PII: S0022-3727(97)82501-6

A study by emission spectroscopy of the N_2 active species in pulsed DC discharges

S P Brühl†, M W Russell†§, B J Gómez†, G M Grigioni†, J N Feugeas† and A Ricard‡

† Instituto de Física Rosario (CONICET-UNR), Boulevard 27 de Febrero 210 bis, 2000 Rosario, Argentina
‡ CPAT, Université Paul Sabatier, 118 route de Narbonne, 31-062 Toulouse, France

Received 11 March 1997, in final form 29 July 1997

Abstract. From the optical emission of N_2 and N_2^+ radiative states in the negative glow of N_2 DC pulsed discharges at pressures 1–4 Torr (133–532 Pa) and current densities 1–6 mA cm^{-2}, it has been determined that the vibrational excitation of the N_2 state deviates from a Boltzmann distribution and strong intensities of the N_2 second positive system (especially from $v = 1$) were also observed in the afterglow. Such strong emission is interpreted in terms of the growing of the $N_2(X, v)$ vibrational distribution in the post-discharge region as the gas temperature is reduced. The $N_2^+(B^2\Sigma_u^+)$ states are mainly produced by electron collisions on $N_2^+(X)$ ions under discharge conditions and quickly disappear in the afterglow as a result of N_2^+–electron recombination.

1. Introduction

Nitriding is applied to increase resistance to fatigue by the development of thick diffusion layers. In the same nitriding cycle, surface properties such as resistance to corrosion and wear may be increased by the growth of thin (1–10 μm) surface compound layers (γ-Fe_4N and ε-Fe_2N_{1-x} for iron and steel nitriding and δ-TiN and ε-Ti_2N for titanium nitriding with the exception of the more recent [1] plasma post-discharge nitriding process). The glow discharge used as a processing plasma for surface treatment can be established and sustained in various ways such as by using DC diode discharges, RF and microwave discharges or transferred plasma. In ion nitriding of iron and steels, standardized nitrogen–hydrogen gas mixtures with or without the addition of methane allow the formation of diffusion layers with or without the formation of compound layers. Pure nitrogen plasma only is used for nitriding titanium alloys. The plasma parameters are chosen in the range 1–10 Torr (133–1333 Pa) for the gas pressure and several mA cm^{-2} for discharge current densities, to heat the workpiece to 770–840 K in order to reach the α phase of N atom diffusion inside the metal. In industrial reactors, the voltage and the discharge current are modulated with variable frequencies and duty cycles, often in the medium frequency range 10–50 kHz. However, the active species which are produced during the pulse and the behaviour of these species after the discharge have scarcely been studied [2]. It is the purpose of the present work to analyse by optical emission spectroscopy the N_2 radiative species during a DC pulsed discharge and in the afterglow. A kinetic analysis will be proposed to explain the experimental results.

§ On leave from: Naval Research Laboratory, Code 6174, 4555 Overlook Avenue SW, Washington, DC 20375, USA.

2. The experimental set-up

A schematic illustration of the nitriding plasma reactor is shown in figure 1. The reactor consisted of two stainless steel circular plane electrodes, 6 mm thick and 35 mm in diameter. The upper electrode was negatively biased (the cathode) and the lower (the anode) was at earth potential. The electrodes were separated by 40 mm and located in a cylindrical Pyrex glass vacuum chamber (70 mm in diameter and 290 mm in length).

The cathode was connected to the power supply through a cylindrical hollowed stainless steel rod which allowed the introduction of a thermocouple to monitor the temperature of the electrode in the plasma region. The rod was completely covered by a Pyrex pipe, avoiding plasma generation along its surface and ensuring that the discharge was being generated only around the surface of the cathode planar disc (25 cm^2).

Prior to introducing the process gases, the chamber was evacuated to a base pressure of 15 mTorr (2 Pa). Using flowing N_2, an abnormal DC pulsed plasma was produced

0022-3727/97/212917+06$19.50

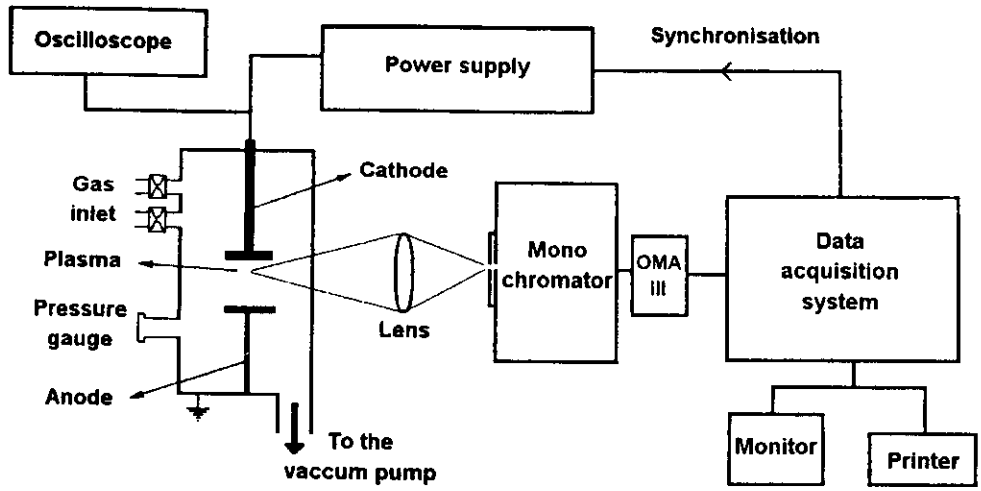

Figure 1. The experimental set-up.

at a pressure in the range 0.5–10 Torr (67–1330 Pa) and discharge currents in the range 10–200 mA. The pulsed widths of the discharge were variable in the range 1–60 ms, such that the total time available for the discharge and afterglow was determined by the operating frequency of the power supply (16.67 Hz).

A PAR optical spectrometer (focal length 275 mm; grating width 600 grooves mm^{-1}) and OMA III multichannel analyser (Princeton Applied Research) detected via an optical lens the plasma glow near the cathode. By imaging the plasma glow on the entrance slit of the spectrometer, the total discharge emission in the negative glow or in the after-glow was detected from a distance of about 1 cm from the cathode surface with an integrated time of 30 ms.

To synchronize the data acquisition with the discharge pulse, the following procedure was used. The OMA was programmed with a sequence of an active scan (during which data were stored) followed always by an ignored scan (data not stored); and the voltage supply was commanded by a trigger pulse delivered from the OMA III spectrometer at the beginning of each active scan. The delay time could be varied to choose in which part of the discharge (glow and various times inside the afterglow) the active scan took place [3].

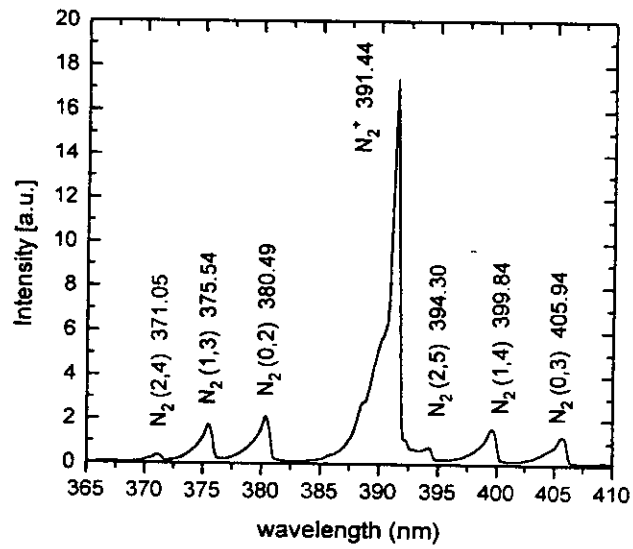

Figure 2. A partial optical emission spectrum for nitrogen for a 30 ms pulsed discharge: cathode potential 450 V, discharge current 150 mA and pressure 4 Torr (532 Pa).

3. Radiative state intensities

3.1. The emission in the N_2 discharge

The emission of the N_2 discharge was mainly produced from the negative glow around the steel cathode. The dominant species bands were the first negative bands of N_2^+ and the first positive and second positive bands of N_2. A part of the spectrum showing emission from N_2^+(B, 0–X, 0) at 391.44 nm and N_2(C, v'–B, v'') $\Delta v = -2$ and $\Delta v = -3$ bands is shown in figure 2 for a 4 Torr (532 Pa), 150 mA discharge of 30 ms duration. It can be seen in figure 2 that the N_2^+ first negative band at 391.44 nm was the most intense, which is a characteristic of N_2 negative glows [4].

From the N_2(C, v'–B, v'') $\Delta v = -2$ and $\Delta v = -3$ sequences, the vibrational excitation of N_2 can be analysed [5, p 102], whereby the band intensity, $I_{CB}(v', v'')$, is related to the N_2(C, v') density [C, v'] by

$$I_{CB}(v', v'') = k(\lambda)[C, v']\frac{A_{CB}(v', v'')}{\lambda} \qquad (1)$$

where $k(\lambda)$ is the spectral response of the spectrometer and $A_{CB}(v', v'')$ is the radiative frequency of the (C,v'–B, v'') bands [6]. By assuming a constant value of $k(\lambda)$ for the short spectral ranges of the analysed $\Delta v = -2$ band emission (360–380 nm), the [C, v'] vibrational distribution was determined from the results of figure 2. In the I_{CB} (v', v'') intensity measurements, care was taken to correct for the band overlapping. For that, with a spectrum as shown in figure 2, the band-head intensity was measured by subtracting the preceding band tail. This vibrational distribution is shown in figure 3.

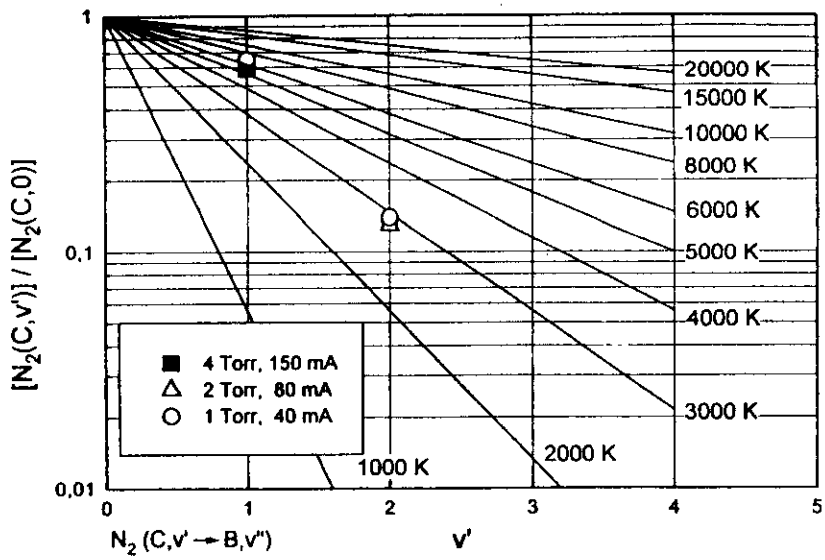

Figure 3. A Boltzmann graph of the vibrational distribution of states $[N_2(C, v')]$ versus the initial vibrational state, v'. Experimental points were determined under discharge conditions.

For the experimental conditions studied (4 Torr, 150 mA; 2 Torr, 80 mA; and 1 Torr, 40 mA) a non-Boltzmann vibrational distribution of the $N_2(C, v')$ state was found, whose $N_2(C, 1)$ density was always higher than the Boltzmann line at 3000 K (see figure 3).

3.2. The emission in the N_2 afterglow

The $N_2^+(B–X)$ and $N_2(C–B)$ bands were always emitted in the afterglow. Because the time constant of OMA detection was 30 ms, the discharge time was reduced to 18 ms to leave 42 ms to record the afterglow with acquisition times starting from 1 to 12 ms. The temporal variations of N_2^+ (391.44 nm) and N_2 (380.49 and 375.54 nm) band intensities are shown in figure 4 for the discharge conditions of figure 2. In figure 4 a sharp linear decrease of the N_2^+ intensity is observed during the first 10 ms within the afterglow. The same time variations were observed for the other discharge conditions (1 and 2 Torr).

In contrast, the N_2 intensities decreased slowly with time inside the afterglow. The vibrational excitation between these bands is shown in figure 5 which gives the $I(C, 1–B, 3)/I(C, 0–B, 2)$ and $I(C, 1–B, 4)/I(C, 0–B, 3)$ intensity ratios during the discharge (under the conditions of figure 2), as well as during the afterglow as a function of the acquisition start time. It can be observed that the vibrational excitation was higher within the afterglow. Similar results are shown in figure 6 for the discharge conditions of 2 Torr (266 Pa), 80 mA, at a time up to 12 ms.

4. The kinetic analysis of the experimental results

4.1. Discharge conditions

From previous kinetic analysis [3, 4] it can be estimated that the $N_2(C, v')$ excited states in the negative glow are mainly produced by electronic collisions as follows:

$$e + N_2(X, v) \rightarrow e + N_2(C, v') \qquad (a)$$

with an electron rate $k_e^C(v')$ which depends on the $N_2(C, v')$ cross section and on the electron distribution function [5, p 31]. The $N_2(C, v')$ states are de-excited by radiative emission with a frequency $v_C^r(v')$ so that the pseudo-stationary density of $N_2(C, v')$ is given by

$$N_2[(C, v')] = \frac{[N_2(X, v)]n_e k_e^C(v')}{v_C^r(v')}. \qquad (2)$$

Thus the $N_2(C, v')$ excited states are directly related to the $N_2(X, v')$ ground state by electron collisions. The vibrational temperature of $N_2(C, v')$, T_v^C, is therefore directly correlated to that of $N_2(X, v')$, T_v^X [5, p 121]. For example, it has been shown that, for $T_v^C = 4000$ K, $T_v^X = 2000$ K.

Other processes, in addition to reaction (a), can arise from collisions between $N_2(A)$ and $N_2(X, v)$ metastable molecules as follows:

$$N_2(A) + N_2(A) \rightarrow N_2(C, v') + N_2(X) \qquad (b)$$

$$N_2(A) + N_2(X, v > 19) \rightarrow N_2(C, v') + N_2(X) \qquad (c)$$

$$N_2(X, v > 24) + N_2(X, v > 24) \rightarrow N_2(C, v') + N_2(X) \qquad (d)$$

with $k_b = 1.5 \times 10^{-10}$ cm^3 s^{-1} [7], $k_c \leq 6.0 \times 10^{-14}$ cm^3 s^{-1} [8] and $k_d \leq 6.5 \times 10^{-17}$ cm^3 s^{-1} [8]. For reactions (b)–(d), the $N_2(C, v')$ populations deviate from a Boltzmann distribution, which could explain the overpopulation of $N_2(C, v' = 1)$ that we observed. (That the possibility of excitation of $N_2(C, v')$ from $N_2(A)$ metastable states by electron collisions in the post-discharge region cannot be excluded was demonstrated recently [13].)

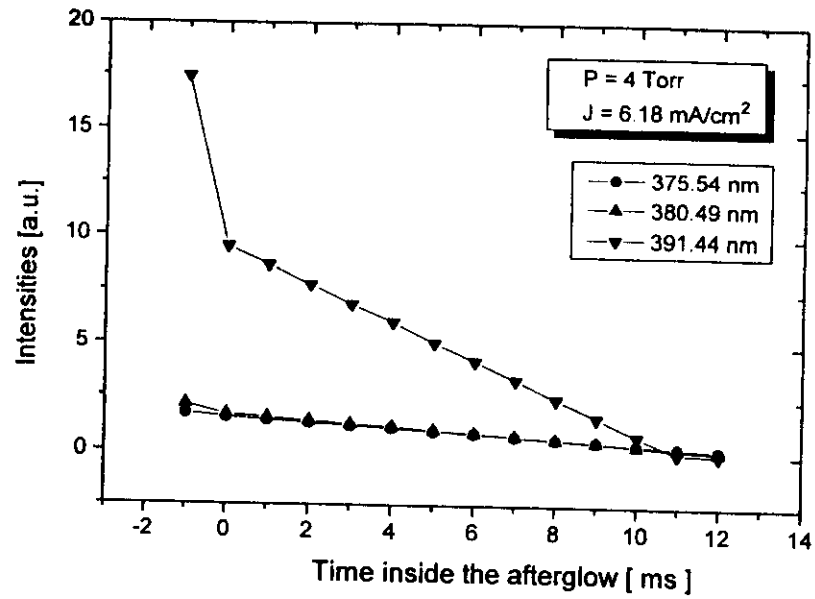

Figure 4. The variation of selected peak intensities during the discharge and the afterglow for various acquisition start times (pulse 18 ms, post-discharge time 42 ms).

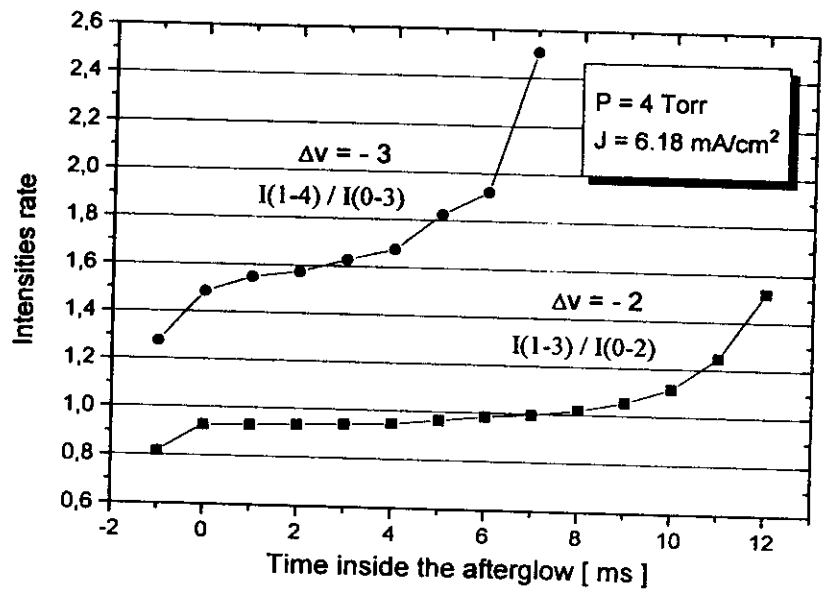

Figure 5. The ratios of the emission intensities for N_2(C–B) transitions $I_{N_2}(1\text{–}3)/I_{N_2}(0\text{–}2)$ and $I_{N_2}(1\text{–}4)/I_{N_2}(0\text{–}3)$ during the discharge ($t_{aq} = -1$ ms) and for various acquisition start times within the afterglow. The cathode potential was 450 V, the discharge current was 150 mA and the pressure was 4 Torr.

Considering the population of $N_2^+(B)$ states, it had previously been shown [9] that, for $n_0R > 10^{16}$ cm^{-2} (n_0 is the gas density, R is the tube radius) in a HF discharge and in the positive column, the main electron excitation is from N_2^+ ions as follows:

$$e + N_2^+(X) \rightarrow e + N_2^+(B) \qquad (e)$$

with a rate coefficient $k_e = 4 \times 10^{-11}$ cm^3 s^{-1} at $T_e = 3$ eV [10].

Also, collisions with $N_2(X, v)$ molecules as given by the following reaction can be relevant:

$$N_2(X, v > 12) + N_2^+(X) \rightarrow N_2(X, v) + N_2^+(B) \qquad (f)$$

with

$$k_f = (1.7\text{–}2.8) \times 10^{-10} \exp\left(\frac{1000}{T_{N_2^+}(K)}\right) \text{ cm}^3 \text{ s}^{-1}$$

($\approx 10^{-11}$ cm^3 s^{-1} at 300 K) [8].

The $N_2^+(B)$ states are destroyed by radiative emission and quenching [5, p 122] with a frequency ν_{B^+}, so that the pseudo-stationary density of $N_2^+(B)$ is given by

$$[N_2^+(B)] = \frac{[N_2^+(X)](n_e k_e + [N_2(X, v > 12)]k_f)}{\nu_{B^+}}. \qquad (3)$$

Therefore the strong intensity of $N_2^+(B)$ observed in the negative glow for pressures of 1, 2 and 4 Torr (532 Pa) can

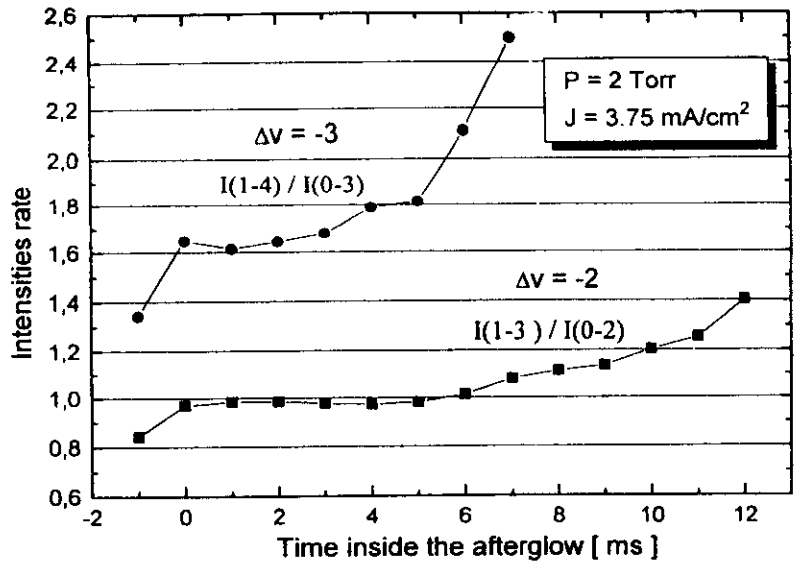

Figure 6. The same as figure 5 except that the cathode potential was 460 V, the discharge current was 80 mA and the pressure was 2 Torr (266 Pa).

be related to there being a high electron density and/or high vibrational excitation of the $N_2(X)$ ground state.

4.2. Afterglow conditions

During the afterglow the electron energy is not sustained by the plasma electric field. Only superelastic collisions at low energies occur [11]. From [2], a mean electron temperature of 0.5 eV has been estimated in the post-discharge region. Consequently, electronic excitations having high activation thresholds such as $N_2(C)$ ($\cong$11 eV) are unlikely to contribute and it can be assumed that reaction (a) disappears in the afterglow. Therefore the $N_2(C)$ states are mainly produced by reactions (b)–(d) with the following kinetic equation:

$$\frac{d[N_2(C, v')]}{dt} = [N_2(A)]^2 k_b + [N_2(A)][N_2(X, v > 19)]k_c + [N_2(X, v > 24)]^2 k_d - N_2(C)\nu_c^r(v'). \quad (4)$$

Equation (4) is strongly dependent on the temporal variations of $N_2(A)$ and $N_2(X, v)$. Because the $N_2(A)$ states are quickly destroyed by collisions with the tube wall whereas the $N_2(X, v)$ vibrational molecules are not [5, p 47], it is estimated that the $N_2(X, v > 24)$ vibrational states are more populated than is $N_2(A)$ in the afterglow. Therefore, in reaction (4), the last production term ($[N_2(X, v > 24)]^2 k_d$) could explain the nearly constant density of $N_2(C)$ states observed in the afterglow. The $N_2(X, v)$ high vibrational levels coming from the afterglow could favour the following step-wise process at the beginning of the next discharge pulse:

$$e + N_2(X, v) \rightarrow 2e + N_2^+ \quad (g)$$

$$e + N_2(X, v) \rightarrow e + N + N. \quad (h)$$

The low excitation threshold of reaction (e) (2.5 eV) may permit electronic excitation of $N_2^+(B)$ states in the afterglow ($k_e = 10^{-11}$ cm^3 s^{-1} at $T_e = 1$ eV [10]). The time-varying kinetic equation of $N_2^+(B)$ is as follows (see equation (3) for the pseudo-stationary density in the discharge):

$$\frac{d[N_2^+(B)]}{dt} = [N_2^+(X)](n_e k_e + [N_2(X, v > 12)]k_f) - [N_2^+(B)]\nu_{B^+}. \quad (5)$$

From equation (5) it follows that the time-varying behaviour of $N_2^+(B)$ is sharply affected by the following electron–ion recombination:

$$N_2^+ e \rightarrow N + N \quad (i)$$

with $k_i \simeq 10^{-7}$ cm^3 s^{-1} at $T_e = 300$ K [12].

The recombination reaction (i) is an efficient loss process which is accelerated as the electron energy decreases ($k_i = 2 \times 10^{-7} \exp(300/T_e(K))^{-0.4}$ [12]). This mechanism could explain the observed decrease in $N_2^+(B)$ intensity.

5. Conclusion

By using emission spectroscopy of the negative glow of pulsed N_2 DC discharges and afterglows, the vibrational excitation of neutral nitrogen molecules has been determined. Under conditions of N_2 pressures in the range 1–4 Torr (133–532 Pa) and current densities in the range 1–6 mA cm^{-2}, a higher vibrational excitation of the $N_2(C, v' = 1)$ state has been found on going from discharge to afterglow conditions. Such an increase in vibrational excitation during the afterglow can be explained in terms of a decrease in the vibrational quenching of $N_2(X, v)$ by the neutral gas as the gas temperature is decreasing. An increase in $N_2(C, v' = 1)$ is related to an increase in the $N_2(X, v)$ vibrational population and then of N atoms which are produced by dissociation following the $N_2(v'–v'')$ climb-up process.

The excitation of N_2^+ has been analysed as occurring by electronic collisions with N_2^+ ions in the discharge and afterglow. Such an excitation is efficient in the discharge but quickly decreases in the afterglow because of electron–ion recombination.

A consequence of a high level of N_2 vibrational excitation during the afterglow is to favour ionization and dissociation of nitrogen during the pulsed discharge. Then, for a given discharge current, the maintenance voltage is lowered by the step-wise ionization process with the advantages that, first, the power yield of the plasma reactor is increased and, second, arc formation producing damage to the cathode is avoided.

Acknowledgments

This work was partially supported by IAEA (research contract RC/6477/R1/RB) and CONICET grants. MWR gratefully acknowledges the support of a J William Fulbright Scholarship. The authors are indebted to Ing Aldo Marenzana for the construction and maintenance of the power-supply and synchronization system.

References

[1] Michel H, Czerwiec T, Gantois M, Ablitzer D and Ricard A 1995 *Surf. Coat. Technol.* **72** 103
[2] Hugon R, Fabry M and Henrion G 1996 *J. Phys. D: Appl. Phys.* **29** 761
[3] Feugeas J N, Marenzana A, Brühl S P and Gómez B J A 1997 Power voltage source synchronized with a spectrometer for real time spectroscopic studies of pulsed discharges *IEEE Trans. Instrum. Meas.* submitted
[4] Petitjean L and Ricard A 1984 *J. Phys. D: Appl. Phys.* **17** 919
[5] Ricard A 1996 *Reactive Plasmas* (Paris: Société Française du Vide)
[6] Lofthus and Krupenie P H 1977 *J. Chem. Phys. Ref. Data* **6** 113
[7] Piper L G 1988 *J. Chem. Phys.* **88** 231
[8] Slovetskii D I 1980 *Mechanisms for Chemical Reactions in Non-Equilibrium Plasmas* (Moscow: Nauka) (in Russian)
[9] Ricard A, Touzeau M and Moisan M 1977 *J. Physique* **38** 669
[10] Crandall D, Kauppila W A, Phaneuf R A, Taylor P O and Dunn G H 1974 *Phys. Rev.* A **9** 2545–51
[11] Capitelli M, Gorse C and Ricard A 1981 *J. Physique Lett.* **42** 469
[12] Mehr F J and Biondi M A 1969 *Phys. Rev.* **181** 26
[13] De Benedictis S and Dilecce G 1985 *Chem. Phys.* **92** 149

J. Phys. D: Appl. Phys. 32 (1999) 2228–2235. Printed in the UK PII: S0022-3727(99)01059-1

In situ synchrotron radiation diffraction study of low carbon steel during ion nitriding

J N Feugeas†, J D Hermida‡, B J Gomez†, G Kellermann§ and A Craievich‖

† Instituto de Fisica Rosario (CONICET-UNR), Bv 27 de Febrero 210 Bis., 2000 Rosario, Argentina
‡ Comisión Nacional de Energía Atómica, Buenos Aires, Argentina
§ National Synchrotron Light Laboratory, Campinas, SP, Brazil
‖ Institute of Physics, University of São Paulo, São Paulo, SP, Brazil

Received 19 January 1999, in final form 22 April 1999

Abstract. The volume close to the surface of materials subjected to ion implantation or ion diffusion exhibits structural transformations that are usually studied by x-ray diffraction. In order to characterize the kinetic aspects of structural transformations in low carbon AISI 1010 steel during ion nitriding, an *in situ* synchrotron radiation diffraction study was performed. An experimental set-up, a specially designed reactor, was constructed for x-ray measurements in real time. The variation in the lattice parameter with time of the initial Fe-α phase was attributed to the heating effect produced by the action of an electric discharge during the first stages of the process. The analysis of the x-ray diffraction patterns indicates the formation of several iron nitrides. The Fe_3N phase exhibits a progressive decrease in the interplanar distances, which is clearly a different behaviour with respect to the other observed phases, even considering a phase with nearly the same stoichiometry.

1. Introduction

Ion nitriding is a process in which active species of nitrogen, generated by an electric discharge out of the thermodynamic equilibrium, are absorbed on a material surface and diffused into the bulk [1]. Depending on the discharge conditions, the structural features in the volume close to the surface vary strongly. The final system is composed of different types of compound layers several tens of micrometres thick (iron nitrides with different stoichiometries). The nitriding development begins with the dilution of the nitrogen in the matrix. By increasing the nitrogen concentration, iron nitrides with different nitrogen contents, such as $Fe_{16}N_2-\alpha''$, Fe_4N-γ', Fe_3N-ε and eventually Fe_2N-ξ, are formed in carbon steels [2, 3]. In multicomponent steels, nitrides of other elements can also be developed.

The kinetics of formation of the compounds and phases depends not only on the nature of the steel, but also on the characteristics of the nitriding process. By using classical x-ray diffraction set-ups, the study of the time evolution of nitride formation (nitriding kinetics) is generally carried out by successive measurements of different individual samples, all of them treated under identical conditions, but interrupting the process at different times. This procedure always presents uncertainties related to the possible lack of repeatability of the process conditions for each sample, including the previous sample preparation. Another possibility could be the study of a single sample after different sequential and partial nitriding processes. This procedure may also not be adequate because of the unavoidable repeated thermal cycling to which the sample is subjected.

Sequenced *in situ* diffraction measurements using synchrotron radiation eliminate the problems mentioned in the preceding paragraph [4]. The use of a powerful x-ray beam, such as those provided by synchrotron sources, is necessary for this type of experiment in order to obtain a series of good-quality diffraction patterns within short time intervals. Acceptable x-ray diffraction patterns can be obtained after a few minutes of exposure time or even less, depending on the synchrotron photon flux and beam collimation conditions.

We report in this paper the details of the construction of a reactor for material nitriding installed on a synchrotron x-ray beamline for *in situ* x-ray diffraction measurements. This reactor allows the determination of a series of x-ray patterns during the nitriding process, corresponding to a well defined volume of the sample which is constant in time.

The first application of the developed experimental set-up was an *in situ* x-ray diffraction study of the structural transformations occurring in a low carbon steel (AISI 1010) during ion nitriding induced by a pulsed dc glow discharge.

0022-3727/99/172228+08$30.00

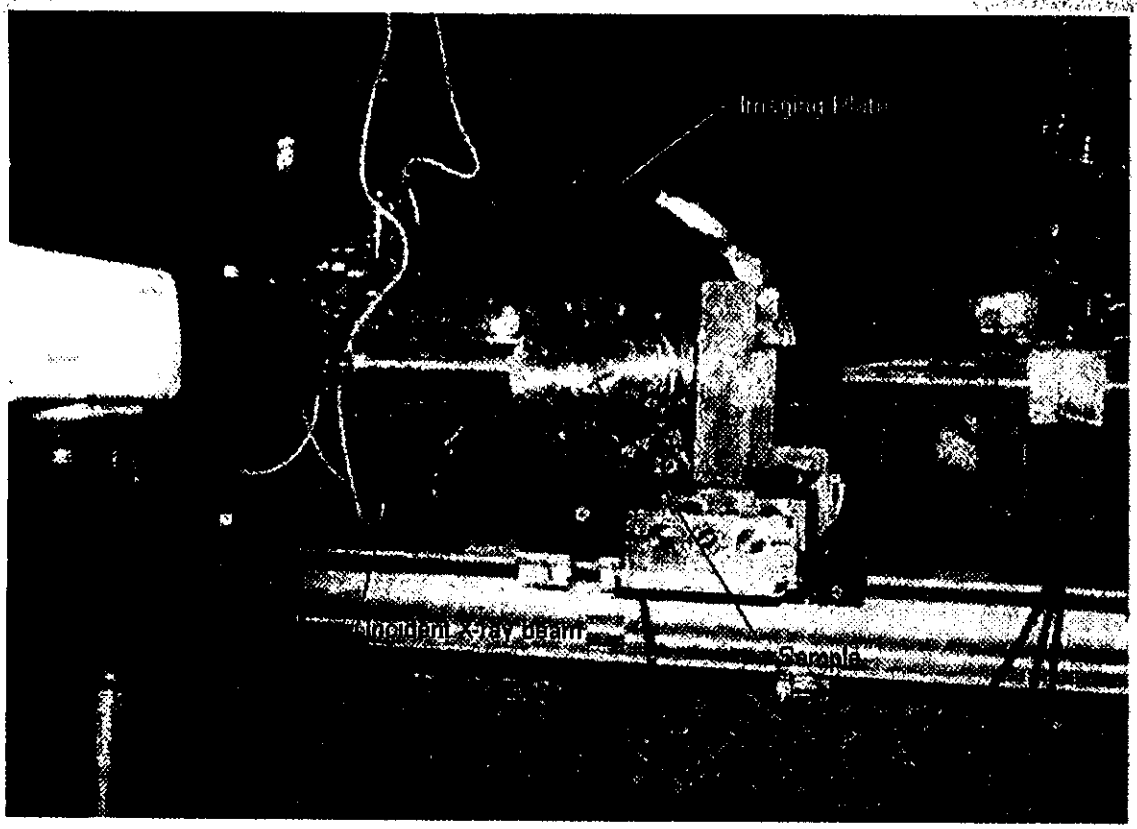

Figure 1. The experimental set-up: the ion nitriding reaction chamber installed in the synchrotron SAXS beamline of LNLS during its operation.

2. Experimental details

2.1. Reactor description

The reactor for ion nitriding consists of a stainless steel cylindrical chamber, 150 mm in diameter and 200 mm in length, with a removable glass window in one of the lateral circular faces for visual observation of the interior. The opposite circular face is a frame for the insertion of a rotating cylindrical shaft supporting at its extreme end the sample holder. This shaft is coaxial with the cylindrical chamber. An overall view of the set-up is shown in figure 1 and the geometrical details of the reactor in figure 2.

A teflon gasket is used between the shaft and the lateral frame for vacuum sealing of the chamber in order to maintain inside the chamber a controlled low pressure. It also acts as an electrical insulator between the sample holder (negative biased) and the chamber walls (ground potential). The rotation movement of the sample holder is externally controlled using a standard micrometric screw. A coaxial internal cavity in the cylindrical shaft and sample holder allows a thermocouple to be placed very close to the material to be studied.

The incident and the diffracted x-ray beams enter and exit the chamber, respectively, through a 10 mm wide window (figure 2) cut in the lateral cylindrical wall of the chamber. The window covers an angular range from $-10°$ up to $+190°$ with respect to the direction of the direct x-ray beam, which hits the flat sample perpendicularly to the plane of the drawing shown in figure 2. The slit is closed with a 200 μm thick foil of Kapton, which is practically transparent to the x-ray beam and keeps the chamber vacuum sealed.

The reactor has appropriate connections for turbo-molecular vacuum pumping, gas mixture controlled input and vacuum measurement. The whole body is supported by a metallic support, which is mounted on the guiding rail along the x-ray beam path. The chamber can be displaced along the rail (in the direction of the beam) and horizontally by a rough translation device. The vertical movement of the chamber is very precise and remotely controlled using a standard translation stage equipped with a micrometric screw.

2.2. The synchrotron x-ray workstation

The reactor described was installed in the SAXS beamline of the National Synchrotron Light Laboratory, Campinas (Brazil), adapted for x-ray diffraction experiments. This beamline produces a monochromatic x-ray beam using a (111) silicon crystal reflection [5]. The beamline arm and the crystal Bragg angle were adjusted in order to have the beam hitting the sample with a wavelength $\lambda = 1.760$ Å. This wavelength was chosen because it is just above the edge K of Fe ($\lambda_K = 1.74$ Å) and it does not produce iron fluorescence, allowing the study of shallow layers. The wavelength was measured using a Fe filter and measuring its absorptance. The 2θ of the crystal monochromator was selected in such a way to provide a λ value just above the iron absorption edge ($\lambda_K = 1.74$ Å). A diffraction pattern of a standard sample of a paraffin ($C_{24}H_{50}$) was used to determine the x-ray wavelength. Even if this procedure is not very precise, it was adequate enough for us because we were interested in

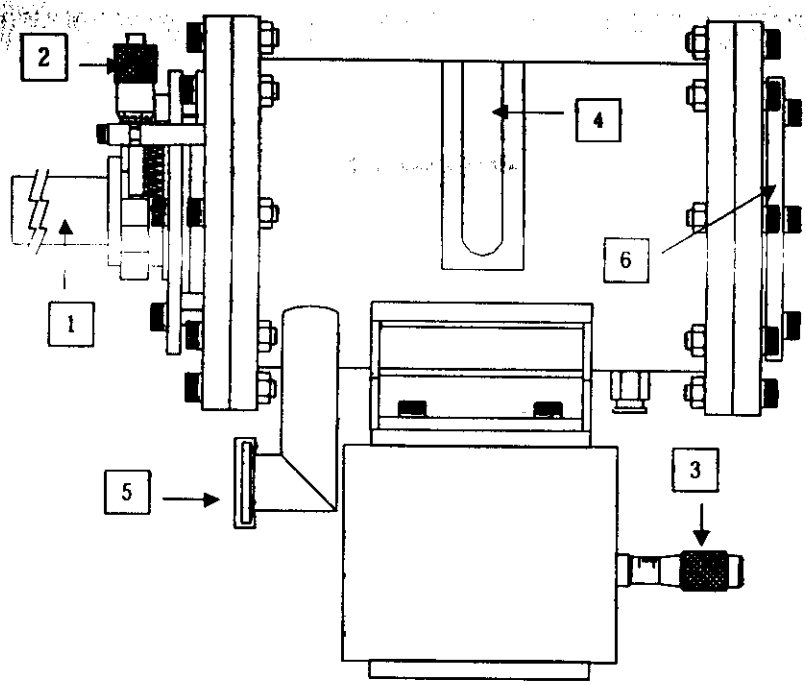

Figure 2. A schematic diagram showing the ion nitriding reactor with details related to the special design to make the x-ray diffraction analyses possible *in situ* and in real time. The figure corresponds to a plane perpendicular to the incident x-ray beam: 1, rotation axis; 2, sample rotation micrometric screw; 3, vertical displacement control (micrometric screw); 4, x-ray diffracted exit slit (Kapton foil covered slit); 5, vacuum pumping; 6, glass window.

variations of the crystallographic distances (and not in their absolute values). Typical maximal variations of $\Delta\lambda/\lambda$ due to thermal drifts are about 1/3000.

The silicon crystal collects 7 horizontal mrad of the incident white beam. It has a triangular shape and is bent in order to focus the beam horizontally. Adequate slits define the geometry of the beam, whose cross section at the sample position is 6 mm horizontally and 0.3 mm vertically.

The entrance and exit of x-ray beams were laterally centred with respect to the slit by a lateral chamber translation. The coincidence of the x-ray vertical beam position with the axis of the sample rotation was achieved by iterative vertical translations and rotations of the sample holder, while the intensity of the direct beam was monitored using a scintillator counter located at $2\theta = 0°$.

The choice of $\alpha = 20°$ allowed us to record the main diffraction peaks of Fe-α (110 and 200) and also the main nitride peaks. A smaller α ($\alpha = 10°$ or 15°) is not convenient because, under this condition, the diffraction peaks would be too wide.

2.3. Detection system

The photons diffracted by the sample exit the reaction chamber through the Kapton window and are recorded by means of an imaging plate (IP). The IP reader is a Molecular Dynamics Model Storm 820. The pixel size selected for the scanning was 200 μm. The IP is flexible and shaped by a cylindrical rigid holder (166 mm of diameter) whose axis is also the axis of rotation of the cylindrical shaft which holds the sample. The plate holder axis and the sample axis were put in coincidence by using a special mechanical device. This guarantees a concentricity within about 0.1–0.2 mm.

The exit slit is clearly indicated in figure 2 (central part, above). As explained, the different x-ray diffraction spectra are recorded by displacing the IP holder step by step in a direction parallel to the reactor axis.

The cylindrical frame containing the IP can be displaced horizontally along the direction of the sample axis of rotation by means of a translation stage driven by a stepping motor. This system (not shown in figure 2) is used to record many x-ray diffraction patterns (up to 16) successively. Once the recording of all the diffraction patterns is completed, the IP is removed from the frame and transferred to an electronic reader. The data plotted in figure 4 are Origin files exported from the Image-Quant package used to scan the imaging plates.

2.4. Nitriding conditions

The electric discharge across the gas inside the reactor was generated by a pulsed dc power supply [6]. The voltage is a polarized square wave with an amplitude that may be varied from 0 to 600 V. This negative potential is applied to the metallic sample holder, the rest of the chamber remaining at ground potential. The frequency can be varied from 0 (dc) to 1 kHz, with a control of the ratio between the active and passive parts of each cycle of discharge [7]. The current discharge is permanently controlled by means of a digital amperimeter.

In our experiments, the gas composition was 80% of nitrogen mixed with 20% of hydrogen, which was maintained inside the chamber at a constant pressure of 5.6 mbar, applied voltage 400 V, frequency 100 Hz and active-to-passive ratio 60%.

During the nitriding process, the samples are heated by the discharge up to temperatures of $\sim$ 400 °C. Nevertheless,

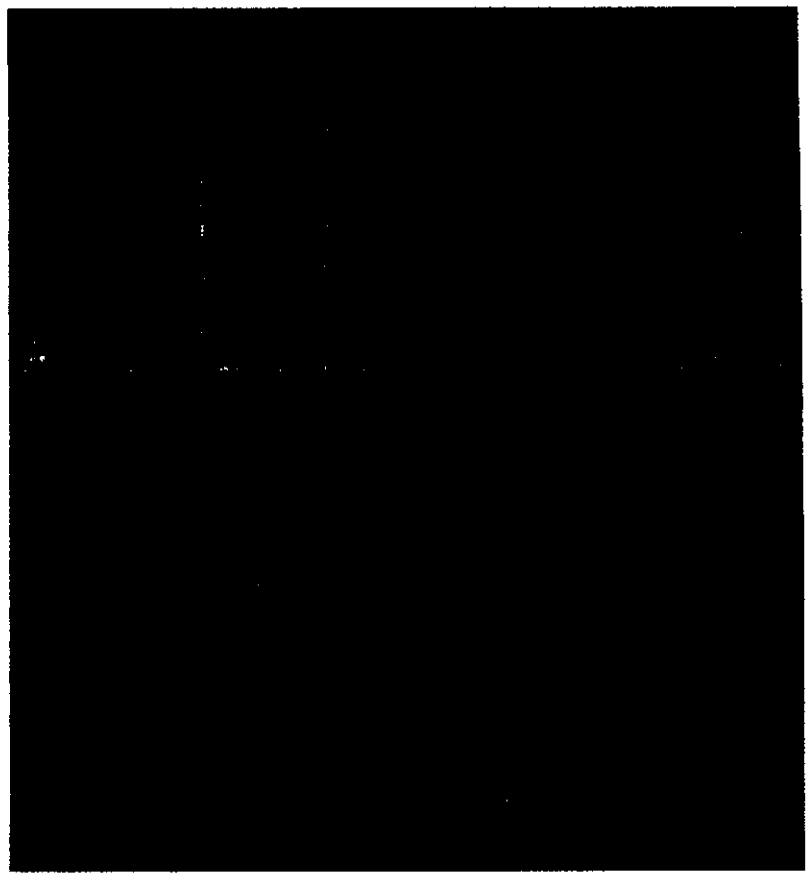

Figure 3. The imaging plate after exposure during the AISI 1010 sequential analysis and scanned through the Image-Quant image processing system. Each strip corresponds to a different diffractogram. The different x-ray intensities, which in the original are recorded in false colours (from maximum to minimum intensity: red, orange, yellow, green and blue), are presented here in black and white.
(This figure can be viewed in colour in the electronic version of the article; see www.iop.org)

the rest of the chamber did not overpass the temperature of $\sim 50\,^{\circ}C$ due to an external cooling, with the rest of the system (IP holder, chamber support, etc) at room temperature. This ensures that the geometry and the dimensions of the system set-up were kept virtually unaltered.

2.5. Samples

The studied material was an AISI 1010 steel (C: 0.08–0.13%; Mn: 0.3–0.6%; P: <0.04%; S: <0.05%). The sample tested was a disk 30 mm in diameter and 2 mm thick. The disk was normalized and mechanically polished (finished with 1 μm of diamond paste). For normalization, the sample was heated in an oven up to 800 °C, held at this temperature for a few minutes and then cooled down to room temperature.

3. Experimental results

A picture showing the spatial distribution of the diffracted photon density in the IP corresponding to all successively recorded spectra is shown in figure 3. Thirteen spectra were sequentially obtained, each of them with 10 min of exposure. The corresponding series of patterns of x-ray diffraction intensity is shown in figure 4 as a function of the scattering angle (intensity versus 2θ). This series of patterns contains the necessary information to characterize the kinetics of the structural transformations during the first 2 h 30 min of ion nitriding.

The ion nitriding conditions associated with each diffractogram, indicated by a-1, a-2,..., a-13, are reported in table 1. The first diffractogram (a-1) corresponds to the material before the beginning of the nitriding process, a normalized AISI 1010 steel.

The equation connecting the θ Bragg angles associated with the diffraction peaks to the spatial coordinate on the imaging plate, x, corresponding to the peak position is given by

$$\theta = (x - x_0)/2R \tag{1}$$

where x_0 is a reference position associated with the direct x-ray beam (corresponding to $2\theta = 0°$) and $R = 163.8$ mm is the radius of the cylindrical surface of the IP. The value of x_0 was indirectly determined assuming the lattice parameter was known room temperature for the initial body-centred-cubic (bcc) Fe-α structure.

The equation connecting the interplanar distances d_{hkl} and the Bragg angle θ_{hkl} (hkl are the Miller indexes) is given by Bragg's law

$$\lambda = 2d_{hkl}\operatorname{sen}\theta_{hkl}. \tag{2}$$

For cubic lattices

$$d_{hkl} = a/(h^2 + k^2 + l^2)^{1/2}. \tag{3}$$

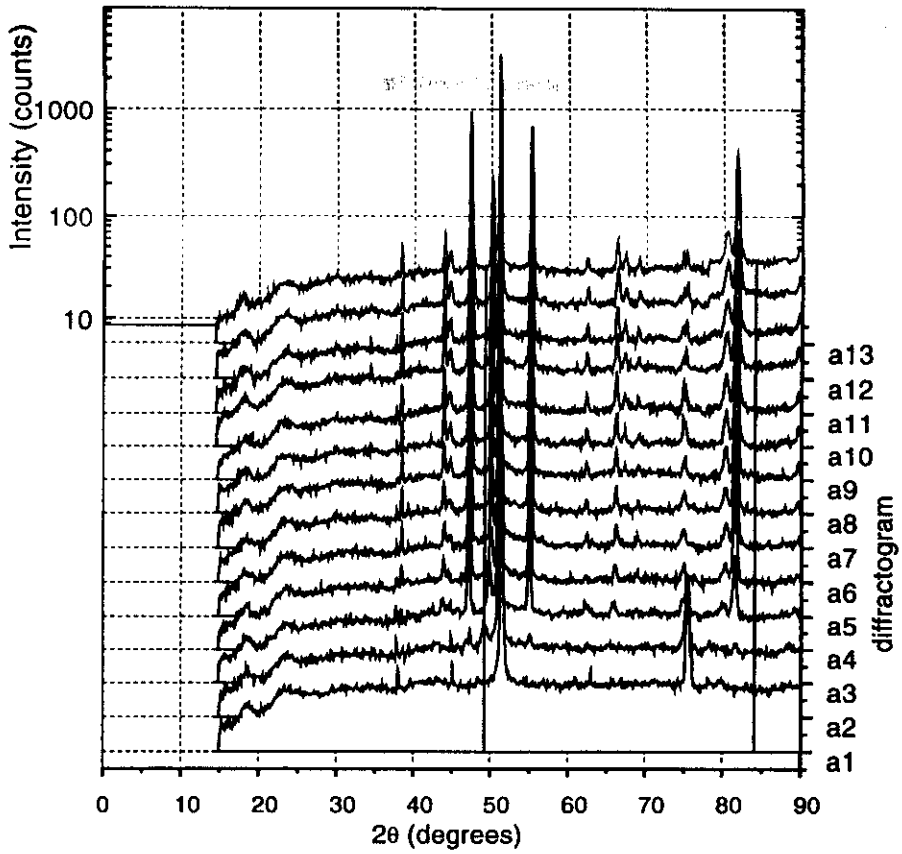

Figure 4. Sequence of the 13 x-ray diffraction patterns (a-1 to a-13) corresponding to the 13 strips in the imaging plate. Fe-α peak positions in all patterns (a-2 to a-13) are displaced towards lower angles with respect to the first a-1. A displacement towards high 2θ angles, during the first stage of processing (from a-2 to a-6 patterns), and for all peaks corresponding to the Fe_3N-ε phase can be seen. The intensities (vertical axis) are displayed on a logarithmic scale.

Table 1. Ion nitriding conditions for each diffractogram. In the first column each diffractogram is identified by the notation a-1 to a-13. In the second and third columns the initial time and the final time of each diffractogram recording are indicated in minutes of processing (0 minutes corresponds to the beginning of the nitriding process). In the fourth and fifth columns the sample temperature at the beginning and at the end of each diffractogram recording are indicated in °C degrees. The other nitriding parameters were kept constant (as indicated in the text) during the whole nitriding process.

Diffractograms	t_i (min)	t_f (min)	T_i (°C)	T_f (°C)
a-1	0	10	20	246
a-2	12	22	287	367
a-3	23	33	368	395
a-4	33	43	396	407
a-5	44	54	410	410
a-6	54	64	410	410
a-7	65	75	410	410
a-8	77	87	410	410
a-9	88	98	410	410
a-10	98	108	410	410
a-11	112	122	410	410
a-12	123	133	410	410
a-13	135	145	410	410

In our case, x_0 was determined by means of equations (1)–(3) using the well defined (110) and (200) Bragg reflections of the Fe-α phase.

The diffraction pattern a-1 (figure 5(a)) corresponds to the initial AISI 1010 steel before starting the ion nitriding process. This ferritic steel has a known bcc lattice with a parameter at room temperature of $a = 2.87$ Å. Two sharp peaks at $2\theta = 51.47°$ and $2\theta = 75.61°$ are apparent in figure 5(a), corresponding to Bragg reflections (110) and (200), respectively. These peaks are also visible in all the subsequent patterns but in these cases they are slightly shifted to smaller angles. In the a-2 pattern, recorded between 12 and 22 min after the beginning of the nitriding process, with a final temperature of 367 °C, the (110) and (200) peaks corresponding to Fe-α were found at 51.12° and 75.26°, respectively. In addition, other diffraction peaks are observed indicating the incipient formation of new phases, which then evolve during the rest of the nitriding process.

The final state of the sample is characterized by the last diffraction pattern a-13 (figure 5(b)), which was recorded between 2 h 20 min and 2 h 30 min after the start of the nitriding process, with the sample at 410 °C. In this pattern the (110) and (200) reflections, corresponding to the Fe-α phase, are still visible but somewhat attenuated.

In addition to the Bragg peaks corresponding to the parent Fe-α phase, a number of others are apparent in pattern a-13. They were identified as being produced by several different iron nitrides. We identified the (110), (111), (200), (210), (211) and (220) reflections as produced by a Fe_4N-γ'' phase. Two peaks detected ((100) and (102)) were attributed to a $Fe_{3+x}N_{1-x}$-ε phase with $x = 0.17$ [8].

The a-2 pattern was recorded between 12 and 22 min after the beginning of the nitriding process, with a final

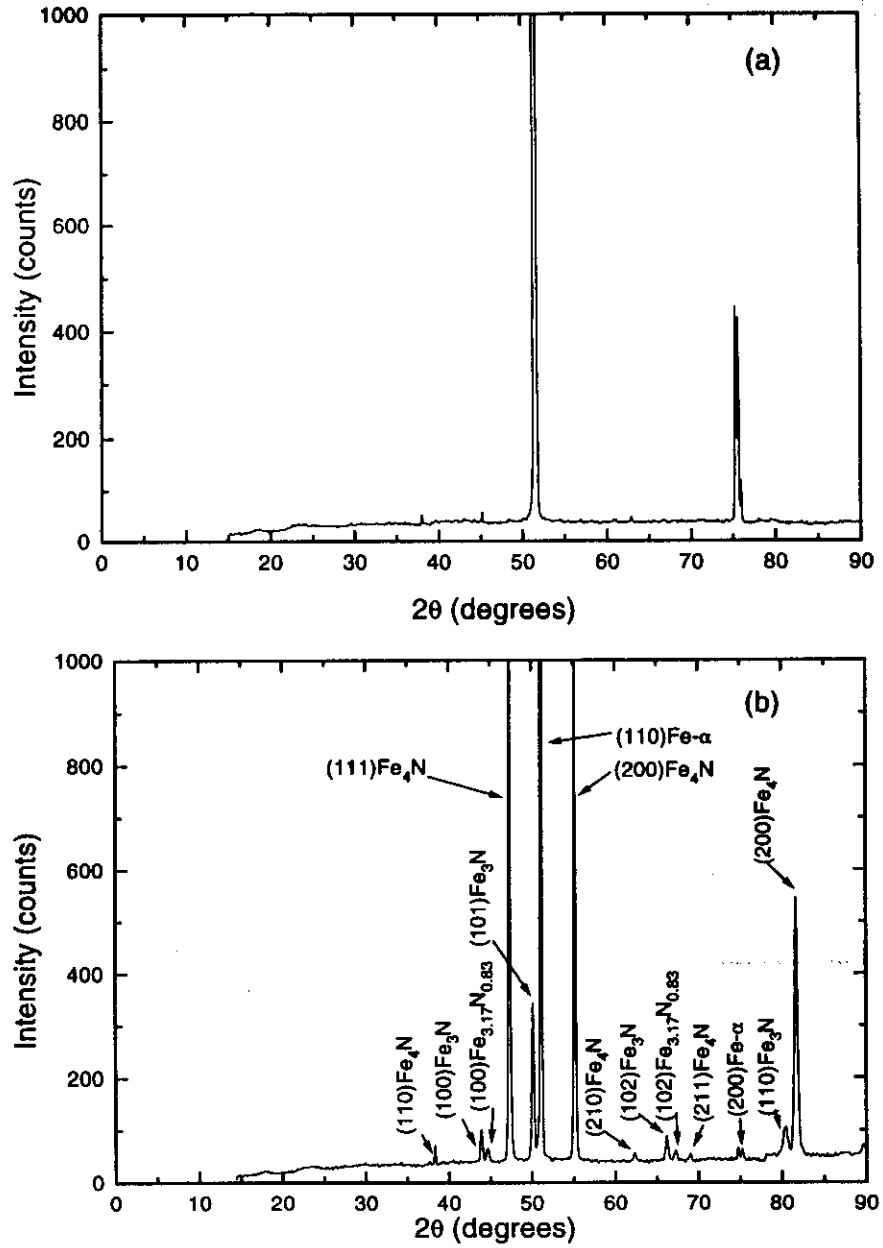

Figure 5. (a) X-ray diffraction pattern of the non-treated sample at room temperature (a-1), before the beginning of the ion nitriding process. Only Bragg reflections corresponding to the Fe-α phase are present. Other peaks like those at 38°, 45° and 63° can be attributed to iron oxides and impurities. (b) X-ray diffraction pattern recorded at the end of the nitriding process at 410 °C (a-13), after 2.5 h of processing. The Fe-α (200) splitting can be attributed to statistical fluctuations of a low-intensity peak. The identified phases are indicated. The intensities (vertical axes) are displayed on a linear scale.

temperature of 367 °C. In addition to the peaks corresponding to the Fe-α phase already observed in a-1, the incipient presence of peaks at 47.3°, 49.8°, 55.2° and 81.7° is apparent. The peaks at 47.3°, 55.2° and 81.7° correspond to the (111), (200) and (220) reflections from a Fe_4N-γ' phase, and the peak at 49.79° corresponds to the Fe_3N-ε hexagonal phase.

The pattern a-3 was taken between 23 and 33 min of the process with a final temperature of 395 °C. A comparison between a-3 and a-2 indicates that all peaks corresponding to the different nitrides strongly increase as the process evolves. In addition, in the particular case of the peak corresponding to the Fe_3N-ε phase, the angular position shifts towards $2\theta = 49.93°$. Besides the mentioned peaks, others appear at 2θ angles of 43.77°, 65.88° and 80.08° corresponding to the hexagonal (100), (102) and (110) reflections from the Fe_3N-ε phase, at 44.82° related to the (100) reflection from a $Fe_{3.17}N_{0.83}$-ε phase and at 62.3° associated with the (210) reflection from a Fe_4N-γ phase.

All diffraction peaks due to the different nitrides that can be seen in the a-4 pattern, recorded between 35 and 45 min of the process at a sample temperature of 407 °C, are also present in all the subsequent patterns. These peaks progressively increase in intensity as a consequence of the continuous growth of the volume fraction occupied by the different iron nitrides.

The shift in the angular position of some of the peaks towards higher 2θ angles from a-2 to a-3 was also observed in patterns a-4, a-5 and a-6. This behaviour is illustrated in

Table 2. The 2θ diffracted angles for the $Fe_{3.17}N_{0.83}$ and Fe_3N phases (for all the crystal orientations observed in our experiments) are displayed in roman font, corresponding to each different diffractogram identified with a-1 to a-13. The corresponding interplanar distances (d_{hkl}) computed using equations (2) and (3) are indicated for each case in italic font, with an error $\Delta d_{hkl} = 0.002$. It can be observed that the interplanar distance varies with the time of nitriding for the Fe_3N phase. This variation was observed up to the a-5 diffractogram, followed by an apparent stability until the end (a-13) of the processing. For the phase with nearest stoichiometry, $Fe_{3.17}N_{0.83}$, these interplanar distance variations, within the measurement errors, were not observed. The results for the a-7 to a-12 diffractograms are omitted.

	$2\theta/d_{hkl}$ (Å)							
Phases	a-1	a-2	a-3	a-4	a-5	a-6	...	a-13
Fe_3N (100)	—	—	43.77°	43.91°	44.98°	44.98°	...	43.91°
			2.361	*2.354*	*2.301*	*2.301*		*2.354*
$Fe_{3.17}N_{0.83}$ (100)	—	—	44.82°	44.75°	44.89°	44.75°	...	44.68°
			2.308	*2.312*	*2.305*	*2.312*		*2.315*
Fe_3N (101)	—	49.79°	49.93°	50.07°	50.14°	50.07°	...	50.14°
		2.091	*2.085*	*2.080*	*2.077*	*2.080*		*2.077*
Fe_3N (102)	—	—	65.88°	66.02°	66.16°	66.16°	...	66.23°
			1.618	*1.615*	*1.612*	*1.612*		*1.611*
Fe_3N (110)	—	—	80.08°	80.29°	80.36°	80.50°	...	80.50°
			1.368	*1.365*	*1.364*	*1.362*		*1.362*

table 2, which reports the 2θ angles and the corresponding d_{hkl} values corresponding to the different phases.

The variation in peak positions, indicating a progressive decrease in interplanar distances during the first minutes of the nitriding treatment, only occurs to (hkl) reflections corresponding to the Fe_3N phase and does not occur for all the others, even not to the $Fe_{3.17}N_{0.83}$-ε phase, as can be seen in table 2 for the (100) reflection.

4. Discussion

A shift in the 2θ angle position of the (110) reflection corresponding to the Fe-α phase between the first (a-1) and the last (a-13) x-ray diffraction was observed. The 2θ angles for the (a-1) and (a-13) diffractograms were 51.40° and 51.12°, respectively, which corresponds to a $\Delta 2\theta = 0.28°$. This value corresponds to an increase in interplanar distance $\Delta d_{110} = 0.006$ Å or a relative expansion of ≈0.5%. Considering that the experimental error in the 2θ determination was ±0.07 and taking into account equation (2), the error in d_{110} can be estimated to be ±0.002. Taking into account the fact that the temperature difference between the samples corresponding to the a-1 and a-13 patterns is ≈400 °C, the expected sample linear expansion, considering an average temperature dilatation coefficient of $\approx 13.5 \times 10^{-6}$ for the AISI 1010 steel, is ≈0.51%. Therefore, we conclude that the decrease in the peak angular positions of the reflections corresponding to the Fe-α phase is a consequence of the expected thermal expansion of the sample heated by the action of the nitriding process.

The other phases do not exhibit the same behaviour. Analysing, in particular, the case of the Fe_3N-ε phase, we remark that the angle associated with the (101) reflection in the a-2 pattern leads to a value of the interplanar distance $d_{101} = 1.152$ Å. This value is larger than that corresponding to the a-3 pattern, $d_{101} = 1.150$ Å, even though the a-3 pattern was recorded with the sample at a higher temperature.

The decreasing trend of d_{hkl} values corresponding to the Fe_3N phase is maintained for a-4 and a-5 and then approaches a nearly constant value (within the experimental errors) of $d_{hkl} = 1.146$ Å. Considering that the d_{101} modification for $t > 17$ min takes place for almost a constant temperature, this variation in interplanar distance cannot be attributed to thermal effects. The variation in d_{101} corresponds to a relative linear expansion of 0.52% (17 min), 0.31% (28 min) and 0.01% (38 min) with respect to the final state. This suggests that the initial Fe_3N phase is subjected to stresses producing a significant volume expansion which is progressively relaxed during the nearly isothermal conditions of the advanced stages of the nitriding process.

The particular behaviour observed for Fe_3N seems to be exclusive to this phase because the interplanar distances corresponding to the others, even $Fe_{3.17}N_{0.83}$-ε, remain constant from $t = 17$ min until the end of the process, as can also be seen in table 2.

5. Conclusion

A reactor chamber was constructed and installed in the synchrotron radiation SAXS beamline of LNLS, which was adapted for x-ray diffraction experiments. It first use was for an *in situ* study of the structural variations occurring in the surface structure of a AISI 1010 steel subjected to a nitriding process.

The decreasing intensity of the diffraction peaks corresponding to the Fe-α phase is a consequence of the decrease in its volume fraction, close to the sample surface, as a consequence of the formation of different iron nitrides. The observed increase in the interplanar distances, during the first stages of nitriding, agrees with the value corresponding to the expected thermal linear expansion effect.

The experimental results indicate the formation of three different nitrides, Fe_4N-γ and Fe_3N-ε in the first minutes and $Fe_{3.17}N_{0.83}$ later on.

During the nitriding process under nearly isothermal conditions ($t \gtrsim 20$ min) the interplanar spacing of all phases, except Fe_3N-ε, remains constant within the experimental error. The interplanar spacing in the Fe_3N phase exhibits a decreasing trend, probably due to the action of

stresses which progressively relax for increasing periods of time.

The effect observed for Fe_3N-ε does not occur in any other phase with nearly the same stoichiometry, i.e. $Fe_{3.17}N_{0.83}$-ε.

Acknowledgments

We are grateful to Javier Laverense for his assistance in the use of the image processing systems. This work was partially supported by IAEA (research contract No ARG 9384 R1), Agencia Nacional de Promoción de la Investigación Científica y Tecnológica (PIP No 602), Fundaciones Antorchas/Vitae (Project No. B-11487/6B002) and University of Rosario.

References

[1] Michel H, Czerviec T, Gantois M, Ablitzer D and Ricard A 1995 *Surf. Coating Technol.* **72** 103
[2] Bruzzoni P, Brühl S P, Gómez B J, Nosei L, Ortiz M and Feugeas J 1998 *Surf. Coating Technol.* **110** 13
[3] Bott A H, Brühl S P, Gómez B J, Zampronio M, Miranda P E, and Feugeas J. 1998 *J. Phys. D: Appl. Phys.* **31** 3469
[4] Cookson D J, Hunter B A, Kennedy S J and Garret R F 1998 *J. Synchrotron Radiation* **5** 926
[5] Kellermann G, Vicentin F, Tamura E, Rocha M, Tolentino H, Barbosa A, Craievich A and Torriani I 1997 *J. Appl. Crystallogr.* **30** 880
[6] Bougdira J, Henrion G, Fabry M, Remy M and Cussenot J R 1991 *Mater. Sci. Eng.* A **139** 15
[7] Brühl S P, Russell M W, Gómez B J, Grigioni G, Feugeas J N and Ricard A 1997 *J. Phys. D: Appl. Phys.* **30** 2917
[8] Inokuti Y, Nishida N and Ohashi N 1975 *Metal. Trans.* A **6** 773

Power Voltage Source Synchronized with a Spectrometer for Real-Time Spectroscopic Studies of Pulsed Discharges

Jorge N. Feugeas, Aldo Marenzana, Sonia P. Brühl, and Bernardo J. A. Gómez

Abstract—**The evolution of the species generated in a plasma may be characterized through real-time optical emission spectroscopy. Nevertheless, for experimental situations in which the light emission intensity is insufficient for acquisition times of several tens of milliseconds (typical resolution time of optical multichannel analyzers), some complementary instrumentation has to be incorporated. In this paper, we present the design of an experiment to study the spectroscopic evolution of a plasma during a switch-on of a dc discharge, and/or during its switch-off (afterglow). The solution consisted of a periodic discharge generated by a dc square wave voltage source, synchronized with the optical multichannel analyzer of the spectrometer through its TTL (logic family of Transistor–Transistor Logic) level pulse. The periodicity of the discharge under similar physical conditions allows accumulation the spectroscopic information for each cycle, making possible a time resolution of tens of milliseconds by increasing the resulting intensity profile of the spectra.**

I. Introduction

OPTICAL emission spectroscopy [1] is a powerful technique which can be widely used in many applications, among which plasma processing of materials is one of the more interesting examples. The plasma enhanced physical vapor deposition (PEPVD) [2], for example, is a process in which an electric discharge in a pure gas or mixture of pure gases is produced simultaneously with an evaporation of pure metallic species, giving rise to the molecular formation of compounds that can be deposited onto the surface of substrates, like the TiN or TiAlN coatings on steels. Another process is the plasma enhanced chemical vapor deposition (PACVD) [3] in which different compounds can be developed in the plasma by an electrical discharge in a mixture of reactive gases. The hydrogenated amorphous silicon through silane decomposition is an example. The plasma etching (physical and/or chemical) is a process in which the ions generated in an electrical discharge can remove atoms or molecules from a substrate surface (negative biased) through a simple collision process or by the volatile compound formation between the filling gas molecules or resulting radicals and the substrate atoms. These etching processes can be used in surface cleaning prior to surface treatments, or for the removal of selective material in compact integrated circuits (microelectronics).

Manuscript received July 15, 1997; revised December 21, 1998. This work was supported in part by IAEA under Research Contract RC/6477/R1/RB and by CONICET grants.

The authors are with the Instituto de Física Rosario, Universidad Nacional de Rosario-CONICET, 2000 Rosario, Argentina.

Publisher Item Identifier S 0018-9456(98)09931-8.

Ion nitriding (or nitrocarburizing) is another process in which the nature of the surface of certain materials, steel, for example, can be modified by the adsorption, and posterior diffusion into the bulk, of certain atomic species (like nitrogen and/or carbon) produced in the discharge into an appropriate mixture of gases [4]. This process, in which the affected layers can be thicker than 100 μm, has to be differentiated from others such as ion implantation in which the depths are of only a few microns [5], [6].

In all the above examples, the generated plasmas are out of thermal equilibrium, and the temperatures (ion and molecular temperatures) are close to room temperature. In this medium, the processes which produce spectroscopic emission (atomic, molecular and low ionization degrees electronic transitions, vibrational and rotational molecular band fine structure formation) are mainly dominated by electronic collision excitation.

During the discharge, it is of crucial importance to characterize, whatever the above processes may be, the atomic or molecular species formation (decomposition and recombination processes into the bulk of the plasma and/or as result of the plasma–surface interaction). Optical spectroscopy (such as in the emission or in the absorption mode) is the most important technique in the sense that it provides *in situ* information, has a good spatial definition, and does not perturb the system. The actual technology allows coverage from close to one hundred to several thousands of nanometers of wavelength radiation without excessively complicating the instrumentation. Compact monochromators, optical multichannel analyzers, luminic (UV, visible, and IR) conducts like optical fiber bunches, windows for different wavelengths range transmission, etc., are available economically from commercial sources.

Nevertheless, spatial and time resolutions are two factors that always need to be improved, depending on the nature of the experiment. The spatial resolution can be resolved by the size (cross section) of the optical fiber, but only along the perpendicular to the line of sight. Short focal length optical systems can help in the line-of-sight spatial resolution direction. The time resolution is linked to the use of the optical multichannel analyzers (OMA's) in which an array of photodiodes collects the diffracted light from a monochromator, integrating the information of several milliseconds. This time resolution can be improved by the use of electrooptical shutters which can reduce the exposure time to nanoseconds. Also, the problem derived from the natural light intensity reduction,

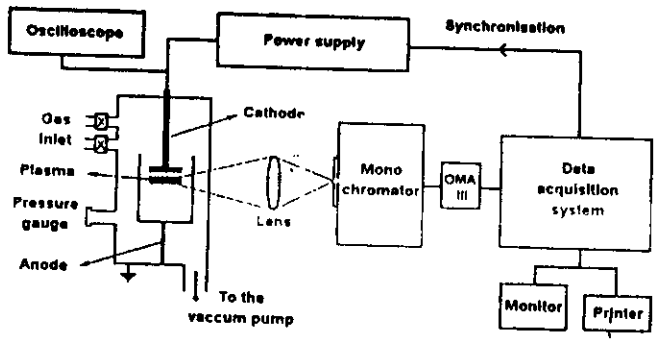

Fig. 1. Schematic view of the experimental setup.

associated with the short exposure time, can be compensated for by the use of light intensifiers.

In this paper, we describe an instrumental solution to the specific problem of the optical emission spectra evolution of plasmas generated in pulsed dc glow discharges in both parts of its cycle: glow and afterglow.

II. The Experimental Problem

A. The Plasma Reactor

The experiment (performed at the Instituto de Física Rosario) that motivated this work was a pulsed dc glow discharge, mainly used in processes of ion nitriding and nitrocarburising of steels [7]–[9]. In both cases, a mixture of pure gases (nitrogen, hydrogen, argon, methane, etc.) is introduced with controlled and continuous flow in a reactive chamber (vacuum chamber). The discharge is produced inside the chamber by a pulsed dc power supply, which provides a square wave with a variable frequency (between 0–1 kHz), variable time duration of the active part of the cycle, and variable amplitude (applied voltage) between 200–800 V. In the normal mode of operation, the electrode configuration consists of a circular flat surface 50 mm in diameter, the cathode (to which the samples are fixed during the processes of nitriding or nitrocarburising), and a cylindrical stainless-steel cage (inner diameter of 60 mm and 120 mm in length), which provides the grounded anode. In Fig. 1, a schematic view of the experiment is presented.

Under these experimental conditions, and for total filling pressures above 0.5 mbar, a well-defined negative glow is developed close to the cathode surface. It is in this region of the discharge where the reactions (molecular decomposition and recombination) are produced, generating ionic species which are accelerated to the cathode through the cathode fall voltage. These species are responsible for surface modification.

In this medium, the species evolution is virtually the same in every cycle of the discharge, at least within several minutes, because the starting physical conditions in each cycle are virtually the same. Each cycle lasts several milliseconds, a short enough time to keep the basic physical conditions unchanged to the next cycle, considering the low energy involved in our experiment. Those physical conditions are the nature of the gas mixture, the partial pressure of each filling gas, the substrate composition, the concentration of sputtered atoms from the surface in the plasma, and the substrate temperature, etc. As an example, the temperature (when the experiment reaches the steady state) can change only several degrees within tens of minutes of processing, and the nature of the substrate surface (composition of the surface layers) can change significantly in only tens of minutes. This fact enables the study of the evolution of the plasma composition and other properties in one cycle through the addition or the average of the results obtained in several consecutive cycles. The number of cycles to scan can be determined through the compromise solution between the good statistic of the accumulated results and the possible modification of the general experimental conditions due to the length of the data acquisition time.

B. The Spectrometer

To characterize the full process of an experiment like the one described above, where it is necessary to study the formation and the temporal evolution of the species in a plasma, optical emission spectroscopy is the natural and most important experimental method, mainly because it does not interact with the system (nonperturbative method). In our case, we used a Princeton Applied Research optical spectrometer, which comprises a triple grating monochromator (Jarrell Ash 27 monospec) of focal length 275 mm, and an optical multichannel analyzer (1024 cooled photodiodes) OMA III from Princeton Electronics, which are set by means of an optical lens to detect the plasma glow near the cathode. By imaging the plasma glow on the entrance slit of the spectrometer, the total discharge emission in the negative glow or in the afterglow is detected from a distance of about 1 cm from the cathode surface with an integrating time of 30 ms.

This spectrometer works with a base exposure time of 30 ms composed of 28.67 ms of scanning time and 1.33 ms of overhead time. The scanning time is the time in which the information of a complete spectrum is stored by the 1024 photodiodes, being two consecutive periods separated by an overhead time. The scanning can be active (active scan) where the information is stored, or inactive (ignored scan) when no information is stored. The OMA can be set to different data acquisition modes. It can be programmed to control a predetermined number of successive active scans (one or more) adding their results, virtually increasing the acquisition time by a multiple of 30 ms. On the other hand, it is possible to control dead periods by the accumulation of one or more ignored scans, in which no spectral information is stored. These active and dead periods can also be periodically interspersed through an appropriate OMA mode programming.

In addition to the single operation of spectra storing corresponding to each active period (successive active scans), the software which controls the OMA operation allows the addition or subtraction of spectra as desired for a determined purpose, giving a composed line and band intensity profile. The subtraction of a previously stored spectrum allows, for example, partially eliminating the background light in spectra of experiments where the emission intensity is comparable to the radiation intensity emitted by the environment. In these cases, before or after the experiment, a spectrum of the region

to be studied is stored from the same spectrometer operating conditions (number of active and ignored scans, etc.), but without running the experiment. This background spectrum (normally noisy continuous spectra) can then be subtracted from the one obtained during the experiment, with the natural background light reduction.

The OMA III also provides as output, together with the information of each cycle composed by the 29-ms scans (active and/or ignored scans) plus the 1 ms of dead time between them, a time mark coincident with the beginning of each active scan. This time mark (TTL level pulse) consists of a sharp voltage peak (3 V of amplitude and 1 μs wide) destined to be used externally for synchronism purposes. Both the cyclic signal and the time mark can be monitored through the use of an oscilloscope.

The low energy of the discharge used in the experiment generates a plasma whose optical emission intensity is not adequate to produce single spectra (30-ms accumulation time) to be studied. Even the more intense emission lines and bands are too faint to be used to study their profiles and their time variation in each cycle of the discharge. In addition, the background light (even in the dark room condition) and the natural noise of the photodiodes array detection give a background signal (continuous spectrum characteristics) of an intensity which can be comparable with the intensity of the weaker faint peaks of the plasma emission spectrum.

To solve these experimental problems, we worked through the accumulation of the information of several cycles of the discharge, and the subtraction of the information of the background radiation from the resulting spectra also accumulated during a time equivalent to the number of scanned cycles.

The last procedure is contemplated in the OMA functioning program (as described above). The solution to the first problem, which involves the development of an external additional instrumentation, is the subject of this paper.

III. The Design of the Experimental Solution

To study the optical emission spectra evolution of the discharge, the experiment was diagramed for adaptation to the OMA operational characteristics. A square wave dc power supply was specifically designed with the following operating characteristics:

a) Frequency of the power supply (square wave): 16.67 Hz.
b) Active part of the discharge (glow): variable between 1–60 ms.
c) Voltage amplitude: variable between 0–600 V.
d) Discharge current: between 10–200 mA.

The frequency of 16.67 Hz, which corresponds to a period of 60 ms (twice the scanning time of the OMA), can be corrected for synchronism purposes through an external trigger source with a delay control. Once the active/dead (glow/afterglow) ratio for the operating conditions of the power supply and the amplitude is fixed, the discharge will be established and the experiment will run automatically without modifications. Nevertheless, for the acquisition of emission spectra from the plasma at a certain time interval within a discharge cycle, the power supply can be synchronized through the OMA TTL level pulse output (available at the beginning of each active scanning period) in the following way: the OMA is programmed to operate with one active scan, followed by one (or more) ignored scans. The TTL level pulse is connected to the power supply as the external trigger source for synchronism purposes, selecting the appropriate delay to make the beginning of the active scan coincide with the beginning of the period of the discharge cycle in which the spectrum wants to be sampled. After each active scan (in which one complete spectrum is stored), one ignored scan follows, giving time for the beginning of a new active scan with the same conditions as the preceding, being each active scan synchronized by the TTL level pulse originated in the preceding one. One active scan plus one ignored scan gives a periodicity of 60 ms, which is the period of the discharge. The resulting spectrum (S_i) corresponds to the addition of the successively recorded active scans.

The total number of active scans used in each experiment depends on several factors such as the radiation intensity of the plasma, the possibility of changes in the experimental conditions during the total time involved, etc. Normally, in our experiments, we used several thousand scans involving an integrated time of several minutes (typically 5 min).

After each experiment, a similar routine (total number of scans) was performed on the experimental system but without the discharge (power supply off), with background spectrum (S_{bg}) recording purposes. S_{bg} was then subtracted from the primary S_i, giving the final spectrum $S_f = S_i - S_{bg}$, with a better signal-to-noise ratio (SNR).

As an observation over the synchronism in the periodic scanning of the cyclic discharge, we can say that every spectrum is taken under similar conditions due to the TTL level pulse triggering function, except for the first scanning that can be randomly produced at any part of the periodic discharge. This occurs due to the lack of a preceding active scan with the corresponding TTL level pulse. Nevertheless, the number of active scans is large enough (normally several thousand) to negate the influence of a single spectrum taken out of the preselected part of the cyclic discharge.

IV. Instrumentation

A power supply [10] was developed which provides periodic pulses of voltage with a fixed frequency and which can be programmed with a delay relative to an external signal of synchronism and for a predetermined duty cycle.

The circuit of the power supply, which is shown in Fig. 2, can be separated in two parts: (a) power and (b) control.

A. Description of the of the Power Circuit

The power circuit consists of a dc source, variable from 0 to 600 V, with a maximum of 200 mA, commanded by a power switch that produces the instantaneous connection and disconnection to the load.

The dc source is basically composed of a variable autotransformer (220/0–250 V) connected to a 220/600 V transformer, with a bridge type rectifier and filtered with electrolytic capacitors of 220 μF–450 V, to provide the necessary filtering

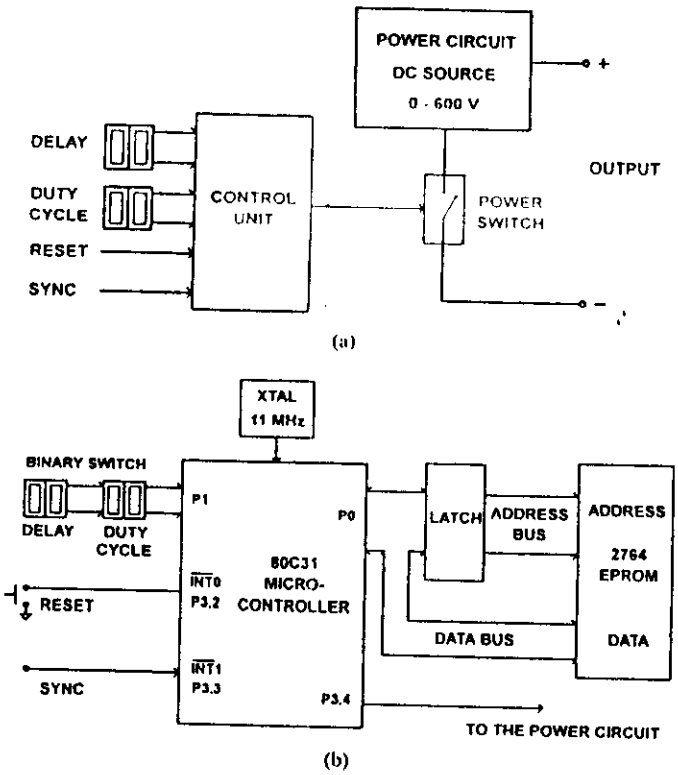

Fig. 2. (a) Power supply circuit. (b) Control unit of the power supply circuit.

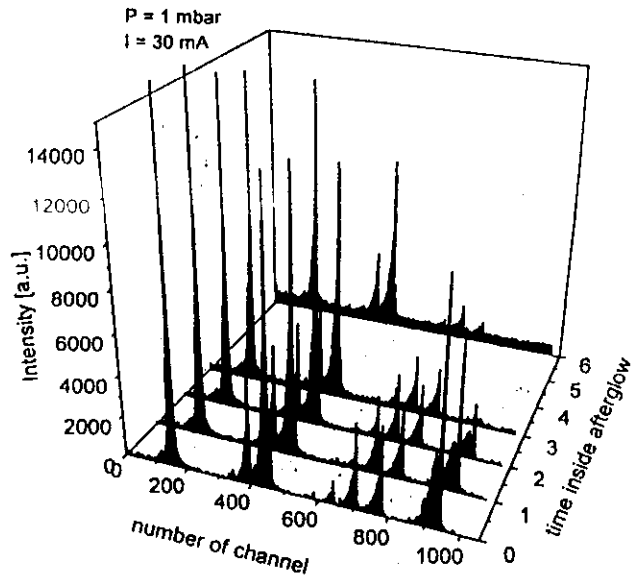

Fig. 3. Spectra evolution for $D_t = 0, 1, 2, 3$ and 6 ms after the beginning of the afterglow. Experiments were performed with discharges, at 1 mbar of pure nitrogen, of a dc square wave 16.67 Hz, 40% active and 500 V of amplitude, total current 30 mA. Note the decreasing intensity with D_t of the band heads, corresponding to the 0–0 transition of N_2^+ ($\lambda = 337.13$ nm) and N_2 ($\lambda = 391.44$ nm).

with the required ripple (<2%). A BU208A transistor power switch, activated from the control unit, was used.

B. Description of the Control Unit

The control unit has an Intel 80C31 microcontroller, which allows control of the duty cycle and the delay, and the synchronism with the external signal. These settings provide control of the power switch to obtain the required working cycle.

The microprocessor read, in a multiplexed way and through the input port, the data of the binary switches; through one pair of switches the data of the effective duty cycle (in percentage) and through the other pair of switches the delay (in milliseconds) to the synchronism signal. The program which performs the operation is contained in the 8-kbyte EPROM memory 2764, connected to the microcontroller by the address bus through the latch and by the data bus directly, such as suggested in the INTEL application notes [11].

For better operation of the system, the microcontroller reads new preset inputs when a signal is sent by means of a pulsed switch. This produces a priority interruption of the system, introducing it into a new routine charged to read and calculate the new variables. In Fig. 2(b), the circuit of the control unit is shown.

V. Results and Conclusions

The method and instrumentation were successfully used in the spectroscopic study of the afterglow of a pulsed discharge to determine the formation and decomposition of molecules and radicals through the line and band profiles evolution. As an example, we present the results of experiments performed with discharges in pure nitrogen at 1 mbar of pressure. The voltage used was a periodic square wave of 16.67 Hz of frequency, with 40% of each cycle active and 60% inactive, and with an amplitude of 500 V. The resulting total current circulating through the plasma was 30 mA.

The active scans of the spectrometer were synchronized beginning at different times Δt after the end of the active cycle. In Fig. 3, the spectra evolution for $\Delta t = 0$, 1, 2, 3, and 6 ms are shown in a 3-D plot.

These experiments were performed within half an hour without interrupting the process of the discharge, with only modification of the delay for the different preselected Δt. This allows use of this method to control the spectroscopic characteristics of plasmas in processes where continuity is necessary, such as the aforementioned examples of surface treatment by plasmas, and have a fast and periodical modification of the voltage–current characteristics.

Acknowledgment

The authors would like to thank G. Pochettino for his valuable collaboration in the development of the instrumentation.

References

[1] A. Ricard, J. E. Oseguera Pena, L. Falk, H. Michel, and M. Gantois, "Active species in microwave postdischarge for steel-surface nitriding," *IEEE Trans. Plasma Sci.*, vol. 6, p. 18, 1990.
[2] K. S. Fancey and A. Matthews, "Evaporative ion plating: Process mechanisms and optimization," *IEEE Trans. Plasma Sci.*, vol. 18, p. 869, 1990.
[3] J. Chin, *Advanced Surface Engineering*, W. D. Sproul and K. O. Legg, Eds. Gaithersburg, MD: NIST, 1994, p. 65.
[4] R. Grün and H. J. Günther, "Plasma nitriding in industry—Problems, new solutions and limits," *Mater. Sci. Eng.*, vol. A140, p. 435, 1991.

[5] J. N. Feugeas, G. Sánchez, C. O. de Gonzalez, J. D. Hermida, and G. Scordia, "Pulsed ion implantation of nitrogen in pure titanium," *Radiation Effects and Defects in Solids*, vol. 128, p. 267, 1994.
[6] G. Sánchez and J. Feugeas, "Thermal evolution of targets under plasma focus pulsed ion implantation," *J. Phys. D: Appl. Phys.*, vol. 30, pp. 927–936, 1997.
[7] J. Bougdira, G. Henrion, and M. Fabry, "Effects of hydrogen on iron nitriding in pulsed plasmas," *J. Phys. D: Appl. Phys.*, vol. 24, p. 1076, 1991.
[8] S. P. Brühl, G. Sánchez, J. N. Feugeas, C. Oviedo, and P. E. V. de Miranda, "Change on the hydrogen permeability in steel induced by pulsed ion nitriding," *Anales de la Asociación Química Argentina*, vol. 83, no. 5, pp. 237–241, 1995.
[9] C. Ruset, A. Bloyce, and T. Bell, "The influence of cooling rate on the microstructure of plasma nitrocarburised compound layers," *Heat Treatment of Metals*, vol. 4, p. 95, 1995.
[10] R. Hugon, M. Fabry, and G. Henrion, "The influence of the respective dutarions of the discharge and the afterglow on the reactivity of a DC pulsed plasma used for iron nitriding," *J. Phys. D: Appl. Phys.*, vol. 29, p. 761, 1991.

Jorge Feugeas was born in Rosario, Argentina. He received the Ph.D. degree in physics from the University of Buenos Aires. His doctoral work concerned Z-pinch experiments, which were performed at the Stevens Institute of Technology, Hoboken, NJ.

His field of research is experimental plasma physics. He is currently principally oriented in the surface treatment of materials. He is a Professor at the University of Rosario, Rosario, Argentina, in the undergraduate courses of Licenciatura in physics and in the physics doctoral program. He is Vice-Director of the Rosario Institute of Physics (National Council of Scientific and Technological Research). He is President of the Technological Entail Unity ACIFIR and is Head of the Plasma Physics Laboratory. He works with the industry in the development of systems and processes for surface treatment of materials. He has been a Visiting Professor at Stevens Institute of Technology, the Laboratoire de Physique de Gaz Ionisee et de Plasmas at the Universite Paris Sud, Paris, France, and the COPPE, Universidad Federal de Rio de Janeiro, Brazil.

Dr. Feugeas is the President of the SAM-Asociacion Argentina de Materiales/Materials Research Society of Argentina.

Aldo Marenzana was born in Rosario, Argentina, in 1958. He received the degree in electronical engineering from the Universidad Nacional de Rosario in 1984.

Since 1985, he has been working on design electronics instruments in the Instituto de Ffsica Rosario, Universidad Nacional de Rosario.

Sonia P. Brühl received a degree in physics from Universidad Nacional de Rosario, Rosario, Argentina in 1991 and the Ph.D. degree in physics from the same university in 1995.

In 1997, she was at IOPW, Technic University of Braunschweig, Germany, for six months on a research scholarship. Her major field of specialization is plasma physics with application to surface treatments, especially ion nitriding of steels, and also optical emission spectroscopy of gaseous discharges used in surface modification processes. She has published several papers in international journals and at the moment is a Full Professor and Researcher at the National Technological University in Concepción del Uruguay, Entre Rios, Argentina.

Bernardo J. A. Gómez received the B.A. degree in physics from the Universidad Nacional de Rosario, Rosario, Argentina, in 1995. He is currently working toward the Ph.D. degree at the same university. His dissertation topic is "Spectroscopic studies of pulsed discharges used in steel nitriding and mechanical properties modification."

J. Phys. D: Appl. Phys. 31 (1998) 3469–3474. Printed in the UK PII: S0022-3727(98)92270-7

Pulsed-plasma-nitrided API 5L X-65 steel: hydrogen permeability and microstructural aspects

A H Bott†, S P Brühl‡, B Gómez‡, M A Zampronio§, P E V Miranda† and J N Feugeas‡

† PEMM-COPPE/UFRJ, CP68505, CEP21945-970, Rio de Janeiro RJ, Brazil
‡ IFIR (CONICET-UNR) Boulevard 27 de Febrero 210 bis, 2000 Rosario, Argentina
§ DFI/UEM, Avenida Colombo 5790,CEP87020-900, Maringá PR, Brazil

Received 6 March 1998, in final form 20 July 1998

Abstract. Nitriding of an API 5L X-65 steel was performed using a low-frequency dc pulsed-plasma technique. A 6 h treatment was found to produce a compact surface nitride layer composed of γ' (Fe_4N) and ε ($Fe_{2-3}N$) nitrides with a thickness of around 2 μm. The plasma-nitriding treatment resulted in a significant reduction in hydrogen permeability, from 2.97×10^{-10} mol H m^{-1} s^{-1} (for the untreated steel) to 7.1×10^{-11} mol H m^{-1} s^{-1} for electrolytic hydrogen charging via the nitrided surface. When the sample was oriented with the nitrided surface as the hydrogen-exit face, the permeability was reduced even further, to 3.9×10^{-13} mol H m^{-1} s^{-1}.

1. Introduction

Nitriding has long been recognized as an efficient surface-hardening treatment for steels, producing a surface nitride layer whose presence results in significant improvements in fatigue, wear resistance and corrosion resistance. The last 25 years have seen a growing replacement of the traditional industrial nitriding methods (which relied on relatively long treatments using gaseous ammonia or liquid cyanide salts) by the more modern ion-nitriding techniques [1]. This form of nitriding exploits the active species resulting from the ionization of nitrogen from pure molecular gas or in gaseous mixtures containing nitrogen. By applying a dc voltage, under low-vacuum conditions, between the workpiece (cathode) and the furnace's wall (anode), the atoms and molecules of the treatment gas can be excited and ionized, producing a luminous 'glow discharge' from which positive ions in the plasma are attracted to and occluded into the negatively charged workpiece's surface.

Commercial applications of such plasma techniques continue to grow, not only because of the inherent labour savings and shorter treatment times involved, but also due to the virtual elimination of associated environmental pollution and very significant reductions in energy consumption. Furthermore, new benefits are being identified which may lead to the even greater exploitation of ion nitriding in the fabrication of industrial components. One such benefit is the reduction of hydrogen permeability in steels as a result of ion nitriding [2, 3], thereby potentially offering a means of minimizing contamination with hydrogen and the subsequent embrittlement of steel components operating under hydrogen-rich service conditions [3–5].

In contrast to the ion nitriding with dc glow discharges in which a constant voltage is applied between the electrodes, the current paper reports some of the initial results obtained in a continuing study of ion nitriding in the surface engineering of API 5L X-65 steel to 'Tailor' permeability to hydrogen with a modulated dc glow discharge [6]. The modulation consists of a square-wave voltage applied between the electrodes, in which the sample is always at positive potential during the active part of each cycle. This technique is known as a dc pulsed glow discharge and it guarantees a high nitriding efficiency and a better control of the variables of the process.

2. Experimental procedures

The base material used for pulsed plasma nitriding was an API 5L X-65 steel, the chemical composition of which is detailed in table 1. Samples of 1 mm thickness were prepared from the bulk material and polished on both faces, using the standard metallographic techniques, before being subjected to the nitriding treatment.

Nitriding was performed using the equipment developed by the Plasma Physics Group at the IFIR. A schematic illustration of the nitriding plasma reactor is shown in figure 1. The reactor consists of one stainless steel circular planar electrode 6 mm thick and 35 mm in diameter (the sample holder), located inside the cavity of the other, a cylindrical cage 50 mm in diameter and 130 mm long

0022-3727/98/243469+06$19.50

Table 1. The chemical composition of the API 5L X-65 steel used in this study (weight %).

Element	Amount	Element	Amount
C	0.11	Al	0.035
Mn	1.05	Nb	0.032
S	0.005	V	0.055
P	0.014	Ti	0.01
Si	0.29	Ca	0.0074
Ni	0.15	Fe	Balance
Cr	0.31		

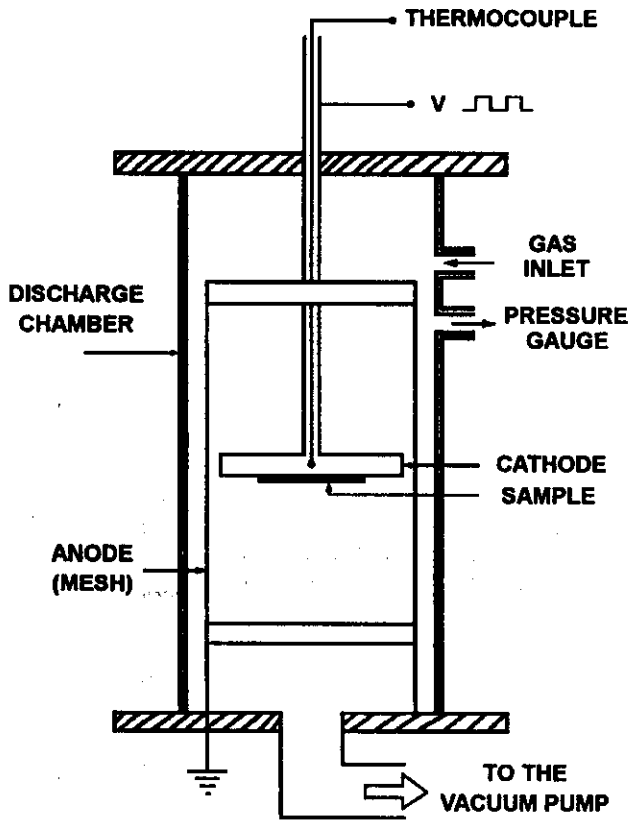

Figure 1. A schematic illustration of the plasma-nitriding reactor.

built of a stainless steel grid. The sample's electrode was negatively biased (the cathode) and the cage (anode) is at ground potential. The electrodes were located in a cylindrical Pyrex glass vacuum chamber (70 mm in diameter and 290 mm long).

The cathode is connected to the power supply through a cylindrical hollowed stainless steel rod which allows the introduction of a thermocouple to monitor the temperature of the electrode in the plasma region. The rod is completely covered by a Pyrex pipe, avoiding the generation of plasma along its surface and ensuring that the discharge is being generated only around the surface of the cathode's planar disc (25 cm^2).

Prior to introducing the process gases, the chamber was evacuated to a base pressure of 15 mTorr (2 Pa). Using a flowing gaseous mixture of 80 vol% N_2 and 20 vol% H_2, voltage 400 V, frequency 100 Hz and relative active period 50%, the samples were treated for 6 h, under a total pressure of 4 Torr (433 Pa). The current density in the sample during the active part of the cycle of the discharge was 4.2 mA cm^{-2} and the temperature of the process was 430 °C.

The nitrided layer produced was characterized using grazing incidence x-ray diffraction (GIXD), scanning electron microscopy (SEM) using a Zeiss DSM960 and microhardness profiling. GIXD diffraction spectra were recorded using a Siemens D-5000 x-ray diffractometer. The operating parameters were Cu Kα radiation (λ = 0.15406 nm), tube voltage, 40 kV, tube current 30 mA, 2θ scan range 0–120°, step size 0.050°, step time 2 s, divergence slit 0.270° and antiscatter slit 0.270°.

After recording rocking curves to calibrate the equipment for the precise alignment of samples, GIXD diffraction spectra were obtained for two different incidence angles, 0.6° and 2° (corresponding to approximate penetration depths of 50 and 200 nm analogous to the work reported by Jagielsky *et al* [7]). Spectra were also obtained for 10° and 30° using the same test parameters.

Microhardness measurements were made using a Shimadzu 2000 automated microhardness system with a Knoop indenter at a load of 5 g, aligning the long axis of the indenter parallel to the sample's surface for the through-thickness hardness profiles. The measurements of the hardness of the surface nitride layer were made on the treated surface itself (perpendicular to the polished transverse section utilized for the other points of the hardness profiles). The first sub-surface indentations were made at a depth of 7 μm below the outer face; subsequent measurements were made at 15 μm intervals.

Hydrogen-permeation parameters were determined using electrochemical hydrogen-permeation tests, the necessary cathodic charging potentials being obtained from the results of prior potentiodynamic polarization scans. All electrochemical tests were performed using a TAI GP-201H programmable electrochemical interface (galvanostat/potentiostat/zero-resistance ammeter) which permitted fully automated control and on-line monitoring of all test parameters as well as data acquisition via a microcomputer. Details of this technique and equipment can be found in [8, 9].

The hydrogen permeation tests were undertaken utilizing a two-compartment electrochemical cell (one for generation of hydrogen and the other for hydrogen detection) both containing 0.1 N NaOH electrolyte solution. Thermostatic control of the cell maintained a temperature of 50 °C throughout the tests. Cathodic hydrogen-generation potentials of 1.30 V versus the standard calomel electrode (SCE) and 1.36 V versus the SCE were used for the untreated and nitrided samples, respectively.

In the permeation test, the sample, of 13 mm diameter and 1 mm thickness, is positioned between the two compartments and a constant cathodic potential is applied in the generation compartment. In the detection compartment, potentiostatic control is maintained at a level equivalent to that of the open circuit (to oxidize hydrogen arriving at the sample's surface after permeating through from the generation side). Since the current required to maintain a constant detection potential is proportional to the flux

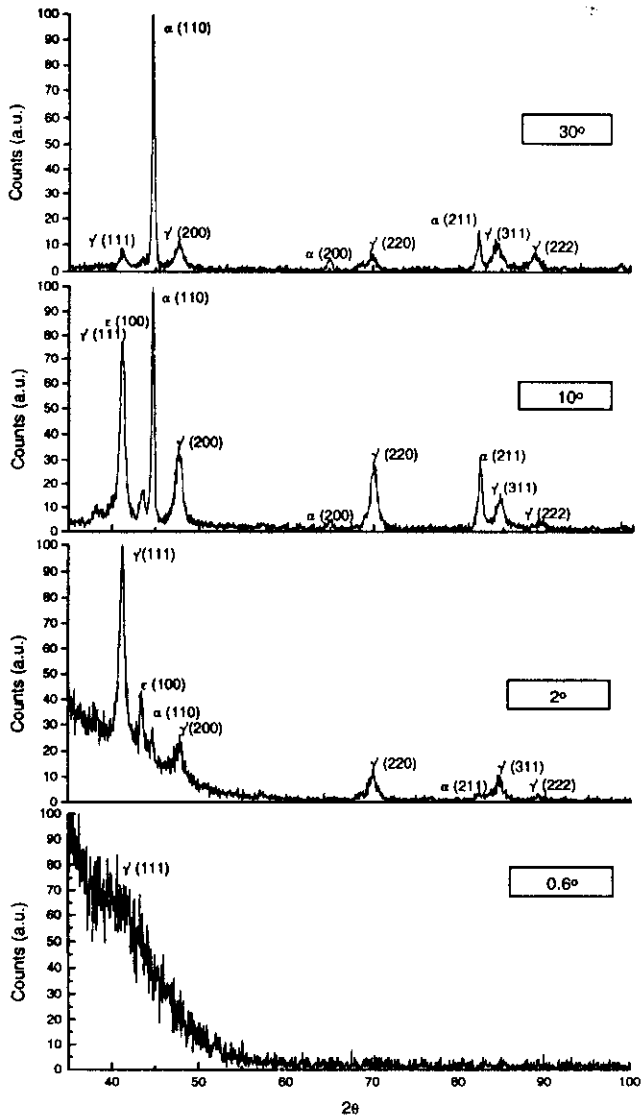

Figure 2. X-ray diffractograms of the 6 h plasma-nitrided API 5L X-65 steel; for incident beam angles of 0.6°, 2°, 10° and 30°.

of hydrogen which permeates through the sample, the analysis, via Fick's laws, of a curve plotting the evolution of this current with time permits the determination of the permeability, diffusivity and solubility of hydrogen in the material being tested.

Tests were undertaken on samples of the API 5L X-65 steel under the untreated and the 6 h plasma-nitrided conditions. In the latter case tests were performed for two distinct sample orientations; with hydrogen charging via the nitrided face via the untreated face of a nitrided sample.

3. Results

Figure 2 shows the x-ray spectra for incident-beam angles of 0.6°, 2°, 10° and 30°. Although the first spectrum is inconclusive, probably due to the microscopic roughness of the surface nitride layer, the spectra for 30°, 10° and 2° clearly show peaks due to the γ' nitride Fe_4N and the ε nitride Fe_2N_{1-x}. As the angle of incidence utilized to obtain the spectra was increased, thereby sampling a greater depth, an increasing contribution for the ferrite α peaks became evident.

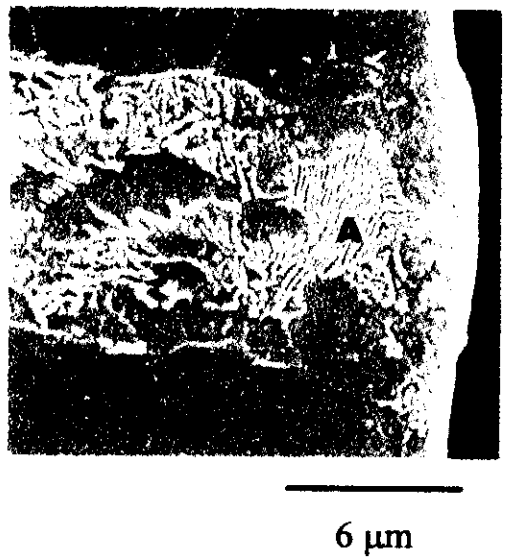

Figure 3. A scanning electron micrograph of a transverse section adjacent to the untreated face of the API 5L X-65 6 h plasma-nitrided steel showing the ferrite–pearlite structure (A) of the base material.

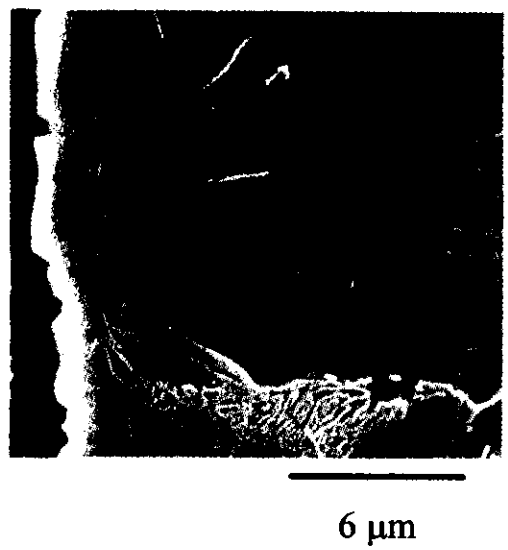

Figure 4. A scanning electron micrograph of a transverse section adjacent to the treated face of the API 5L X-65 6 h plasma-nitrided steel showing, in addition to the ferrite–pearlite structure of the base material, the surface (γ' and ε) nitride layer and an intergranular acicular phase ($Fe_{16}N_2$).

Figure 3 presents a scanning electron micrograph of a polished and chemically etched transverse section of one of the plasma-nitrided samples. In this case the ferrite–pearlite structure in a region close to the untreated face of the sample is shown. (The lighter contrast at the sample edge merely reflects a slight rounding off during polishing.)

Figures 4–6 show various aspects of the microstructure of the same section but adjacent to the treated face of the

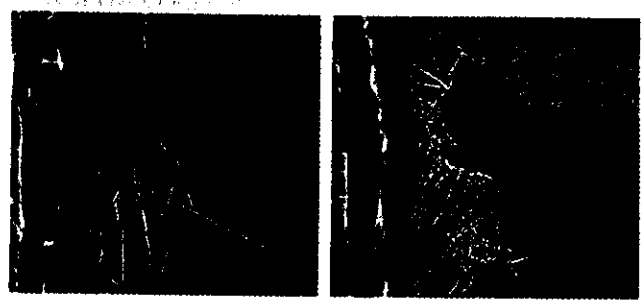

Figure 5. A scanning electron micrograph of a transverse section adjacent to the treated face of the API 5L X-65 6 h plasma-nitrided steel, showing that the intragranular acicular phase ($Fe_{16}N_2$) is present to a depth of around 20 μm (a). In another region a pearlite colony where α'' was not formed can be observed (b).

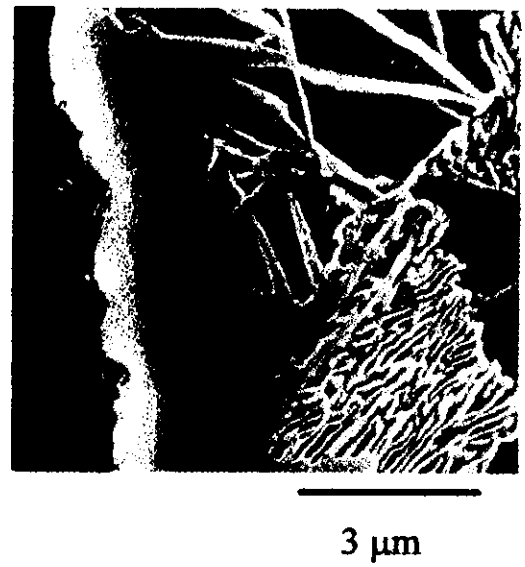

Figure 6. A scanning electron micrograph of a transverse section adjacent to the treated face of the API 5L X-65 6 h plasma-nitrided steel, showing the interaction between the surface (γ' and ε) nitride layer (E) and the cementite (Fe_3C) of a pearlite colony (A).

sample. A surface ($\gamma' + \varepsilon$) nitride layer (indicated by the x-ray diffraction results) of around 2 μm thickness is clearly shown in figure 3, as well as an intragranular acicular phase typical of $Fe_{16}N_2$ in such materials [3,4]. The presence of this acicular phase was observed only to depths of around 20 μm, as shown in figure 5 (in some areas on these micrographs the surface nitride layer had been separated from the substrate during polishing). Figure 6 shows the surface nitride layer at a higher magnification, in a region where this layer came into contact and interacted with the cementite of a pearlite colony.

A further scanning electron micrograph is included (figure 7) in order to show the orientation and size of the 5 g Knoop hardness indentations (used in obtaining the microhardness profiles) relative to the phases present in the microstructure at the treated face of the sample. The microhardness profiles themselves are shown in figure 8,

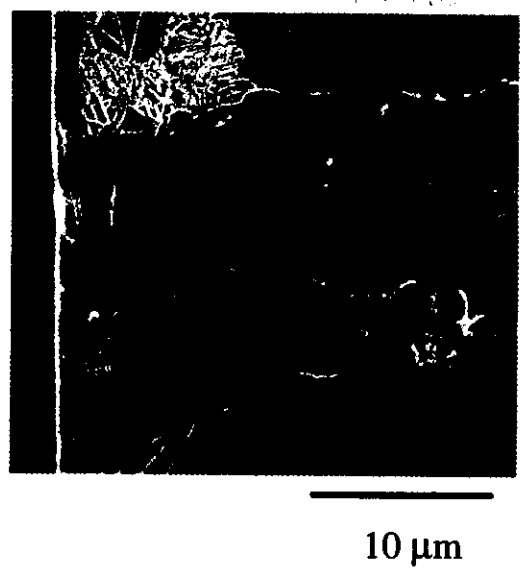

Figure 7. A scanning electron micrograph of a transverse section adjacent to the treated face of the API 5L X-65 6 h plasma-nitrided steel, showing the size and orientation of the Knoop hardness indentations (marked 'K') utilized in determining the microhardness profiles in relation to the phases present.

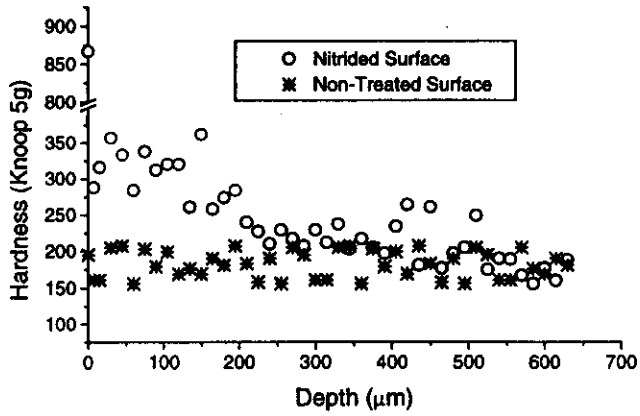

Figure 8. Knoop (5 g) microhardness profiles perpendicular to the treated and untreated faces of the API 5L X-65 steel.

for traverses perpendicular to the treated and untreated faces of the sample. The base material exhibited Knoop hardness values in the range 150–220, whereas the 2 μm nitrided surface layer was much harder with values ranging from around 600 to over 1200, with an average of 870. Immediately below the nitride layer, the Knoop hardness was found to be in the range 280–360. By a depth of 250 μm it was approaching the base metal hardness, further decreasing gradually until, at around 550 μm, the hardness was equal to that of the untreated face and in the sample's bulk.

The hydrogen-permeation curves are presented in figure 9. There is a marked difference between the curves corresponding to the plasma-nitrided samples and that for the untreated material, the nitriding treatment having provoked a significant reduction in the hydrogen permeability. Table 2 presents the calculated hydrogen permeation parameters [3,8,9].

Table 2. Hydrogen-permeation parameters calculated for the API 5L X-65 steel from the data presented in figure 9.

Material	Plasma-nitriding time (h)	Diffusion coefficient D ($m^2\ s^{-1}$)	Hydrogen solubility S (mol H m^{-3})	Steady state hydrogen permeability P_∞ (mol H $m^{-1}\ s^{-1}$)
Untreated steel		$D_s = 1.56 \times 10^{-10}$	$S_s = 1.9$	$P_{\infty S} = 2.97 \times 10^{-10}$
Nitrided steel	6			$P_{\infty ns} = 7.1 \times 10^{-11}$
				$P_{\infty sn} = 3.8 \times 10^{-13}$

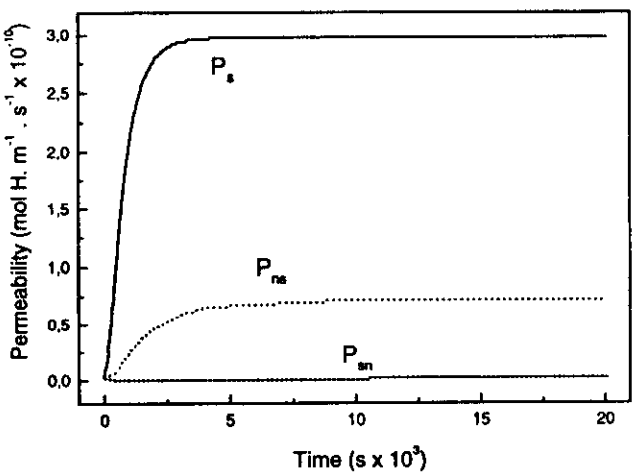

Figure 9. Hydrogen-permeation curves for the API 5L X-65 steel: P_s is an untreated sample, P_{ns} is a 6 h plasma-nitrided sample tested with generation of hydrogen at the nitrided face and P_{sn} is a 6 h plasma-nitrided sample tested with generation of hydrogen at the untreated face.

4. Discussion

The x-ray diffraction spectra clearly indicate that the 2 μm surface nitride layer observed by scanning electron microscopy is composed of the face centred cubic γ' (Fe_4N) and hexagonal close packed ε (Fe_2N_{1-x}) iron nitrides. The relative intensities of the peaks suggest that the γ' phase predominates. This is not dissimilar to results presented previously [2, 3] for the same material after plasma nitriding at a higher temperature by a more conventional continuous dc plasma technique. In the case of the previous work, however, the ε phase was observed only at a greater depth (rather than at the 0.2 μm depth which would be sampled by the 2° GIXD measurements realized in the current study).

The intergranular acicular phase observed in figures 4 and 5 presents the same morphology as the α'' $Fe_{16}N_2$ phase identified for the same material in the previous study [3] and, although in a future stage of this research transmission electron microscopy and electron diffraction should unambiguously identify all phases present, it seems probable that the acicular phase can be considered to be the distorted body centred cubic α''. It is interesting to note that, although, as may be seen from figures 4 and 5, the α'' is predominantly observed at intragranular sites up to a depth of around 20 μm, some grain boundary precipitation of this phase is occasionally observed (lower right-hand side in figure 5(b)).

In the region shown in figure 5(b), close to a pearlite colony, the depth at which α'' formed was apparently restricted to around 10 μm (we assume that this is because the nitrogen diffusing into the steel during the plasma treatment interacted preferentially with the pearlitic cementite rather than undergoing further intragranular diffusion in the ferrite). Where, however, a grain boundary was present, even at the side of the pearlite colony most distant from the sample surface, α'' was observed to have precipitated at a greater depth, up to around 25 μm. Some indication of an enhancement of grain boundary diffusion of nitrogen during pulsed plasma nitriding is therefore evident, even in this low-temperature process (<500 °C).

Figure 6 shows more detail of the very diffuse interface where the surface nitride layer encountered and interacted with the pearlitic cementite. It is generally accepted [10] that, during the nitriding of steel, carbon from the hexagonal close packed Fe_3C is probably incorporated into the ε nitride $Fe_{2-3}N$ and such an ill-defined interface would indeed be typical of such a case and would result in the formation of carbonitrides of the type $Fe_{2-3}(C, N)$.

Microstructural modifications provoked by the pulsed-plasma-nitriding treatment are effectively limited to a depth of around 20 μm, as can be seen from figure 8. The hardening effect produced by nitrogen in solid solution in the ferrite extends to a total depth of over 500 μm (the major effect being observed up to around 250 μm). Though the pulsed-plasma technique is considered to be a relatively low-temperature method of nitriding, diffusion of a significant amount of nitrogen into the base steel evidently does occur.

It has been shown [3] that it is the surface nitride layer which is responsible for the very significant reduction in the kinetics of hydrogen permeation in plasma-nitrided steels, rather than the nitrogen-saturated ferrite in the sub-surface diffusion layer. In this study it was reduced from 2.97×10^{-10} to 7.1×10^{-11} mol H $m^{-1}\ s^{-1}$. The face centred cubic structure of the γ' phase in particular was found to exhibit a much higher solubility of hydrogen and much lower hydrogen diffusivity than did the body centred cubic ferrite [8]. The nitride layer, therefore, acts as an efficient barrier to diffusion of hydrogen. When the nitride layer is positioned on the hydrogen-detection side of the electrochemical cell the hydrogen permeability is further decreased to 3.9×10^{-13} mol H $m^{-1}\ s^{-1}$. This may be

explained by the fact that with this experimental orientation, the rate-controlling factor is the low hydrogen diffusivity of the nitride layer [8]. The nitride layer was also determined to be a barrier to hydrogen permeation in experiments on AISI 4140 steels, by observing its dependence on the layer's thickness [11].

The influence of other causes on the reduction in hydrogen permeation can be neglected. One of them is the possible presence of an oxide layer followed by an oxide–nitride interface. The probability of deposition of an iron oxide layer from the iron sputtered at the surface in combination with the oxygen (existing at a low percentage content in the plasma) can be considered very low. An estimation can be obtained if the voltage applied to the sample is already known: the energy distributions both of ionic and of neutral plasma species incident on the surface of the cathode can be estimated through the L/λ ratio (where L is the cathode sheath's thickness and λ is the mean free path for charge-exchange collisions). In our experiments, in which the applied voltage was 430 V, the L/λ ratio is in the range 10–15. This means that less than about 0.001% of the ions have their maximum energy associated with the applied voltage (430 eV) and the energy mean value is about 40 eV [12]. These low-energy ions that reached the surface did not provoke any significant sputtering effect on the surface. Therefore we cannot expect any significant amount of emission from free iron species from the surface. The formation of iron oxide in the plasma and its re-deposition onto the surface is of insignificant consequence, moreover, taking into consideration that the surface temperature during the nitriding process was relatively low.

5. Conclusions

The 6 h pulsed-plasma-nitriding treatment produced a 2 μm thick surface nitride layer containing both γ' (Fe_4N) and ε ($Fe_{2-3}N$) nitrides, as well as precipitation of α'' ($Fe_{16}N_2$) to a depth of 25 μm. Hardening due to nitrogen in solid solution in the ferrite extended to around 550 μm, though this effect was more pronounced in the first 250 μm below the nitrided surface.

The plasma-nitriding treatment resulted in a significant reduction in hydrogen permeability, from 2.97×10^{-10} mol H m^{-1} s^{-1} (for the untreated steel) to 7.1×10^{-11} mol H m^{-1} s^{-1} for electrolytic charging of hydrogen via the nitrided surface. When the sample was oriented with the nitrided surface as the hydrogen-exit face, the permeability was reduced even further, to 3.9×10^{-13} mol H m^{-1} s^{-1}.

Acknowledgments

The authors acknowledge the financial support of this research by the CNPq/CONICET (project 910192/95-2), Fundaciones Antorchas-Vitae (project B-11487/6B002), IAEA (research contract 302-F1-ARG-9384), CNPq grants 523298/96-0 and 62.0114/92.4-PADCT, CAPES, FINEP/PRONEX project 4.1.96.0909-00 and the collaboration of AGA SA. The laboratory support of Bianca P Trotta is also acknowledged.

References

[1] Michel H, Czerwiec T, Gantois M, Ablitzer D and Ricard A 1995 Progress in the analysis of the mechanisms of ion nitriding *Surf. Coating Technol.* **72** 103–11

[2] Zampronio M A, Cabo A, Bott A H and Miranda P E V 1994 Surface engineering to extend service life: new uses for traditional steels *Proc. IEV94 Int. Congress, 29th June–1st July, Buenos Aires* (Buenos Aires: Comision Nacional de Energia Atomica) pp 253–6

[3] Zampronio M A 1995 Revestimentos superficiais em aço para limitar a contaminação por Hidrogênio *DSc Thesis* COPPE/UFRJ, Rio de Janeiro

[4] Chicot D, Bartier O, Zampronio M A, Miranda P E V and Lesage J 1998 Diffusion et solubilite de l'hydrogene dans an acier faiblement allie nitrure ioniquement *Revue de Metallurgie* May 659–68

[5] Zampronio M A, Bartier O, Chicot D, Lesage J and Miranda P E V 1997 Efeitos do hidrogênio nas propriedades mecânicas do Aço API 5L X65 nitretado ionicamente por plasma *Matéria* **2** no 1 http://www.coppe.ufrj.br/~notimat/materia/Vol2N1/artigo8/artigo.htm.

[6] Brühl S P, Russell M W, Gómez B J, Grigioni G M, Feugeas J N and Ricard A 1997 Study by emission spectroscopy of the N_2 active species in pulsed dc discharges *J. Phys. D: Appl. Phys.* **30** 2917–22

[7] Jagielski J, Fayeulle S, Marest G and Moncoffre N 1995 Correlation between phase transformation and stress evolution in nitrogen-implanted iron *Mater. Sci. Eng.* A **196** 213–17

[8] Zampronio M A, Bartier O, Chicot D, Lesage J and Miranda P E V 1997 Hydrogen diffusion in plasma ion nitrided steel *Defect Diffusion Forum* **143–147** 939–44

[9] Miranda P E V and Fassini F D 1993 New methodology for the determination of hydrogen permeation in layered materials *J. Mater. Sci.* **28** 5148–54

[10] Jack D H and Jack K H 1973 Carbides and nitrides in steel *Mater. Sci. Eng.* **11** 1–27

[11] Bruzzoni P, Brühl S, Gómez B J A, Nosei L, Ortiz M and Feugeas J 1998 Hydrogen permeation modification of 4140 steel by ion nitriding with pulsed plasmas *Surf. Coating Technol.* to be published

[12] Leyland A, Fancey K S and Matthews A 1991 Plasma nitriding in low pressure triode discharge to provide improvements in adhesion and load support for wear resistant coatings *Surf. Eng.* **7** 207–15

Reprinted from

The Institute of Materials
1 Carlton House Terrace London SW1Y 5DB UK

WEAR BEHAVIOUR OF STEEL AND TITANIUM TREATED BY PULSED ION IMPLANTATION

J. Feugeas, G. Grigioni, G. Sánchez, and A. Rodriguez da Costa

Ion beams generated by plasma guns operated in detonation mode follow the energy spectral law $dN/dE \approx E^{-3.5}$ (number of ions N with energy E), with E in the range 20–500 keV, and a time duration Δt of 200–400 ns. These pulsed ion beams were used to implant nitrogen ions into steel and pure Ti. The results show a reduction in the wear rate of stainless steel by a factor of 10, and of high speed steel by a factor of 2, and also a reduction in friction coefficient. In addition, in autotempering steel and Ti, an increase in Vickers microhardness by a factor of between 2 and 3 was measured. The XPS and X-ray diffraction measurements also show high nitrogen concentration in the surface layers, with the nitriding producing the desired stoichiometry for tribological purposes. A study of the temperature evolution of the substrate owing to the pulsed nature of the beams (heating rate around 15 K ns^{-1}, temperature gradients of around 1500 K μm^{-1}, and peak temperatures near the melting point) shows that it plays an important role in the surface modification process.

Dr Feugeas, Dr Grigioni, and Dr Sánchez are at IFIR (CONICET–UNR), Bv. 27 de Febrero 210 Bis, 2000 Rosario, Argentina and Dr Rodriguez da Costa is at the Escola de Minas, Universidade Federal de Ouro Preto, Ouro Preto, MG, Brazil. *Manuscript received 14 April 1997.*

INTRODUCTION

Ion implantation is a well known technique for the surface treatment of metals for tribological property improvement, among other applications.[1] A large variety of ion species, energies, and fluences are used depending on the substrate nature and the final surface properties desired.[2,3]

In this work, some results are described for steel and pure Ti nitrogen implanted by pulsed ion beams, accelerated in focused electric discharges in a coaxial electrode system (plasma gun).[4] These beams present several differences with respect to standard low current and continuous ion beams, principally as a result of the short duration of the pulses, which provokes strong thermal effects in the surface layers in addition to the usual ion implantation process.

Also presented are results on the characterisation of the process that allow, to some extent, the explanation of the physics in this pulsed ion implantation process.

EXPERIMENTAL

Accelerator

Ion beams generated by plasma guns operated in detonation mode are accelerated during the collapse of the current sheath, which occurs as a dense plasma column (about 1 mm diameter and 6 mm length) or dense plasma focus (DPF). The energy stored in a capacitor bank is discharged into the coaxial electrode system (*see* Fig. 1), which is closed at one end by a coaxial insulator (pyrex pipe) and open at the other. The interelectrodic space is filled with a gas (of the type of ions to be accelerated) at a pressure ranging between 100 and 1000 mtorr (depending on the nature of the gas). For an optimised design (geometry, electrical parameters, and gas filling conditions) the breakdown occurs on the insulator surface as a gliding plasma sheath.

The interaction of the current sheath with the magnetic field generated by the external current accelerates the current sheath to the open side of the gun. During the rundown, the current sheath sweeps the gas of the interelectrodic space, ionising it and incorporating it into the sheath. When the open end is reached, the sheath is deformed, collapsing in front of the centre electrode (anode), generating the plasma column or DPF. In an optimised design the collapse occurs when the maximum of the external current discharge takes place. This high current circulates through the dense plasma column (about 100 kA in the present system), being responsible for the Rayleigh–Taylor instability generation which drives the ion and electron beam acceleration.[5] On the other hand, the remains of the current sheath will move continuously out of the electrode system, reaching long distances downstream.[6]

For the present system, the ion beam characteristics can be summarised as follows: pulse time duration Δt between 200 and 400 ns; fluence f per pulse $\leqslant 10^{13}$ cm^{-2}; ion energy spectral law given by $dN/dE \approx E^{-3.5}$ (where N is the number of ions with energy E) with E ranging between 20 and 500 keV; and a beam emission of conic geometry with a solid angle of approximately 40°.

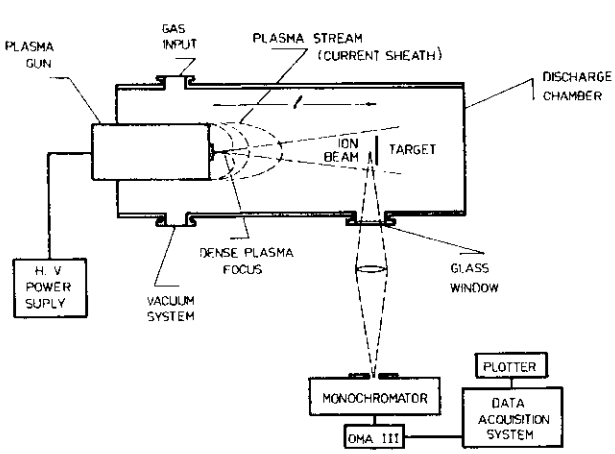

1 *Schematic diagram of experimental pulsed ion implantation setup*

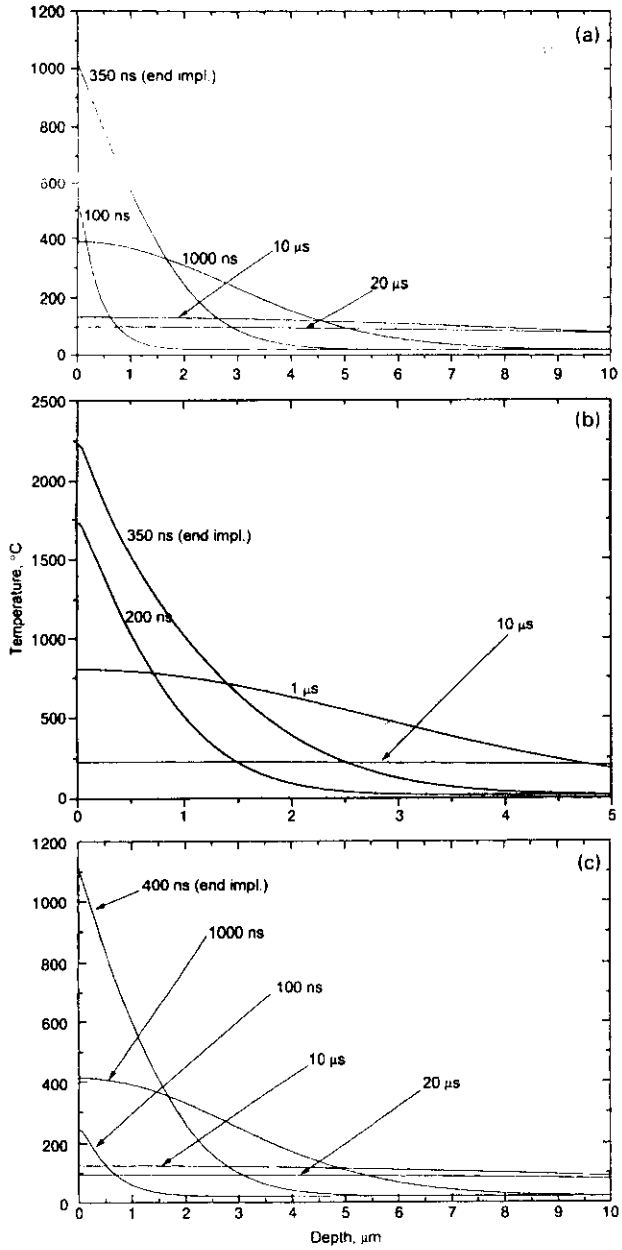

a stainless steel, $\Delta t = 350$ ns; *b* Ti, $\Delta t = 350$ ns; *c* Ti, $\Delta t = 350$ ns

2 *Temperature evolution profiles for surface layers during and after nitrogen pulsed ion implantation*

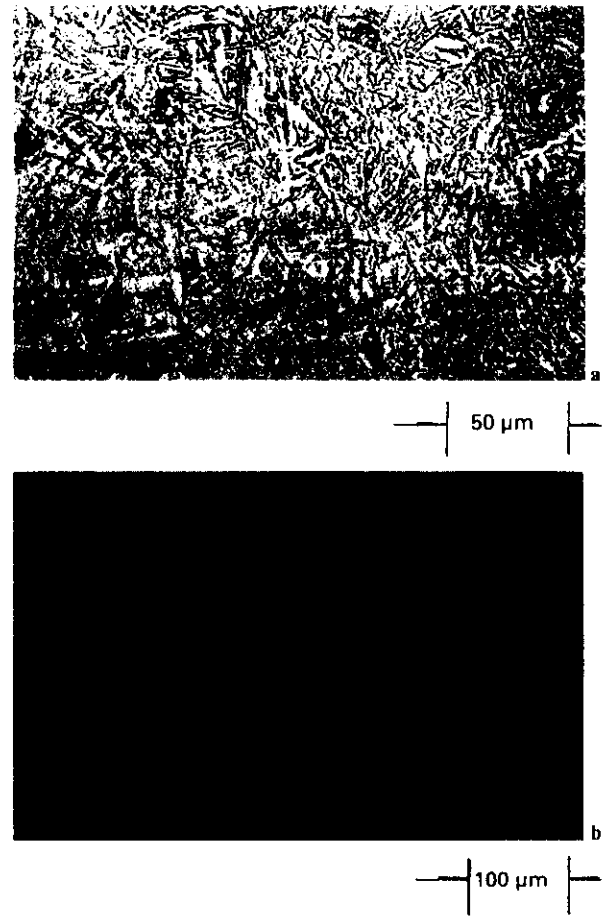

a unimplanted, showing martensitic structure (×320); *b* nitrogen ion implanted, $\Delta t = 280$ ns, showing surface melting (×130)

3 *Optical micrographs of surface of autotempering tool steel samples*

The targets to be implanted are located in front of the beam at some distance from the end of the anode, as shown in Fig. 1. A total implantation fluence F can be obtained by the accumulation of a predetermined number n of beam pulses with fluence f ($F = nf$).

Thermal process characterisation

Owing to the short duration of the beam pulses, a fast energy release takes place during ion beam interaction with solid surfaces. An evaluation of the heating process has been done previously, using finite difference calculations[7] because of the practical impossibility of measuring the thermal evolution in the implanted layers owing to the short duration of the process (400 ns) and the small region (1 μm) affected.

In Fig. 2 the thermal evolution of the surface during the interaction of a nitrogen ion beam with steel (Fig. 2*a*) and pure Ti (Fig. 2*b* and *c*) is plotted against target depth for various times. The pulse length is directly related to the velocity of energy deposition during ion implantation, and consequently to the heating velocities and peak temperature on the surface: the shorter the pulse length, the higher the thermal shock.

In the case of Ti, the results for two different pulse lengths Δt are presented. For $\Delta t = 350$ ns the Ti melting point is reached (Fig. 2*b*) whereas for $\Delta t =$ 400 ns the peak temperature is below the melting point (Fig. 2*c*). In addition to the high peak temperatures the calculations show the velocity of the heating process, with heating velocities of about 15 K ns^{-1} and associated temperature gradients of about 1500 K μm^{-1}.

Considering that the time lapse between ion beam pulses during a repetitive implantation process is around 1 s, and that the surface of the target returns to room temperature in several tens of microseconds (*see* Fig. 2), each new ion beam reaches the target surface when it is completely thermally relaxed. This heating process was verified experimentally both directly and indirectly. Direct verification was by surface observation of implanted samples, which showed in the case of the shorter ion beam pulses the damage to the surface of the target as a result of the material meltdown (*see* Fig. 3*b*). Indirect verification was provided by results including the induced

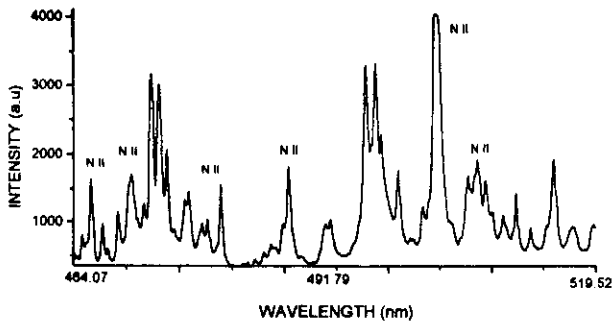

4 *Optimal emission spectrogram of nitrogen plasma at sample location*

residual stresses[8] and residual deformations[9] in steel, Al, and Cu, whose explanation can be found in the fast heating process associated with the beam interaction with the solid.

Plasma sheath ionisation

The remainder of the current sheath moves forward (*see* Fig. 1), reaches the target surface after the ion beam pulse, and lasts for more than 10 μs, far longer than the ion beam pulse duration. Using the technique of optical emission spectroscopy, the type and degree of ionisation were studied. An optical multichannel analyser (OMA III) was used for the measurements, focusing the plasma in the region of the target (*see* Fig. 1).

In Fig. 4 a spectrogram corresponding to an experiment with nitrogen is shown where the NII (nitrogen once ionised) emission lines are clearly visible. This shows that the plasma activity can play an important role in surface treatment with pulsed ion beams generated by plasma guns.

RESULTS

Samples of different materials were implanted with nitrogen ions using a range of pulse lengths Δt and total fluences F. The materials used were stainless steel AISI 304, high speed steel M2, pure Ti, and autotempering tool steel.

Stainless steel AISI 304

The results for AISI 304 stainless steel (0·08C–1·4Mn–0·6Si–0·04Mo–9·0Ni–18·6Cr–0·051Co–0·057P) show a strong improvement in the wear rate and a reduction in the friction force, for nitrogen ion implantation with a total fluence of $1{\cdot}3 \times 10^{17}$ cm^{-2} and a pulse duration of 280 ns.[10]

Wear and friction tests were performed by loading the implanted sample under constant force against a rotating wheel, with the surfaces in contact immersed in mineral oil. The wear scar depth was measured by controlling the displacement of the sample during the penetration of the rotating wheel into the sample, and the sliding distance by controlling the number of turns of the wheel. The friction force was measured by a load cell coupled to the sample, orientated tangentially to the wheel perimeter. The comparative results for implanted and unimplanted samples show a wear rate reduction of 90% in the former (Table 1), and a reduction in the friction force of between 50% (at the beginning of the test) and 30% (long term stabilised value).

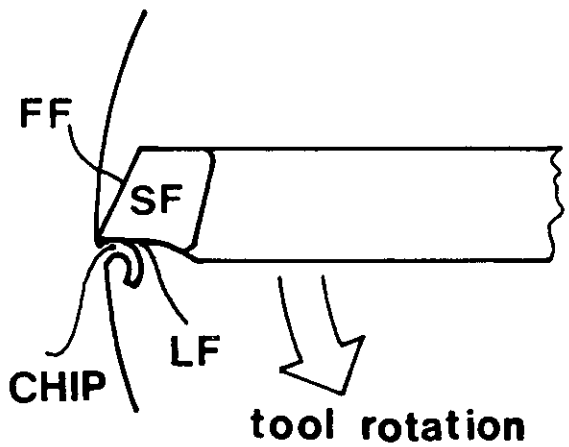

5 *Schematic front view of tool in working position for wear testing*

The nitrogen concentration profile (determined by XPS) of the implanted layer shows 12 at.-% at the surface decreasing to 6 at.-% at a depth of 10 nm, with this percentage being maintained to the maximum depth observed, i.e. 180 nm. X-ray diffractograms showed the formation of Fe_2N and the presence of α-Fe (ferritic phase) in the pre-existing γ-Fe (austenitic phase) of the AISI 304.

High speed steel M2

Wear tests on high speed steel type M2 (0·83C–0·3Si–5·0Mo–4·1Cr–0·3Mn–1·9V–6·1W) were conducted under special experimental conditions. Unimplanted and nitrogen implanted high speed steel cutting tools were wear tested using an industrial boring process for SAE 1045 parts.[11]

The process consists of machining the parts with a lathe by turning its surface into a semicylindrical concavity 35 mm in diameter. Machining is achieved by the successive work of four double ended cutting tools (*see* detail in Fig. 5) distributed along a cylindrical support, with a separation d of 30 mm and a rotation angle α of 45° between consecutive tools (Fig. 6). The machining process starts with tools T1 and T2, and the final radius of 35 mm is produced by tool T4. This last tool, T4, is the one responsible for surface finishing, or boring, and the one selected for wear test purposes. For machining, the cutting speed utilised was 6·15 m min^{-1}, with a cutting depth of 1·5–1·8 mm, in soluble oil lubricated conditions.

Wear was measured by controlling the shortening of tool T4, whose initial length (distance between tips) was L. Three measurements were made for each tool: before machining ($L1$); after the machining of

Table 1 Wear scar depths for unimplanted and implanted AISI 304 samples

	Wear scar depth, μm	
Sliding distance, m	Unimplanted	Implanted
100	16	0·69
200	24	1·38
300	29	2·07
400	34	2·76
500	39	3·40

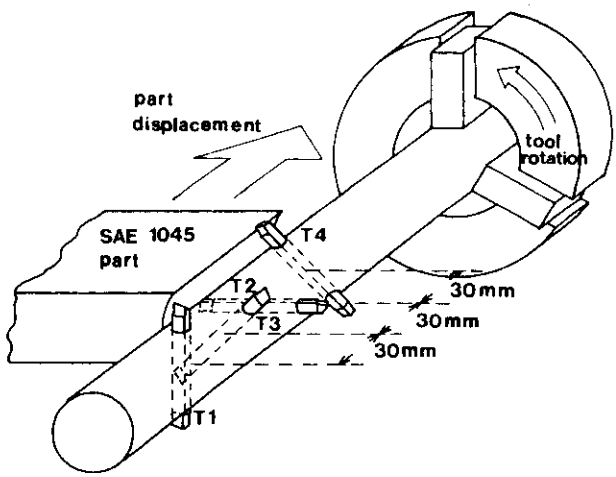

6 *General view of wear testing machining setup*

100 parts ($L2$); and after the machining of 200 parts ($L3$). The results for both implanted and unimplanted tools are given in Table 2.

The results show a systematic reduction of around 50% in the wear rate, for tools nitrogen implanted with a total fluence of $1{\cdot}65 \times 10^{17}$ cm^{-2} and pulse duration of 280 ns. X-ray diffraction analyses showed the formation of Fe_4N, Fe_3C, and WN on the affected layers, with the development of γ-Fe (austenitic) phase in addition to the pre-existing α-Fe (ferritic) one. However, Co_3W_3C, which was observed in unimplanted samples, was totally absent after implantation, being part of the source of W for the development of WN. The nitrogen concentration profile after implantation (XPS measurements) showed about 22 at.-% at the surface, with a reduction to 12 at.-% at 8 nm depth, staying constant to the deeper levels observed (50 nm).

Pure Ti

Pure Ti samples were nitrogen ion implanted with two different types of beam:[12] beam 1 had a pulse length of 350 ns, and beam 2 a length of 400 ns; with beam 1 the implantation was done with a total fluence of $2{\cdot}6 \times 10^{16}$ cm^{-2}, and with beam 2 the fluence was $4{\cdot}2 \times 10^{16}$ cm^{-2}.

The XPS study of the implanted layers showed the formation of TiN with a stoichiometry of $TiN_{0{\cdot}85}$ for beam 1 and $TiN_{0{\cdot}80}$ for beam 2. The nitrogen concentration profile showed, for samples implanted with beam 2, a constant value of 43 at.-% in the surface layer down to a depth of around 30 nm, and a gradual decrease towards deeper levels, reaching 31 at.-% at the deepest level measured (60 nm).

Table 2 Comparative results for unimplanted and implanted tool wear: $L1$ original tool length; $L2$, $L3$ tool lengths after machining of 100 and 200 parts respectively

Tool dimension, mm	Unimplanted	Implanted
$L1$	68·11	67·68
$L2$	67·85	67·57
$L3$	67·65	67·48
$L1 - L2$	0·26	0·11
$L1 - L3$	0·46	0·20

The Vickers microhardnesses of unimplanted and implanted samples were measured with a load of 5 g. In the case of pure Ti the hardness was 270 HV, whereas for samples implanted under both conditions the hardness was 655 HV.

Autotempering tool steel

Samples of autotempering tool steel (0·53C–0·50Mn–0·33Si–3·8Ni–1·65Cr–0·27Mo–0·03W–0·17Cu–0·01Al–0·01P) were nitrogen ion implanted with a total fluence of 8×10^{16} cm^{-2} using three different beam types: beams 1 and 2 with the Δt values used in the Ti implantation, and beam 3 with $\Delta t = 280$ ns.

Sample surfaces, before and after implantation, were observed and photographed (×320) using an optical microscope. Figure 3 shows images of the sample surfaces: Fig. 3*a* shows the surface of an unimplanted sample, and Fig. 3*b* the surface of a sample after implantation using beam 3. No changes in martensite content were observed for implantation using beam 1 or beam 2. However, in the case of implantation with beam 3 (as can be seen in Fig. 3*b*) a surface melted layer was observed.

Microhardness measured using a 25 g load also showed no change from the preimplantation level of about 270 HV after implantation with beams 1 and 2. But an important increase was observed (up to 550 HV) in the case of implantation with beam 3. The microhardness measurements are displayed in Table 3.

DISCUSSION

From the results detailed above it is possible to determine the influence of the thermal effect in the process of ion implantation with pulsed ion beams generated with plasma focus. The following points can be made.

The nitrogen concentration uniformity in depth observed in the implanted materials can not be attributed only to a single ion implantation process. Instead, the results can be explained by reference to the process of strong heating, fast temperature increases, and sharp temperature gradients (*see* Fig. 2). This thermal process can assist the nitrogen redistribution through its diffusion to deeper levels, homogenising the concentration.

In the case of Ti, the high values of nitrogen concentration observed are in contrast with the low fluences used in the implantation processes. Total fluences of $2{\cdot}6 \times 10^{16}$ and $4{\cdot}2 \times 10^{16}$ cm^{-2} can not develop layers with the nitrogen concentration measured. In this case, and taking into account the getter properties of Ti, the combined effect of the strong thermal shock induced by the ion beam pulses, plus the highly activated nitrogen plasma which interacts with the target immediately after the ion beam

Table 3 Microhardnesses of unimplanted and implanted autotempering tool steel

Implantation condition	Microhardness, HV
Unimplanted	270 ± 10
Beam 1	260 ± 10
Beam 2	270 ± 20
Beam 3	550 ± 70

incidence, may be responsible for the extra nitrogen incorporation into the surface. Every incident ion beam pulse heats the surface, improving the diffusion of nitrogen already present in the surface layer towards the deeper layers, and thereby allowing the absorption of nitrogen from the plasma which reaches the surface. This process is repeated for each ion beam pulse, incorporating (ion beam plus plasma) nitrogen into the surface and pumping it towards deeper levels. Looking at the plots of temperature profiles in Fig. 2*b* and *c*, it is possible to see that temperatures as high as 400°C are developed 2 μm below the surface within the first microsecond of the single beam incidence process. During this time, the ion beam pulse falls on the surface (for 350 ns in Fig. 2*a* or 400 ns in Fig. 2*c*), heating the surface layers directly and indirectly, the deeper ones by thermal conduction; this is followed by a cooling process, also a result of thermal conduction to the sample bulk.

The apparent contradiction found for pure Ti nitrogen implantation, in which the higher TiN stoichiometry ($TiN_{0.85}$) is developed for the lower total fluence (2.6×10^{16} cm^{-2}) used whereas $TiN_{0.80}$ was found for a higher total fluence of 4.2×10^{16} cm^{-2} (both stoichiometries acceptable for tribological purposes[13]), can be explained by the fact that for this case the single beam pulse length Δt was short enough (350 ns) to initiate surface melting. This can be seen in Fig. 2*b* where the temperature profile evolution for Ti implanted with such a beam is presented showing the melting of the surface in approximately 160 ns.

The improvements in the microhardness of the autotempering steel tool show that for equal total fluences (8×10^{16} cm^{-2}), the microhardness is increased with respect to the unimplanted samples only for the ion beam of shorter pulse duration. Taking into account the fact that a shorter pulse length means higher temperatures, the resulting microhardness improvement can be attributed to the induced thermal effect during pulsed ion implantation. On the other hand, this fact is corroborated by microscopic surface observation (Fig. 3), by which a melted layer was observed only in the case of implantation with the shorter ion beam pulse length.

CONCLUSIONS

Significant improvements in the tribological properties of steel and Ti were observed after nitrogen ion implantation with pulsed beams generated with plasma guns. Nevertheless, the explanation of this structural modification can not be found by referring to the ion implantation process alone; the thermal effect that the fast energy release, owing to the short duration of the beam pulse, induced in the first 2–3 μm under the surface must also be considered. The nitrogen which is implanted with every ion beam, is redistributed with the following ion beam pulse as a result of the high temperatures and strong temperature gradients, leading to more uniform and deeper nitrogen concentration layers, by a thermally assisted diffusion process. In particular, the remaining plasma which follows the ion beam acceleration can contribute to an increase in nitrogen surface absorption. This process is especially important in materials such as Ti in which the getter effect is very strong.

ACKNOWLEDGEMENTS

The authors are grateful to A. Muñoz for his collaboration in the experimental work. Work was performed under CONICET grant PID–BID 222 and IAEA research contract RC/6477/RB.

REFERENCES

1. I. J. R. BAUMVOL: in 'Ion implantation equipment and technology'; 1984, New York, NY, Academic Press.
2. N. J. MIKKELSEN and C. A. STRAEDE: *Surf. Coat. Technol.*, 1992, **51**, 152.
3. J. PIEKOSZEWSKI, Z. WERNER, J. LAGNER, L. JAKUBOWSKI, C. POCHRYBNIAK, and A. HARASIEWICZ: *Nucl. Instrum. Methods*, 1983, **209/210**, 477.
4. W. BOSTICK, V. NARDI, and W. PRIOR: *Ann. New York Acad. Sci.*, 1975, **251**, 2.
5. V. NARDI, W. BOSTICK, J. FEUGEAS, and W. PRIOR: *Phys. Rev. A*, 1980, **22**, 2211.
6. V. NARDI, W. BOSTICK, J. FEUGEAS, W. PRIOR, and C. CORTESSE: *Nucl. Fus.*, 1979, Suppl. 2, 143–157.
7. G. SÁNCHEZ and J. FEUGEAS: *J. Phys. D, Appl. Phys.*, 1997, **30**, 927–936.
8. A. POCHETTINO, J. FEUGEAS, M. ORTIZ, and G. SÁNCHEZ: *Proc. Journ. Contrainte Resid. Nouv. Technol.*, 1990, 7.
9. G. KAUFMANN, S. BRÜHL, J. FEUGEAS, G. SÁNCHEZ, M. STORTI, and A. CARDONA: *J. Phys. D, Appl. Phys.*, 1995, **28**, 1655–1660.
10. J. FEUGEAS, E. LLONCH, C. O. DE GONZÁLEZ, and G. GALAMBOS: *J. Appl. Phys.*, 1988, **64**, 2648.
11. J. FEUGEAS, C. O. DE GONZÁLEZ, M. F. PEYRONEL, and G. SÁNCHEZ: *Braz. J. Vac. Appl.*, 1990, **9**, 118.
12. J. FEUGEAS, G. SÁNCHEZ, G. GRIGIONI, and C. O. DE GONZÁLEZ: Proc. MRS Symp. on 'Materials modification by energetic atoms and ions', San Francisco, CA, 1992, 389.
13. D. DAVID, E. A. GARCIA, G. BERANGER, J. P. BARS, E. ETCHESSAHAR, and J. DEBUIGNE: Proc. 4th Int. Conf. on Titanium, Kyoto, Japan, 1980, 536.

RESIDUAL STRESSES IN ION IMPLANTED STEELS

A.A.POCHETTINO[1-2], J. FEUGEAS[3], M.ORTIZ[1] AND G. SANCHEZ[3]

1. Dpto. Materiales, Gcia. Desarrollo, CNEA,
Av. Libertador 8250, 1429 Buenos Aires, Argentina

2. LM3, UA CNRS 1219, ENSAM,
151 Bd. de l'Hôpital, 75013 Paris, France.

3. IFIR (Conicet-UNR), 27 de Febrero 210 Bis,
2000 Rosario, Argentina

ABSTRACT

Ion implantation introduces microstructural changes which can produce residual stress states in treated materials. First results concerning Nitrogen ions implantation in AISI 1075 and M2 steels are presented in this work. Implantation experiments were performed by using an ion pulsed beam implanter with a continuous energy spectrum (20 Kev< E <550 Kev) and residual stress measurements were carried out by using X-Ray diffraction techniques. Important changes in the surface residual stress states were determined in the implanted steels. Results are discussed accounting microstructural changes affecting the surface layers and the radiation damage effects.

INTRODUCTION

Ion implantation is a physical process where atoms of a given element are introduced into a solid structure only by means of their kinetic energy. This method introduces modifications in physical and chemical properties of surface layers and it is used in numerous applications going from microelectronics to metallurgy [1]. In this domain, nitriding using Nitrogen ions implantation in steels has shown its utility for the improvement of the tribological properties and the fatigue behaviour of those materials. Nevertheless, it is important to remark that the properties changes introduced in steels by ion implantation are not only a function of the type of implanted steel but also a function of the experimental conditions of implantation: geometry, energy, flux and dose of the ion beam.

Ed. by H. Fujiwara, T. Abe & K. Tanaka
Elsevier Applied Science, 1992

Ion accelerators used during ion implantations are generally low flux, single-energetic beams with a constant current associated (40Kev<E<100Kev). Integrated doses are obtained by implantation during important periods of time. The results presented in this work were obtained by a non-conventional technique of ion implantation, which utilises an ion pulsed beam implanter (BD-1 developped at IFIR-UNR). The main characteristics of the ion beam can be summarized as follows [2]:

* Pulsed beam with pulse time duration of 200ns<t<700ns.
* The ion beam presents a continuous energy spectrum: (20Kev<E<550 Kev, $dN/dE \approx E^{-3.4}$).
* Fluence associated to each shot $\approx 5.10^{15}$ ions/cm^2.
* Beam emission geometry: cone with solid angle $\theta \approx 40°$.
* Higher fluences can be obtained by the accumulation of a prefixed number of shots.

The interpretation of the microstructural changes introduced by ions implantation requires the combination of two aspects of the radiation damage phenomena: defects production by the ions-target elastic scattering and a high speed elevation of the sample temperature during a short period of time produced by the inelastic scattering of ions.

Microstructural modifications introduced into the implanted region can introduce non-reversible deformations in the material, and, consequently, generate Residual Stress (R.S.) states.In this paper, results of R.S. introduced in AISI 1075 (0.7-0.8 % C, 0.4-0.7 % Mg, ≤0.04% P, ≤0.05 S) and in M2 (0.06-0.04 % C, 3.75-4.5 % Cr, 4.5-5.5 % Mo, 5.5-6.75 %W, 1.75-2.20 % Va, 0.20-0.45 % Si, 0.15-0.4% Mn, ≤0.03 P, ≤0.03 S) steels by Nitrogen ions implantation are presented and discussed.

EXPERIMENTAL RESULTS

R.S. states were determined using X-Ray diffraction techniques; $2\theta_{hkl}$ vs. $\sin^2\psi$ curves were obtained using the {211} peaks of the Cr Kα radiation (λ=0.22909 nm). Experiments show that either in non-implanted or in Nitrogen implanted steel, the determined R.S. states can be considered as those corresponding to an homogeneous and isotropic material, Figs. 1 (a) and (b) [3]. In this case, the X-ray elastic constants used for the evaluation of the R.S. states correspond to those given by Noyan [4]. These stress states can be generally associated to biaxial R.S. states. In some cases, especially for high fluences of implanted Nitrogen, shear components were determined, their values are approximately 10-15% of the diagonal components of the stress tensor.

Table 1 shows the R.S. values obtained along the rolling (ø=0°) and the transversal (ø=90°) directions for the AISI

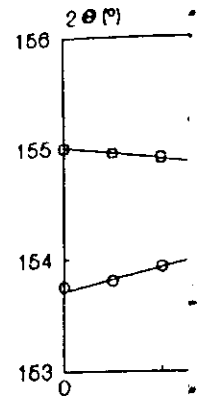

(a) Ro

Figure 1.
□ no

Surface
imp

Samp
non-imp
1.5 10^{15}
1.5 10^{17}

Surface

Samp
non-imp
1.5 10^{16}
2.5 10^{16}

1075 ferrit
stresses do
implanted N
initial R.S
with the in
an expansio
Table 2.

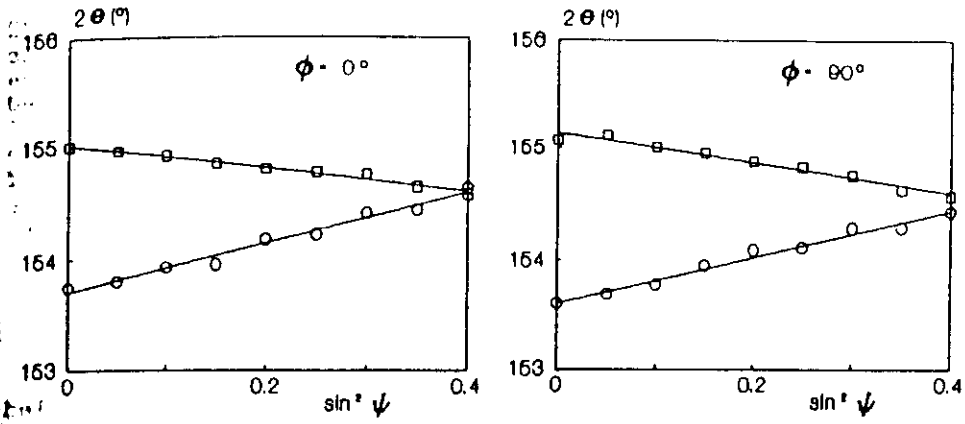

(a) Rolling Direction (b) Transversal Direction

Figure 1. $2\theta_{(211)}$ vs $\sin^2\psi$ curves for the AISI 1075 steel: □ non implanted, o implanted 1.5 10^{17} Ions/cm².

TABLE 1
Surface residual stress evolution with Nitrogen ions implantation in the AISI 1075 ferritic steel.

Sample	Rolling Dir.	Transv. Dir.
non-implanted	232±40 MPa	245±15 MPa
1.5 10^{16} Ions.cm^{-2}	-286±24 MPa	-----
1.5 10^{17} Ions.cm^{-2}	-261±50 MPa	-280±37 MPa

TABLE 2
Surface Residual stresses in the M2 Steel implanted with Nitrogen Ions.

Sample	Rolling Dir.	Transv. Dir.
non-implanted	-880±67 MPa	-768±35 MPa
1.5 10^{16} Ions.cm^{-2}	-304±25 MPa	-358±52 MPa
2.5 10^{16} Ions.cm^{-2}	342±51 Mpa	454±87 MPa

1075 ferritic steel. It can be observed that the measured stresses do not present a linear dependence with the dose of implanted Nitrogen ions. In the case of the M2 steel, the initial R.S. state corresponds to compressive stresses and, with the increment of the Nitrogen ions dosis, it changes to an expansion stress state. These results are presented in Table 2.

Figure 2 shows the R.S. evolution with depth in the M2 steel for an implantation dose of 3.5 10^{16} Ions cm^{-2}. It is interesting to remark that, accounting the penetration of the Cr-Kα X-Ray in steels (≈ 10μm), the stress values associated to each point of the curve correspond to the integration of their gradient in depth for a layer of about 10 μm. It can be observed from the curves of Figs. 2(a) and (b) that a layer of about ≈ 20μm is affected by the Nitrogen implantation. The width changes of the diffraction peaks observed between non-implanted and implanted samples are not significant.

DISCUSSION

The analysis of the experimental results needs a detailed study of the ion-matter interaction mechanisms and the microstructural changes introduced by this interaction. Two basic effects should be considered [5]:

- Energy losses by inelastic electronic scattering,
- Elastic collisions with atomic displacements production.

Energy losses by inelastic scattering are a consequence of the electromagnetic interactions between the incident Nitrogen ions and the electronic core of the sample atoms. These interactions can produce thermal effects introducing very localized and very shorts (≈10^{-9} s) "thermal peaks". Sometimes local temperatures could surmount the melting point. It is evident that thermal effects could also induce localized phase transformations nitrides formation.

Elastic collisions produce primary atomic displacements of sample atoms, which can also produce cascade collision processes. Interstitials and vacancies generated during the cascade process can contribute to:

* The acceleration of the diffusion processes,
* The formation of atomic segregations (interstitials or vacancies) and new phases (as nitrides).

Related to nitrures formation, Fe_4Ni was detected in a layer of 0.2 μm of depth by Auger microanalysis in the case of an implanted AISI 304 stainless steel [6].

Microstructural changes introduced by ion implantation are the combination of the stated effects. Considering the ion beam spectral law ($dN/dE \approx E^{-3.4}$ with 20Kev<E<550Kev) it can be easily demonstrated that only 19% and 2% of the ions associated to each shot will have energies verifying E≥40Kev and E≥100Kev respectively. Then, it is evident that thermal effects will be very important near the surface and that displacement processes will contribute to microstructural changes in depth (lower than 15-20 μm). Considering the R.S. distribution in depth, Figs. 2 (a) and (b), it is also evident that thermal effects could be related to the change of the

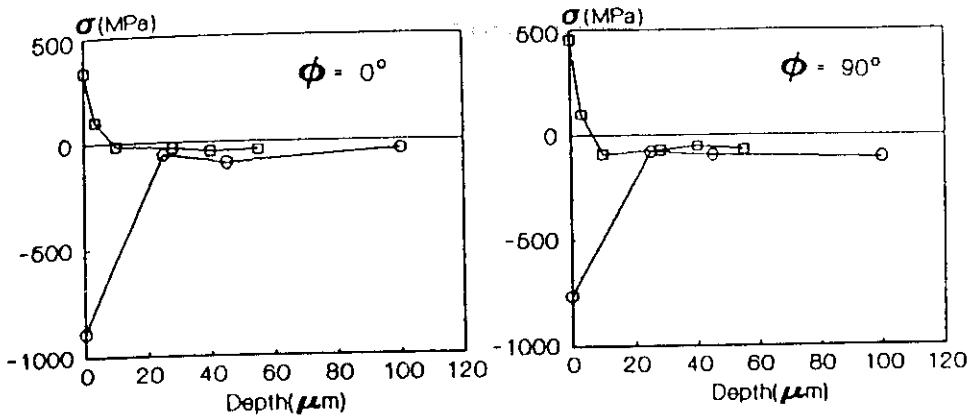

(a) Rolling Direction (b) Transversal Direction

Figure 2. Residual Stress evolution with depth in M2 steel. Nitrogen implantation dose: 3.5 10^{16} Ions cm^{-2}.

R.S. states before and after implantation. For example, in the case of compressive residual stresses, plastic deformation is facilitated near the surface of the solid when temperature increases. As this thin layer is in compression and the remainder material is not deformed (for depth greater than 20 μm residual stresses are negligeable), a tensile residual stress state can be generated in the implanted region. A similar reasoning can be applied in the case of initial tensile residual stresses. This is a very simplified reasoning but it constitues a first step to interpretate the R.S. changes observed.

Another factor to be accounted for is the possibility of a martensitic transformation during the cooling process of the sample which undergoes thermal effects [7]. This effect could introduce an additional R.S. state in the surface layer. In our experiments, its role either is not significant in front of that introduced by thermal effects or it could be overlapped by other metallurgical effects. The same reasoning can be applied to another source of R.S. states: nitrides formation induced by the implanted Nitrogen. In this case, there are some X-Ray evidences of nitrates formation in our samples, which might introduce compressive residual stress. A more detailed study on the influence of induced metallurgical phenomena is at present being carried out.

CONCLUSIONS

The first results about the generation of R.S. by Nitrogen ions implanted in steels using the BD-1 accelerator indicate that stresses can be associated to tensile or compressive states. The interpretation of the experimental results needs the analysis of many simultaneous processes produced by the ions in the steels: defects production by elastic scattering, thermal peaks produced by inelastic scattering and the consequent possibility of martensitic transformations induced during the cooling process, the radiation enhanced atomic diffusion and the possibility of nitride nucleation. The interpretation of our experimental results indicates that thermal effects produced by inelastic scattering could be responsible of the reported changes in residual stress states.

ACKNOWLEDGEMENT

This work was partially supported by the Programa Multinacional de Investigaciones y Desarrollo de Materiales (PMIDM, OEA-CNEA). The authors are thankful to Mr. P. Gargano for his cooperation and help.

REFERENCES

1. Hirvonen, J.K., Ion beam processing for industrial applications. Mat. Science. and Eng., 1989, A116, 167-175.

2. Ortiz, M., Sanchez G., Saulino, D., Maragno, L., Feugeas, J. and Pochettino, A., Residual stresses in Nitrogen ion implanted AISI 1075 Ferritic Steel, in Proc.IAEA Meeting on Residual Stresses in Structural Materials and components of Nuclear Power Plants, ed. by IAEA-CNEA, 1989, pp 125- 129.

3. Lebrun, J.L. and Pochettino, A., Determination de champs de déformations et contraintes en utilisant la diffraction. ENSAM, Paris (France), 1991.

4. Noyan, I.C., Determination of the elastic constants of inhomogeneous materials with X-Ray Diffraction. Mat.. Science and Eng., 1985, 75, 95-103.

5. Thompson, M. W., Defects and radiation damage in metals, University Press, Cambrigde, 1969.

6. Feugeas, J., Gonzalez, C.O. de, Llonch, E. and Galamboe,G, Nitrogen implantation of AISI 304 stainless steel with a coaxial plasma gun. J. of Appl. Phys.,1988, 64, 2648-2651.

7. Beck, G. and Ericsson, T., Prediction of residual stresses due to heat treatment, in Proc. 1st. Int. Conference in Residual Stress, ed. E. Macherauch and V. Hauk, DGM-Verlag, 1987, pp 27-40.

J. Phys. D: Appl. Phys. 30 (1997) 2026–2032. Printed in the UK PII: S0022-3727(97)80259-8

Optical emission spectroscopy of electrical focii discharges

J Feugeas and G Grigioni

Instituto de Física Rosario (CONICET, UNR), Boulevard 27 de Febrero 210 bis, 2000 Rosario, Argentina

Received 11 December 1996

Abstract. The optical emission from a dense magnetized plasma column (the Z pinch) was studied in experiments with a 1 kJ plasma focus using an optical multichannel analyser (OMA III). The plasma column (about 10 mm length and about 1 mm diameter) generated at the end of the co-axial discharge had a density of about 10^{19} cm^{-3}, a duration of about 200 ns and a maximum circulating current of about 170 kA. All the most intense lines from the carrier gases (neutral atoms and ions) were found in the spectra in the optical range 340–700 nm, showing that the line intensity was independent of the pinch intensity. Also, an intense emission from other elements such as copper (belonging to the brass electrodes) and silicon (from the glass insulator) was observed with a strong dependence of their line emission intensities on the pinch intensity. By partially covering the electrode surfaces with aluminium sheets, and studying variation of the aluminium and copper line emission intensities with the pinch intensity, it was shown that the source of contamination could be attributed in part to the power energy density deposition of the current sheath during the breakdown and run down stages of the discharge, before the formation of the dense plasma column. This more energetic electrode (and glass insulator) erosion can be associated with a thinner current sheath, a condition that is also conducive to more efficient pinch formation. The possibility of covering the last centimetre of the electrode surfaces with materials with higher evaporation points offers an opportunity to reduce the contamination effect when the plasma focus is used as a surface-treatment apparatus.

1. Introduction

Among a large variety of experiments on high-density magnetized plasmas, the plasma focus is relevant because of the extraordinary efficiency in the development of several energetic processes. As an example, it is possible to mention that 10^9 neutrons (from nuclear fusion reactions) can be obtained in experiments (using deuterium as filling gas) with 4 kJ of energy stored in a capacitor bank [1]. Also, relativistic electron beams are efficiently accelerated in experiments of similar characteristics, with a simultaneous and intense emission of hard x-rays [2]. The generated ion beams have a wide energy spectrum with an energy tail that exceeds 10 MeV, with fluences in the range 10^{14}–10^{15} cm^{-2} emitted in pulses of about 300 ns duration [3]. This high-power energy released by the ion beams has been used in several applications for surface modification of solids, providing significant improvements in the tribological properties of steels and pure titanium when nitrogen and argon were used in the experiments [4].

The whole physical process of the experiment, beginning with the breakdown, followed by the evolution of the discharge and ending with the formation of a high-density and strongly magnetized plasma column, is accompanied by the emission of strong electromagnetic radiation, which goes from very short wavelengths (hard x-rays) to radiowaves. In every stage, the interaction of the discharge with the solid surface of the electrodes and insulator produces its erosion, contributing to the contamination of the plasma with heavy particles. This contamination was observed, for example, on the upper surface layers of materials treated with the ion beams and constitutes a problem when high purity is required.

In this paper the emission in the visible range was studied by optical spectroscopy using an optical multichannel analyser (OMA III), for the purpose of identifying the atomic and ionic species in the plasma and to study their intensities. In particular, the line emission of the contaminating species can help one to investigate the role and importance of each stage of the discharge. Overall, taking into account that the energetic plasma environment generated in plasma focus experiments responds to physical conditions of characteristics similar to those in other experiments (Z pinches in particular), the results are of general interest.

0022-3727/97/142026+07$19.50

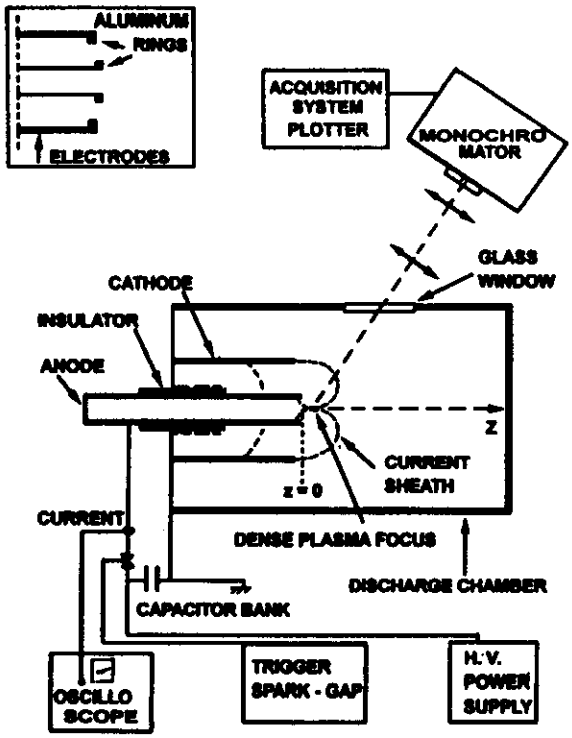

Figure 1. A schematic diagram of the plasma focus and the optical set-up for the spectroscopic examination of the emission from the plasma.

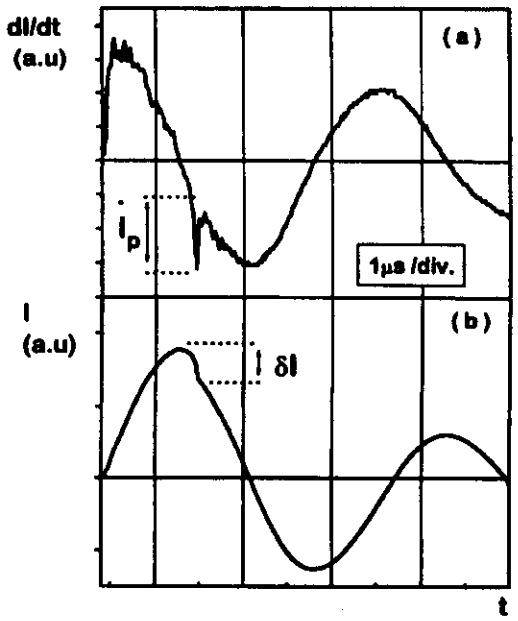

Figure 2. (a) A typical recorded trace of the temporal derivative of the external current discharge and (b) the corresponding current trace obtained by numerical integration.

2. The experimental set-up

2.1. The plasma focus device

The plasma focus is essentially a Z pinch experiment, in which the plasma column is developed at the end of a fast discharge in a plasma gun. A detailed description of the plasma focus can be found in many publications since the early works of Mather [3, 5].

Basically, the plasma focus consists of a co-axial electrode system open at one end and closed, but separated by a co-axial insulator, at the other (see figure 1). The electrodes are connected to a capacitor bank by a low-impedance transmission line, through a fast spark-gap switch. The electrodes are located within a discharge chamber, which is filled with a pure gas at a controlled pressure (between 0.1 and several Torr, depending on the type of experiment). For cleaning purposes, the chamber is evacuated to 10^{-5} Torr prior to being filled with the working gas.

When the spark-gap switch is closed, the electrical energy stored in the capacitor bank is discharged into the electrodes producing the breakdown (BD) that, for an optimized system (appropriate geometrical and physical parameters of design), will consist of a current sheath (CS) developed on the insulator surface as a gliding discharge. The electrical current I carried by the CS will interact with the magnetic field B self-generated by the current I, inducing a Lorentz force F ($F \propto I \times B$) which will accelerate the CS to the open end of the electrodes. During this run-down stage, the CS will sweep the gas that fills the interelectrode space, ionizing and incorporating it. When the CS reaches the electrode's end, the roll-off stage begins, collapsing into a dense plasma focus (DPF) consisting of a small plasma column co-axial to the electrodes and developed in front of the anode. For an optimized system (a combination of specific geometrical design parameters and specific physical parameters of operation) this DPF column is developed in the moment at which the external current discharge reaches its maximum value (a quarter of the period of the oscillating component of the damped oscillating current of a typical LRC circuit). The high intensity of the current that circulates through the DPF column provokes its magnetic compression (the Z pinch) with the development of Rayleigh–Taylor instabilities. These instabilities which appear as abrupt falls in the current–time traces (see figure 2) induce a fast change in the pinch inductance.

The geometrical and physical parameters of the system used in the experiments can be summarized as follows. The geometrical parameters were the centre electrode's (anode's) internal diameter, 14.3 mm; the external electrode's (earthed cathode's) internal diameter, 49 mm; the cathode's length, 67.5 mm; the anode's length, 70 mm; the electrodes' thickness, 1.7 mm; and the insulator's (Pyrex pipe's) length, 44 mm. The physical parameters were the capacitor bank's charging voltage, 20 kV; the capacitor bank's capacity, 4 μF; the period of the current discharge, 3.0 μs; and the gas (nitrogen and argon) operating pressure, 200 mTorr. Under these operating conditions a DPF column of about 1 mm diameter and about 7 mm length (observed through the x-ray image taken with a pin-hole camera) is developed in front of the anode with one of its extremes at the anode end.

2.2. The electrical diagnostics

A Rogowskii coil was used to monitor the external current discharge in a Digital Dual 600 MHz, 5 Gs s^{-1} oscilloscope. The signal from the Rogowskii coil is actually the temporal derivative $\dot{I}(t)$ of the current $I(t)$. Typical recorded traces of $\dot{I}(t)$ and the corresponding $I(t)$ (by the $\dot{I}(t)$ numerical integration) can be seen in figures 2(a) and (b) respectively, showing an oscillation with a characteristic period of 3 μs.

The energy liberated during the pinch formation can be observed as an abrupt fall δI of the external current discharge. This δI results in a sharp discontinuity (a 'spike') in the current temporal derivative trace whose height $\dot{I}_p$ is a measure of the change in the slope of $I(t)$. Thus, the pinch intensity can be associated with the magnitude of $\dot{I}_p$ and likewise the efficiency of the acceleration process of ions and electrons, neutrons from nuclear fusion production, electromagnetic bursts and so on.

2.3. The optical diagnostics

Optical emission spectroscopy (OES) has been used as a probing technique for glow-discharge diagnostics, having the advantage of providing *in situ* real-time information (depending on the time scale associated with the experiment considered), without disturbing the discharge. In the present paper, OES of excited species is used to study some processes taking place in the plasma generated in the plasma focus.

The OES system shown in figure 1 is comprised of a triple-grating monochromator (Jarrell-Ash 27 Monospec) with an optical multichannel analyser (1024 cooled photodiodes) with a time resolution per spectrum of 30 ms. Scans of the emission across the plasma volume were performed using a lens–diaphragm system, yielding a spatial resolution of 2 mm. In this manner, the plasma was monitored through a 5.6 mm diameter glass window, focusing on different distances z along the system axis Z, in front of the anode in the region of the DPF column. This condition observed includes, besides the DPF column, the radiation that originated along the line of sight from the plasma belonging to the remnant of the CS.

The small window used was located at the end of a cylindrical aluminium conduit of 5.6 mm diameter and 25 mm length, aligned with the optical focusing system (external to the vacuum chamber). This conduit allowed on the one hand the elimination of most of the light coming from outside the studied region (improving the spatial observation resolution) and on the other, the reduction of the light intensity to levels which did not saturate the photodiodes' storage capacity.

Experiments focusing on the region to be studied through a 150 mm diameter window (without the aluminium conduit) showed that there was complete saturation when the spectrometer was focused at $z = 0$, 5 and 10 mm from the end of the anode and along the DPF column, requiring a complementary neutral filtering (10% transmission) to reduce the intensity to observable intensity levels. Outside the DPF column region, at $z = 20$ mm for example, the level of intensity was strongly reduced, allowing direct observation of the spectra (without neutral filtering), exhibiting saturation only for the most intense emission lines. Far from the DPF region ($z \geq 100$ mm), the spectral intensities were strongly reduced and several bands corresponding to molecular species in the plasma were observed.

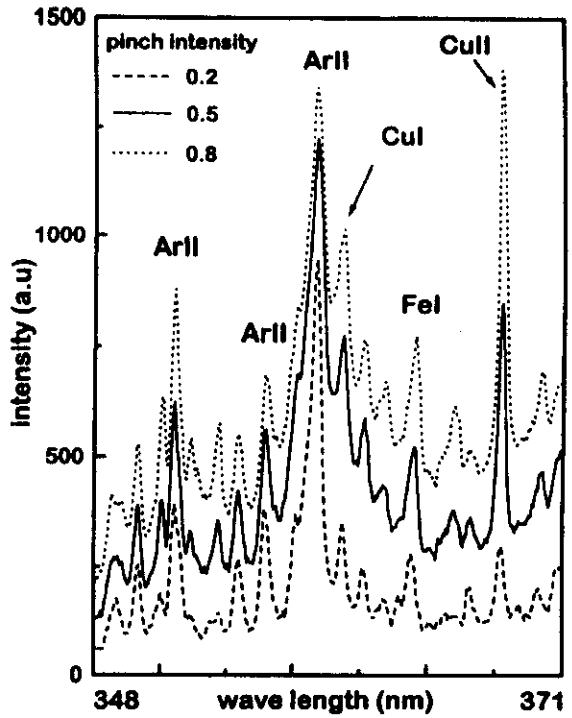

Figure 3. Three spectral profiles (within the spectral range 343–371 nm) corresponding to discharges with pinch intensities 0.2, 0.5 and 0.8.

The above considerations ensured that the spectra observed through the small glass window at the end of the aluminium conduit, belonged almost exclusively to the DPF column region. Taking into account the short duration of the PF discharge ($\tau = 3$ μs) and the spectrometer's sweeping time (about 30 ms), the acquisition of spectra corresponded to the time integration of the whole experiment.

3. Results

The experiments were carried out using argon or nitrogen as filling gases, at a pressure of 200 mTorr under continuous-flow conditions to maintain the gas purity. Two different gratings were used with linear dispersions of 24 and 3 nm mm^{-1}. The optical range studied extended from 340 nm (the wavelength of the spectral edge of the glass window used to monitor the discharge) to 700 nm. The spectra obtained during the experiments were calibrated against argon, helium and neon lamps for the whole range of wavelengths used. For each experiment, the spectrum was recorded simultaneously with the $\dot{I}(t)$ trace of the external current discharge.

All the most intense lines in the spectral range studied, reported in the tables listed in [6–9], corresponding to neutral species and ions of different degrees of ionization of the working gas, were observed. Lines corresponding

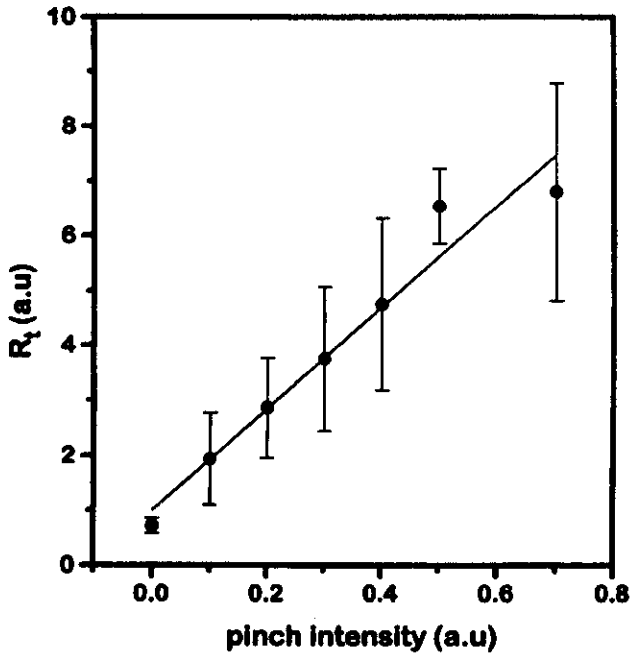

Figure 4. The total emission intensity (R_t) as a function of the pinch intensity for the spectral range 490–550 nm.

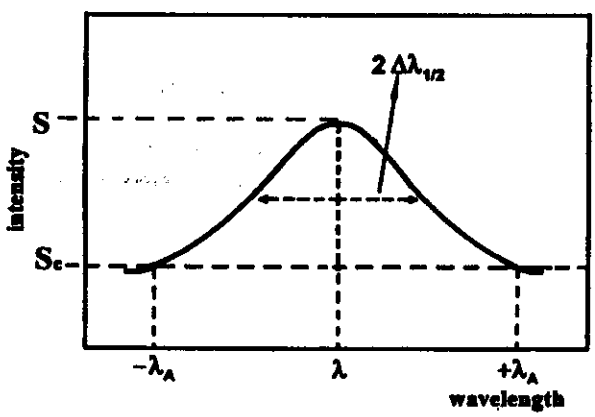

Figure 5. The method of line-intensity determination.

Table 1. Species observed in the spectra.

Element	Source	Species
Ar	Carrier gas	Ar I, Ar II, Ar III, Ar IV
N	Carrier gas	N I, N II, N III
Fe	Sputtering yield of the chamber	Fe I, Fe II
Cu and Zn	Erosion yield of the electrode system	Cu I, Cu II, Cu III, Zn I
Si	Erosion yield of the insulator surface	Si I, Si II, Si III, Si IV
C	Contamination	C I, C II
O	Contamination	O II, O III, O IV

to higher degrees of ionization were in the UV region and could not be viewed with the experimental set-up used. Besides the lines of the working gas, lines of the elements corresponding to the material of the solid parts of the experimental system (Cu, Fe, Si and so on) were recorded. A list of the species (atoms and ions) identified in the plasma is presented in table 1.

The observed spectra were composed of a series of lines superimposed upon a continuous radiation emission. For different discharges the continuum (likewise the intensity of some spectral lines) grew with the pinch intensity value, as can be seen in the example of figure 3. In order to study this behaviour, the total emission intensity, R_t, was determined for each experiment by measuring the area below the curve that described the spectrum (continuum plus line emission). For the different spectral regions considered, a linear correlation between R_t and the pinch intensity $\dot{I}_p$ was determined. This response was verified for different experiments using either argon or nitrogen as the filling gas. As an example, we present in figure 4 the results of argon discharges in the spectral region 490–550 nm using the grating with the highest spectral resolution.

The individual line intensity emission was determined by subtracting from the measured line intensity S the contribution of the continuum. This correction may be performed theoretically by using the line-broadening theory through the application of the wing intensity distribution formulae. For isolated lines [10] with a Lorentzian profile out into the far wings [11], it can be done geometrically as follows. It is assumed that the background in the neighbourhood of the line becomes approximately constant at the points $-\Delta\lambda$ and $+\Delta\lambda$, where λ is the central wavelength of the considered line (figure 5). Then it is possible to draw a straight line between these points to account for the continuous background intensity S_c. The error by which S is affected when S_c is measured 1 nm from the centre of the line is $\leq$10% [12], which is below the 13% [13] corresponding to the error associated with the full acquisition system.

This approximation of the background correction was verified for the isolated lines of the studied spectra [13]. A self-programmed code was used to test different profiles (Lorentzian, Gaussian and Voigt) for the experimental data fitting. For the isolated lines, the Lorentzian was the best profile for fitting in their wings.

For the carrier-gas emission lines it was found that their intensities were almost constant as the pinch intensity varied, even for experiments in which $\dot{I}_p = 0$. This behaviour was verified in experiments using pure argon or pure nitrogen. Also, for experiments in which a mixture of nitrogen with argon (25% Ar–75% N and 50% Ar–50% N) were used, the line intensities associated with each gas varied as the corresponding partial pressure, confirming these results.

In figure 6 the intensities of the 356.10 and 488.90 nm lines of Ar II are shown. These results were obtained by focusing on two regions of the DPF column centred at $z = 0$ and $z = 5$ mm.

A completely different response was noticed in the emission lines of the elements Si and Cu, belonging to the electrode system and to the co-axial insulator. The intensity of copper lines had an increasing relationship with $\dot{I}_p$, with a growth rate that depended on the line considered. In figure 7, the intensities for the 515.32 and 521.82 nm lines of Cu II are plotted for the two DPF regions mentioned above.

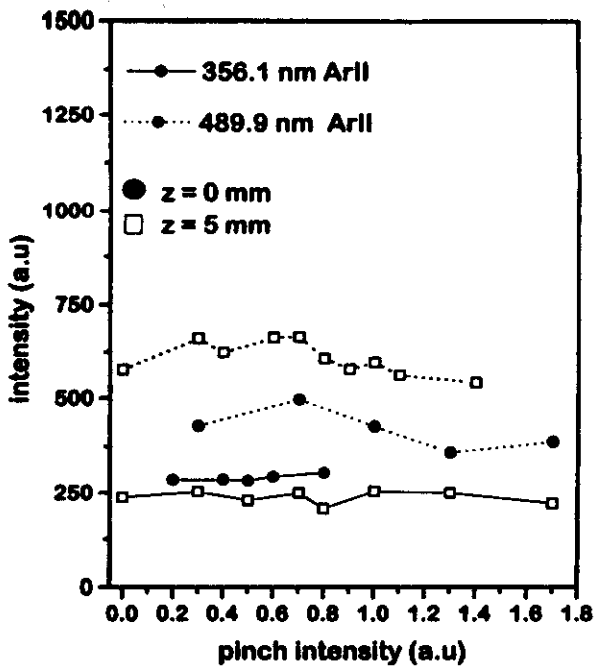

Figure 6. Emission intensities of argon lines observed in the DPF region at $z = 0$ and 5 mm.

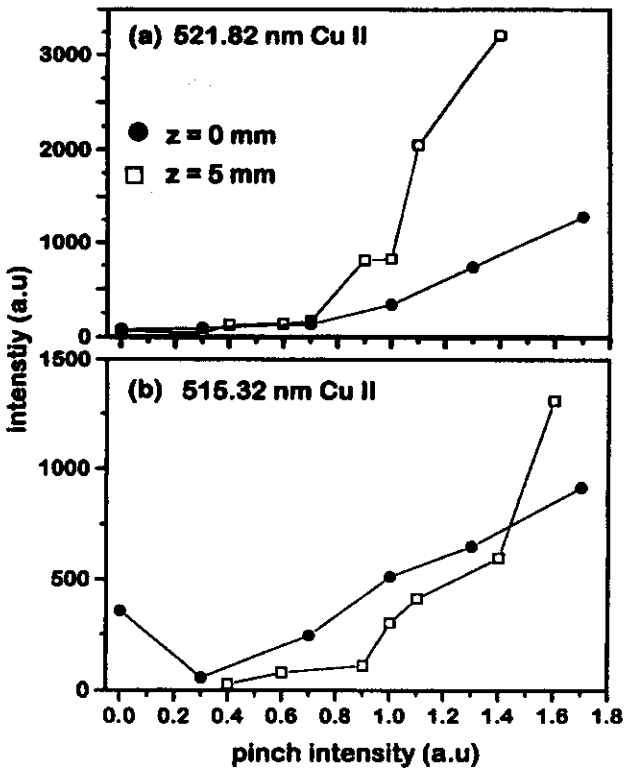

Figure 7. Emission intensities observed in the DPF region at $z = 0$ and 5 mm of (a) the 521.82 nm Cu II line and (b) the 515.32 nm Cu II line.

For silicon and its ions, the intensities had the same behaviour with respect to I_p as the one observed for the copper lines. However, in this case, emissions from neutral species and ions of up to the third ionization were observed for discharges with $I_p = 0$. The silicon was incorporated into the discharge during the breakdown phase due to the interaction of the discharge with the insulator's surface. The influx of silicon from other parts of the system (inside the vacuum chamber) can be considered negligible, because in the experiments the small 5.6 mm diameter glass window (at the end of the 25 mm aluminium conduit and far from the DPF region) was the only possible extra source of this element. These results are in accordance with the observation of a thin layer of silicon on the surface of the targets during ion implantation [14], which was attributed to the Si contamination of the discharges. In figure 8 the intensity of the variation of the 385.60 nm Si II line with the pinch intensity can be observed as an example, for three different experiments.

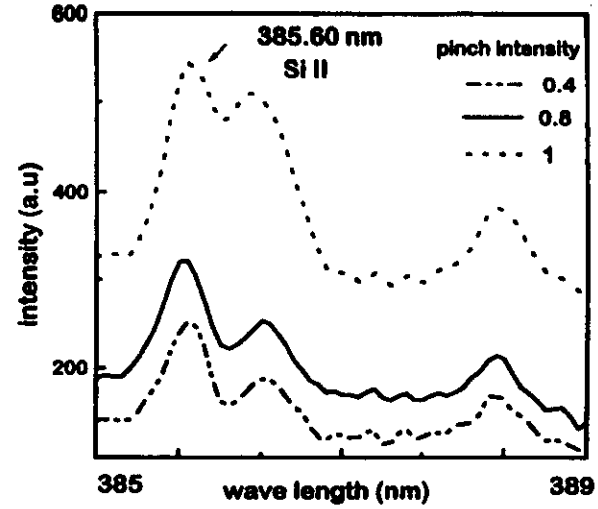

Figure 8. The emission intensity profiles of the 385.60 nm Si II line for experiments with various pinch intensities.

3.1. Experiments with the electrode surfaces partially covered with aluminium

To study the effect of contamination by the electrode walls, which in our experiments mostly corresponded to the copper ejected during erosion of the brass wall, the electrode surfaces were partially covered with a sheath of aluminium. This showed the weight of the contribution of the last centimetres of the electrode surface to the discharge contamination through the incorporation of aluminium into the plasma. To identify the aluminium lines, some spectra were recorded with the hollow anode front sealed with aluminium to obtain maximum emission intensities.

In figure 9, the results presented correspond to experiments in which (a) the last 20 mm of the internal surface of the external electrode (cathode) and (b) the last 20 mm of the external surface of the internal electrode (anode) were covered with 2 mm thick aluminium rings. The discharges were performed at 200 mTorr of Ar, focusing on the DPF column at $z = 5$ mm. It is possible to see in figure 9 that no aluminium lines appeared in the spectra in case (a), although the characteristic argon emission lines corresponding to this spectral range can be observed. Nevertheless, in case (b), the 358.66 nm lines of Al II and the 360.16 and 361.24 nm lines of Al III were detected.

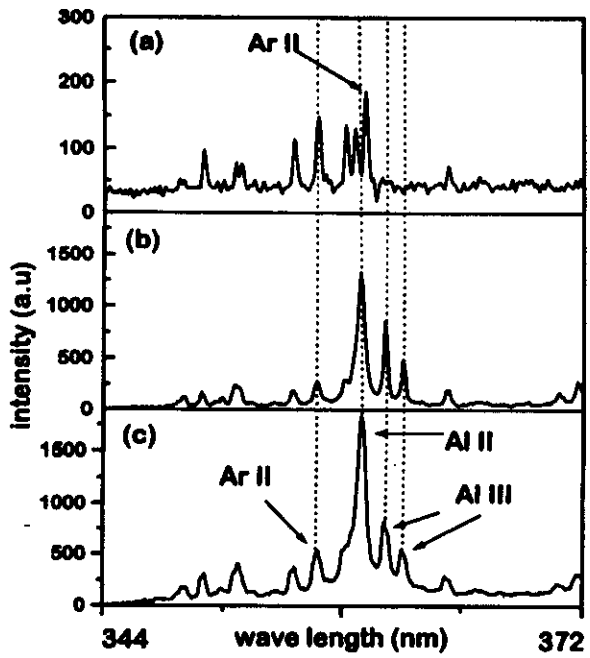

Figure 9. The emission line intensity of aluminium in experiments with argon as the filling gas: for (a) the internal surface of the cathode and (b) the external surface of the anode partially covered with aluminium sheaths; and (c) the anode front sealed with aluminium.

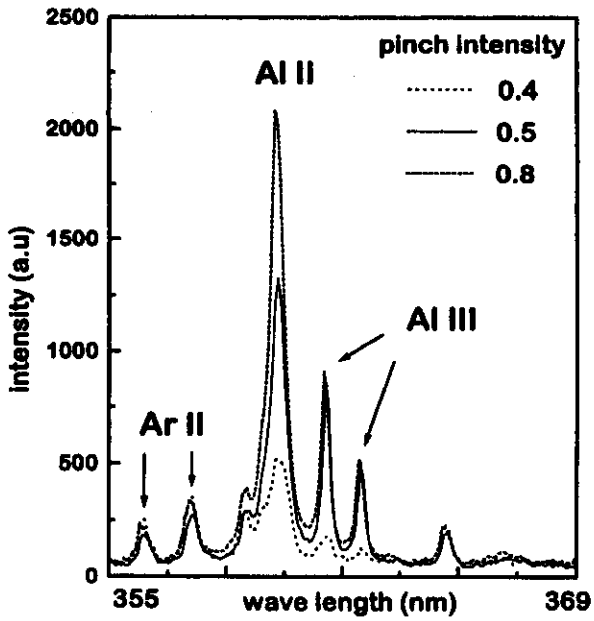

Figure 10. The emission intensity of the aluminium line in spectra corresponding to experiments with the external anode surface partially covered, with various pinch intensities.

As shown in figure 10, for the aluminium-covered anode, case (b), it was observed that the Al II line intensity increased with the pinch intensity, but no intensity variation was seen for the Al III lines. Different Ar II lines are indicated in the spectra to show their invariable intensities. These results corroborate the pinch-intensity dependence found for the Cu lines when the aluminium ring was not used in the experiments. On the other hand, the remaining contamination with copper (coming from the rest of the non-covered anode surface) was reduced.

These results show that the last part of the anode surface is critical in terms of the contribution of contamination to the plasma. This fact can also be corroborated through the strong erosion observed in the anode by simple eye inspection.

Finally, in the spectra (see figure 3) the presence of Fe was systematically observed. Its possible source was the stainless steel vacuum chamber. A series of ten discharges was carried out after the interior walls of the chamber had been covered completely with aluminium foil, to avoid direct contact between the plasma and the steel. In each discharge a spectrum was taken focusing the spectrometer on the DPF column at the $z = 5$ mm position, using the plasma focus with its electrodes in their normal mode of operation (without aluminium rings partially covering the electrode surfaces). The observed spectra were no different from those observed with the stainless steel surface of the internal chamber wall exposed to the plasma. No significant differences were found in the Fe line intensities and the aluminium spectral lines were totally absent. These results showed that the Fe lines did not originate directly from the plasma's interaction with the wall surfaces during each discharge.

Nevertheless, the only possible source of Fe was the chamber walls. It can be supposed that the Fe is removed during each discharge by the plasma current sheath remains and is deposited on the electrodes and other parts of the system, thus contaminating them. This electrode contamination could be the source, during each discharge, of the Fe introduced into the plasma together with the other species such as Cu.

4. Discussion

The experimental observation reported in this paper shows that the intensities of the lines belonging to the working gas (argon or nitrogen) showed no variation with the pinch intensity. Nevertheless, the intensities of the lines associated with the solid parts of the system (silicon, copper and aluminium) had an increasing dependence on the pinch intensity.

Considering the constancy of the line intensities of the working gas and the fact that the gas density (working pressure) was the same for all the experiments, it is possible to associate the growths of the line intensities corresponding to Si, Cu and Al with increases in their concentrations in the plasma.

In [15] two types of extreme conditions of breakdown were observed. One corresponded to a diffuse process, in which a current precursor on the cathode was detected (before the CS reached the electrode) with a current distribution that was concentrated within a thick (about 1 cm) sheath. The other was a more localized one, in which the discharge was generated on the insulator surface as a thin dense current sheath. In addition, in [14] the results obtained with a device similar to the one used in the present work showed that the experimental conditions

under which the plasma focus experiments had maximum pinch intensities coincided with those under which thinner sheaths were formed during the breakdown.

The correlation found in this work between the concentration of silicon and the pinch intensity reinforces the idea of the formation of high-density current sheaths on the insulator surface during the breakdown stage, for better DPF development. In discharges with higher pinch intensities, the insulator undergoes a more intense and localized erosion that results in an increase in the concentration of silicon in the plasma.

In the same way, the elements belonging to the electrodes are incorporated into the discharge during the run-down and roll-off stages through various mechanisms such as sputtering by the ions on the cathode and an arc-spot-like process on the anode surface.

Thinner current sheaths (which correspond to higher pinch intensities) will deliver to the electrode surfaces higher power densities during their passage (during the first quarter of the period of the discharge) from the back to the front end of the gun. This higher density of power deposition will result in more energetic removal of material, increasing the amount of atoms of the solid elements (Cu, Al, Fe and so on) incorporated into the plasma. At the same time, the energy stored in the current sheath continuously increases from the breakdown stage to the formation of the DPF at the front of the gun. This effect is due to the variation of the voltage (between the electrodes) during the first quarter of the period of the discharge, which follows the same sinusoidal function as the external current discharge, giving the maximum material removal at the surface close to the end of the gun, just when the voltage reaches its highest value. This fact was corroborated by inspection of the electrodes' surfaces, showing that the maximum erosion had occurred at the open end of the gun.

Regarding the centre electrode for example, the high-power electron energy deposition on the anode wall evaporates and ionizes the atoms of the material, incorporating them into the plasma of the current sheath. Those ions, once in the dense plasma column, are ionized to higher degrees of ionization, being responsible for the variation of the line intensity with the intensity of the pinch.

5. Conclusions

The results show that plasma focii are prolific spectroscopic line generators. In our experiments, all the most intense lines in the optical range studied, corresponding to the degrees of ionization of the elements existing in the discharge (carrier gases, impurities generated during the interaction of the discharge with solids surfaces and so on) were observed. Considering the physical conditions of the discharges in these devices, it is possible to predict their use as a source of radiation to study forbidden transitions. Nevertheless, for this purpose, a higher resolution spectrometer should be used.

On the other hand, the response of the emission lines to the pinch intensity observed in the present work confirms the importance of the initial stage of the discharge (breakdown) and the current-sheath-propagation stage (run down) in the formation of the plasma focii.

Considering the possibilities of the plasma focus as a surface-modification apparatus, through the combined effect of ion implantation and strong thermal irradiation shock, and the inconvenience created by the impurities added to the original ion beam (ions of the carrier gas species), the results in this work show the feasibility of some experimental corrections. It possible to reduce the amount of impurities in the discharge by replacing only the last centimetres of the centre electrode by an appropriate material. Thus, the bulk of the electrode can remain copper, a desirable material due to its electrical (conductivity) properties for optimized functioning of a plasma focus. This replacement not only can be done with materials with higher evaporation temperatures (tungsten for example), but also with those that present a certain compatibility between the impurity and the eventual surface to be treated, such as iron when a steel surface is implanted.

Acknowledgments

The authors thank J Reyna Almandos for helpful suggestions on the analysis of spectra and A Muñoz for his collaboration in the experimental work. This work was performed under CONICET grant BID-PID 222, International Atomic Energy Agency Research contract 6477/RB and International Centre for Theoretical Physics TWAS research grant MP 90-090.

References

[1] Nardi V, Bostick W, Feugeas J and Prior W 1980 *Phys. Rev.* A **22** 2211
[2] Nardi V, Bostick W, Feugeas J, Prior W and Cortesse C 1979 *Nucl. Fus.* (suppl.) **2** 143
[3] Feugeas J 1989 *J. Appl. Phys.* **66** 3467
[4] Feugeas J, de Gonzalez C O and Sánchez G 1994 *Radiat. Eff. Defects Solids* **128** 2267
[5] Mather J W 1985 *Plasma Phys. Cont. Nucl. Res.* C **21/80** vol 2 (Culham: IAEA)
[6] Kaufman V and Edlén B 1974 *J. Phys. Chem. Ref. Data* **4** 825
[7] Norlén G 1973 *Phys. Scr.* **8** 249
[8] Pettersson S 1982 *Phys. Scr.* **26** 296
[9] Reader J and Corliss C (eds) 1992 *NIST Spectroscopic Properties of Atoms and Atomic Ions Database Version 1.0* (Gaithersburg: NIST)
[10] Wiese W L and Shumaker J B 1961 *J. Opt. Soc. Am.* **51** 937
[11] Griem H 1962 *Phys. Rev.* **128** 515
[12] Wiese W 1965 *Plasma Diagnostic Techniques* ed R Huddlestone and S Leonard (New York: Academic)
[13] Grigioni G 1995 *PhD Dissertation* Universidad Nacional de Rosario
[14] Feugeas J and Von Pamel O 1989 *J. Appl. Phys.* **66** 1080
[15] Gurevich A 1961 *Sov. Phys.–JETP* **12** 904

J. Phys. D: Appl. Phys. 30 (1997) 927–936. Printed in the UK PII: S0022-3727(97)74749-1

The thermal evolution of targets under plasma focus pulsed ion implantation

G Sánchez and J Feugeas

Instituto de Física Rosario (CONICET-UNR), Boulevard 27 de Febrero 210 bis, 2000 Rosario, Argentina

Received 22 May 1996, in final form 23 August 1996

Abstract. Pulsed ion beam implantation with plasma focus has proved to be an effective method of metal surface treatment for tribological purposes. Nevertheless, the pulsed nature and the continuous energy spectrum of the ion beams differ from those of the standard ion implantation processes. In this paper a model of the thermal evolution of the surface layers of stainless steel, titanium and copper, during and after nitrogen and argon ion beam incidence, is presented using the finite-difference method.

In the calculations, the geometry and physical characteristics of the ion beams, the single-ion–solid interaction process and the thermal properties of the materials were used. The results showed a strong thermal effect consisting in the generation of transitory heating slopes and heating speeds as high as ~3600 K μm^{-1} and ~40 K ns^{-1} respectively, with maximum temperatures that can reach even the material evaporation point at the surface layers. The cooling down process, through the thermal conduction mechanism at the target bulk, turns out to be fast enough to produce the complete thermal relaxation of the target in only a few microseconds after the end of the ion beam incidence. The results presented are contrasted with experiments performed in similar conditions to those used in the numerical model.

1. Introduction

Experiments of surface treatment with plasma focus (PF) showed excellent results in hardening and wear reduction of different types of steel and pure titanium. PF is basically a Z-Pinch experiment induced by a fast, energetic electric discharge in a coaxial electrode system which has been investigated in its two geometries, Mather [1] and Filipov [2] types, since the 1960s. Experiments using deuterium as the filling gas showed the development of nuclear fusion reactions, during the maximum compression stage of the plasma column. These reactions, for a PF of similar physical and geometrical characteristics as those used in our experiment, are observed through the emission of bursts of $\sim 10^8$ neutrons per discharge, a consequence of the deuterium–deuterium nuclear fusion reactions.

In addition, bursts of hard and soft x-rays, ultraviolet, visible light, infrared and microwave radiation, with pulsed energetic ion and electron beams are simultaneously emitted. Precisely the study of these ion beams was begun by Feugeas *et al* [3] as a surface treatment process for metals with tribological purposes, showing in its first work a wear reduction by a factor of ~20 in austenitic AISI 304 stainless steel, after nitrogen ion implantation, with Fe_2N phase formation. Also, the wear resistance of high-speed steel (M2 type) was enhanced by a factor of 2.3 after nitrogen ion implantation [4]. On the other hand, in nitrogen implanted pure titanium, a high (~50 at.%) and uniform (within ~5000 Å depth surface layer) nitrogen concentration was found, with titanium nitride compound formation, driving to an important increase in microhardness [5].

These results, that can be associated with the nitrogen inclusion in the surface through the implantation process exclusively, are accompanied by others like the observed change of residual stresses from a compressive to tensile state on AISI 304 stainless steel after nitrogen or argon ion beam implantation and the induced concave residual deformation after the nitrogen and argon ion implantation of several different metals and alloys.

These last results, together with the observation of surface melting for several experimental situations, can be associated with a fast and strong thermal effect due to the pulsed nature of the ion beam (high-energy deposition).

Consequently, a better understanding of this fast thermal effect is necessary to fully characterize the PF ion implantation process. Nevertheless direct measurements of the target's thermal evolution under PF ion implantation require depth resolution superior to 1 μm (layer thickness affected) and time resolution superior to 1 μs (temporal extension of the process) which are, from a technological point of view, almost impossible to satisfy simultaneously.

In this work the thermal effect is studied using numerical simulation calculations based on the PF ion beam characteristics, ion–solid interactions and the thermal properties of matter. The results of the calculations are compared with some experiments on PF ion implantation on different materials.

0022-3727/97/060927+10$19.50

2. The plasma focus device

The plasma focus (PF) functioning, which is schematized in figure 1, is well known and can be extracted from the abundant existing literature since the early work of Mather in 1965 [1].

In our experiments we have used a system with a Mather type geometry with an electrode total length $L = 70$ mm and external diameter $\phi = 70$ mm. The operating pressure in all cases (for argon and nitrogen filling gases) was 200 mTorr, resulting in a discharge with an oscillating component of 3.4 μs period.

The observed dense plasma focus column (DPF) in front of the gun was ~7 mm in length and ~1 mm in diameter, with a maximum circulating current of 200 kA. It is during the DPF formation when the nuclear fusion reaction takes place (if deuterium is used as filling gas), together with other energetic processes such as ion and electron beam acceleration. In our case, those ion beams were used for surface treatment purposes.

Nevertheless, the accelerating physical mechanisms are not well understood, being under research today by several groups in the world. In spite of this, several general features associated with the ion beams can be seen in the literature [6–8]. The ion beams are principally accelerated at the front of the gun with an angular distribution which gives a maximum fluence on the axis (0° in figure 1), a fluence which decreases gradually with increasing angle inside a conic geometry. This characteristic was indirectly corroborated in our experiments through the damage left on the target surfaces after being exposed to the ion beams. The damage had a circular distribution with a gradual reduction of its intensity from the centre (aligned with the symmetry axis of the gun) to the edge, becoming negligible for angles greater than 40°. For simplicity in our calculations, we have considered an ion beam with conic geometry with a solid angle of 40°. On the other hand, and in spite of the temporal non-uniformity in the ion beam acceleration (observed by several authors), also for simplicity in the calculations, we have considered that the acceleration process is uniform and that it lasts ~200 ns, duration of the x-ray burst profiles measured by the use of a pin diode with a 12.5 μm thick beryllium foil window.

Another feature to be taken into account is the ion beam energy spectrum. The ions are accelerated with a continuous energy spectrum whose measured spectral law varies, among different authors, with the energy of the experiment (stored energy in the capacitor bank), with single-ion energy which goes from a few tens of keV to several tens of MeV. Nevertheless, in all cases, the dependence showed a fast decrease in the number N of ions with energy E for increasing values of E, following a general law that can be expressed as

$$\frac{dN}{dE} \propto E^{-x} \tag{1}$$

with x ranging between 2.0 and values that can be greater than 5.0.

In our case, we used the value $x = 3.5$ given by several authors [7], within the range of energies 20 keV $< E <$ 500 keV [8]. The lower value of 20 keV was chosen because it corresponds to the maximum voltage applied on the PF electrodes (capacitor bank charging voltage) at the moment of the DPF formation. The maximum value of 500 keV was arbitrarily selected, taking into account the strong reduction in the number of ions N beyond this energy.

However, the total number of emitted ions is a difficult experimental observation and the constant of proportionality of equation (1) has to be determined indirectly by comparing macroscopic experimental and numerical results. In our case, the number of ions will be determined by adjusting the constant of proportionality for the equation (1) to the ion flux (or energy flux) necessary to produce certain observed surface damage, associated with an incipient melting process, produced onto targets located at different distances ℓ from the DPF where the implantation was performed (see figure 1).

3. Numerical evaluation of thermal effect of pulsed ion implantation

The problem consists of the study of the thermal evolution of an implanted target with ion beams with the characteristics described above. The one-dimensional heat conduction equation with an energy source is solved by the finite-difference method, considering the ion beam as the energy source contribution.

3.1. Ion beam modelling

To find expressions for the ion number and the energy distribution, relation (1) is written as an equality using a constant of proportionality α which will be determined later:

$$\frac{dN}{dE} = \alpha E^{-3.5} \tag{2}$$

with E constrained in the range 20 keV $\leq E \leq$ 500 keV.

If equation (2) is integrated between 20 keV and E, the number of ions with energy in this interval can be obtained:

$$N(E) = \frac{\alpha}{2.5}[7.54 \times 10^{-4} - E^{-2.5}]. \tag{3}$$

From (3), the inverse function $E(N)$ can be obtained:

$$E(N) = \left[7.54 \times 10^{-4} - \frac{2.5}{\alpha}N\right]^{-0.417}. \tag{4}$$

To perform the numeric calculation it is necessary to discretize the continuous variables N and E partitioning the energy interval in subintervals of length ΔE. The ith energy subinterval is in the range between E_i and $E_{i+1} = E_i + \Delta E$. The number of ions n_i within the energy subinterval can be obtained as

$$n_i = N(E_{i+1}) - N(E_i) \tag{5}$$

where $N(E_{i+1})$ and $N(E_i)$ are calculated from (3).

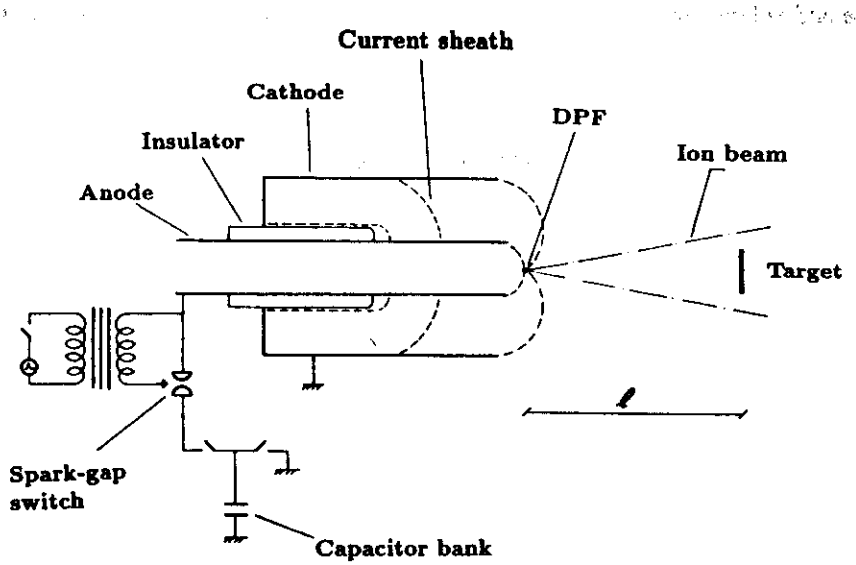

Figure 1. A diagram of the plasma focus device.

Making ΔE small enough, it is possible to associate a mean energy per ion e_i with the n_i ions of a subinterval calculated from (4) as

$$e_i = \frac{1}{n_i}\int_{N(E_i)}^{N(E_{i+1})} E(N')\,dN'. \tag{6}$$

The ion beam fluence f_i in such interval can be quoted as

$$f_i = \frac{n_i}{\sigma_\ell} \tag{7}$$

where σ_ℓ is the ion beam cross section of the beam at a distance ℓ from the focus. In this case, and considering the beam conical geometry, it can be calculated as

$$\sigma_\ell = \pi(\ell \tan 20°)^2. \tag{8}$$

The corresponding energy fluence ε_i in such a subinterval becomes

$$\varepsilon_i = f_i e_i. \tag{9}$$

3.2. Temporal characteristics of the beam

As mentioned above in section 2, for calculation purposes, we have assumed that the acceleration process occurs in the DPF column and lasts 200 ns, and that the ions are emitted during the entire interval with the same spectral law, same geometry and uniform flux. Calculation of the ion flux at the target location, the ion emission condition, the beam geometry and the different time of flight for ions with different energies all have to be considered.

The first ion that arrives at the target will be one of maximum energy (E = 500 keV), accelerated at the beginning of the acceleration process (t = 0). The last ion will be one of the minimum considered energy (E = 20 keV) and accelerated at the end of the acceleration process (t = 200 ns). The lapse between the arrival of the first and the last ion to the target is the time t_l in which the implantation process (IP) takes place and can be calculated as

$$t_l = 200\text{ ns} + \frac{\ell}{\sqrt{6.408\times10^{-15}\text{ m}^{-1}}}. \tag{10}$$

In the same way, and considering only ions from an energy interval (E_i, E_{i+1}), the first ion of such an interval to arrive at the target will be one with energy E_{i+1} and accelerated at t = 0, and the last, one with energy E_i and accelerated at t = 200 ns. The n_i ions of the ith energy subinterval will interact with the target in a lapse $\Delta\tau_i$:

$$\Delta\tau = \tau_i - \tau_{i+1} \tag{11}$$

where τ_{i+1} and τ_i are the arrival time of the first (at $t = \tau_{i+1}$) and the last (at $t = \tau$) ions of such an interval of energy to the target. Using equations (9) and (11), the energy per time and area unit delivered at the target by the ions of the ith subinterval can be obtained as

$$\mathcal{E}_i = \frac{\varepsilon_i}{\Delta\tau_i}. \tag{12}$$

3.3. Energy delivery into the target

When an ion penetrates into the target it loses energy by collisions until it stops at a certain depth below the target surface. This depth is called the projected range R_p and it depends on the ion mass, ion energy and target nature and density.

In this work the energy transference from the ion beam to the target is considered as an energy flux released in layers, of thickness defined by R_p, below the surface. It is assumed for simplicity that the whole kinetic energy of the ion is transformed into thermal energy into the bulk of the target. The range R_p for each particular situation and for each ion energy was calculated using the TRIM code [9].

For ions with energy in the ith subinterval the mean projected range $\langle R_P\rangle_i$ is defined as

$$\langle R_P\rangle_i = \tfrac{1}{2}(R_p^{i+1} + R_p^i) \tag{13}$$

where R_p^i is the projected range of ions with energy E_i.

The energy per time and volume unit delivered by the ions of the ith energy subinterval into the target $\dot{q}_i$ can be obtained through the equation

$$\dot{q}_i = \frac{\mathcal{E}_i}{\langle R_P \rangle_i}. \tag{14}$$

A point at any depth d into the target will receive energy from the ions with $r_p \geq d$. The energy flux delivered by the ion beam into that point is

$$\dot{Q}_d = \sum_i \dot{q}_i \tag{15}$$

where $\dot{q}_i$ is given by (14) and the summation is extended over all i that satisfy the condition $\langle R_P \rangle_i \geq d$.

3.4. Thermal evolution of the target

To calculate the thermal evolution of an implanted target under the described conditions, the one-dimensional heat equation

$$\frac{\partial^2 T}{\partial x^2} + \frac{\dot{\phi}}{k} = \frac{1}{a}\frac{\partial T}{\partial t} \tag{16}$$

has to be solved.

In equation (16) T is the temperature, $\dot{\phi}$ the energy flux, x denotes the variable depth in the target, t is the time, k the thermal conductivity and a the thermal diffusivity of the material given by

$$a = \frac{k}{\rho c_p} \tag{17}$$

where ρ is the density and c_p is the specific heat of the material.

The finite-difference method is applied in the resolution of equation (16). To implement this method the spatial and temporal domains are divided in small subdomains of length Δx and Δt. One node is assigned to each spatial subdomain, Δx being the distance between nodes and w the total number of nodes. After transforming the equation (16) into a finite-difference equation, the temperature in node j at time t is

$$T_j^t = \frac{1}{M}(T_{j-1}^{t-1} + T_{j+1}^{t-1}) + \left(1 - \frac{2}{M}\right) T_j^{t-1} + \dot{Q}_j^{t-1} \tag{18}$$

where

$$\dot{Q}_j^{t-1} = \frac{\dot{\Phi}_j^{t-1} \Delta x^2}{kM} \tag{19}$$

and

$$M = \frac{\Delta x^2}{a \Delta t} \tag{20}$$

with $j = 1, \ldots, w-1$. The finite difference method ensures convergence if [10]

$$M > 2. \tag{21}$$

In equation (18) T_j^1 gives the temperature in a node j at time t, having received in the instant $(t-1)$ an energy flux $\dot{\Phi}_j^{t-1}$, and using its own and its neighbour's temperature in the instant $(t-1)$.

In this work we consider as the energy source the energy transferred by the beam, which then defines the energy flux. If Δx is small, it can be assumed that the energy transferred by the ions in such a thickness is constant; thus the energy flux can be calculated as

$$\dot{\Phi}_j^{t-1} = \sum_i \dot{q}_i^{t-1} \tag{22}$$

where $\dot{q}_i^{t-1}$ is the energy per volume and time unit transferred by the ions with energy in the ith subinterval given by (14). The summation is extended over all i that satisfy the condition $\langle R_p \rangle_i \geq j \Delta x$.

For a node that does not receive energy, $\dot{Q}_i^{t-1}$ vanishes in equation (18).

In these calculations, we will neglect thermal losses by the surface through the two possible mechanisms, convection and radiation. Then the temperature for the node exposed to the beam, $j = 0$, can be quoted through the equation

$$T_0^t = \left(1 - \frac{2}{M}\right) T_0^{t-1} + \frac{2}{M} T_1^{t-1} + \frac{2}{M} \dot{Q}_i^{t-1} \tag{23}$$

and that for the last node, $j = w$, through

$$T_w^t = \left(1 - \frac{2}{M}\right) T_{w-1}^{t-1} + \frac{2}{M} T_w^{t-1}. \tag{24}$$

When a node reaches the melting (during heating) or solidifying (during the cooling down) temperature of the target material, a phase change takes place. The exact solution of this problem is complicated, and a simple model is proposed.

Each node can be represented by a mass density given by

$$\rho_j = \rho \Delta x. \tag{25}$$

The amount of mass Δm_j^t molten or solidified at the instant t in the jth node can be calculated by

$$\Delta m_j^t = \frac{\Phi_j^{t-1}}{L} \tag{26}$$

where Φ_j^{t-1} is given by equation (22) and L is the melting (or solidifying) heat. The remaining mass in the original phase at the instant t is

$$\Delta \rho_j^t = \rho_j - \Delta m_j^t.$$

When a phase change in a node takes place, its temperature is kept fixed until the total mass of the node is molten (during heating) or solidified (during cooling down).

If the evaporation point is reached, mass transport and other additional physical considerations should be taken into account. We will not consider such extreme cases of heating in this work.

Heat losses from the surface through convective processes were neglected because the low pressure of the filling gas ($\leq$200 mTorr) and the extremely short duration of the whole process do not allow any important transport of matter.

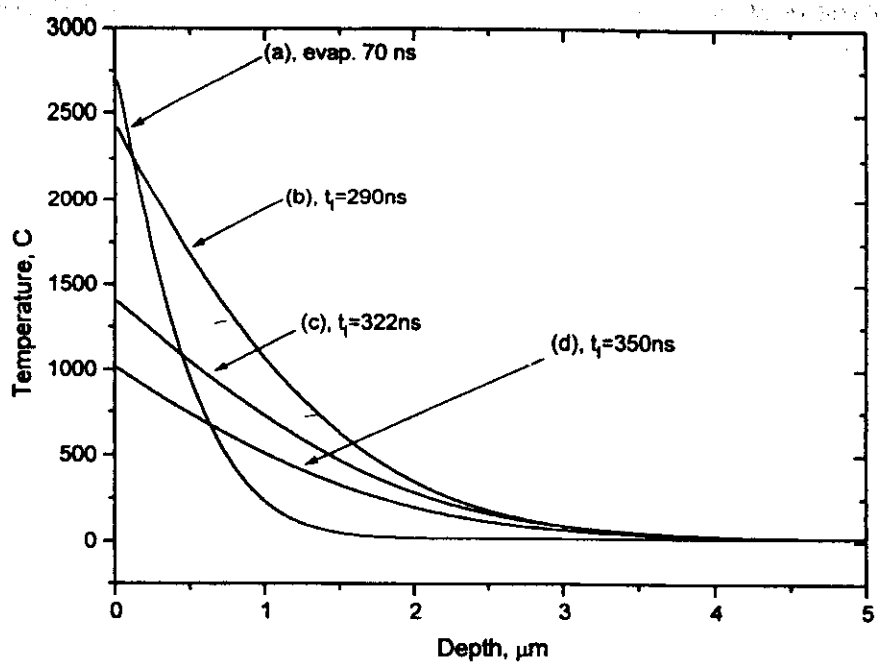

Figure 2. Thermal gradients of nitrogen implanted stainless steel at the end of IP. (a) ℓ = 40 mm, (b) ℓ = 60 mm and (c) ℓ = 80 mm, (d) ℓ = 100 mm.

The calculations start defining arbitrarily the ΔE value, which fixes the n subintervals of the whole range of energy considered. Now, Δx (the spatial domain partition) can be determined as

$$\Delta x = \frac{1}{n}\sum_{i=0}^{n}[\langle R_p\rangle_{i+1} - \langle R_p\rangle_i] \qquad (27)$$

where $\langle R_p\rangle_i$ and $\langle R_p\rangle_{i+1}$ are using equation (13). The duration Δt of the temporal domain partition can be calculated through equations (17), (20), (21) and (27).

Using equations (18)–(24) instantaneous temperature profiles are obtained considering the temperature dependence of the material thermal properties.

4. Calculation procedures

4.1. Determination of α

The first step in the process of calculation is the determination of the α parameter (equation (2)), which is related to the ion flux at the region of acceleration. The procedure followed in this work is related to the flux variation with the distance ℓ due to the conic geometry of the beam (which modifies the beam cross section with ℓ), and the multiple energy of the ions that modifies the flux by the differentiated time of flight in at distance ℓ.

To quantify α, we use the experimental observation of different material surfaces exposed to the beams at different distances ℓ, with the purpose of melting induced damage detection. The maximum ℓ at which some damage is observed indicates the energy flux limit for which the material melting point is reached.

For a nitrogen implanted titanium [5, 11] sample located at ℓ = 40 mm, the surface was totally damaged within the beam incidence area. The damage degree is gradually reduced for larger ℓ becoming imperceptible for ℓ = 150 mm.

In copper, nitrogen and argon ion implantation [12, 13] did not produce any damage even at the short distance used (ℓ = 40 mm), showing that the copper melting temperature was not reached.

For stainless steel the results can be detailed as follows [14].

(i) ℓ = 40 mm: strong damage observation showing material ejection from surface due to an evaporation process.

(ii) ℓ = 60 mm: damage observation showing that the melting temperature was reached.

(iii) ℓ = 80 mm: low damage observation showing that the melting temperature was reached, but in shallower layers than the preceding case.

(iv) ℓ = 100 mm: no damage observation showing that the melting temperature was not reached.

With these results, temperature profiles for nitrogen implanted stainless steel were calculated for several predetermined α values using adequate ΔE, Δx and Δt values. The chosen α, for which the calculated temperatures satisfy the experimental observations, was:

$$\alpha = 1.12 \times 10^{19}\text{au}.$$

In figure 2 the temperature profiles at the end of IP, calculated for nitrogen implanted stainless steel for different ℓ values using the selected α value, are shown.

4.2. Parameters selection

The first problem to be solved was the size selection for ΔE, Δx and Δt to maximize the precision of the results

Table 1. Parameters of calculation.

Implantation case	ΔE (keV)	Δx (μm)	Δt (ns)
N → AISI 316	25	0.019	0.030
Ar → AISI 316	25	0.011	0.009
N → Cu	25	0.022	0.002
Ar → Cu	40	0.017	0.001
N → Ti	25	0.027	0.050

ensuring, at the same time, convergence for the temperature profiles.

This convergence analysis was done for all the ion–material pairs used in this work, argon implanted copper being the less restrictive case, where the convergence condition is verified for $\Delta E \leq 40$ keV. Nevertheless, nitrogen implanted stainless steel convergence is ensured only if $\Delta E \leq 25$ keV.

Once ΔE is selected, the number of nodes for finite-difference calculations (and then matrix and vector sizes) was defined through the Δx predetermination. Therefore the maximum possible ΔE was selected to minimize RAM requirements during calculations.

On the other hand, and taking into account that the Δt value has no incidence in the result while condition (21) is verified, the maximum value that verifies condition (21) was selected with the purpose of minimizing the calculation line.

According to these criteria the results are independent of the selected parameters. The set of parameters used in this work is summarized in table 1.

5. Results and discussion

The results for several specific cases are presented in figures 3 and 4. In the figures, the temperature profile in the surface layers at different times during the ion beam interaction with the target, and several microseconds after the end of the implantation process (cooling down stage), are presented.

Figure 3(a) shows the thermal evolution of a nitrogen implanted stainless steel target located at $\ell = 80$ mm. The melting point is reached at $t = 240$ ns, lasting up to the end of the implantation process ($t_I = 320$ ns) without evaporation.

At the end of IP the maximum thermal gradient $\nabla_{N \to SS} \sim 400$ K μm^{-1} and the heating speed $V_{N \to SS} \sim 7$ K ns^{-1} were reached.

Figure 3(b) corresponds to the same experimental situation but for the case $\ell = 100$ mm, showing lower temperatures than for the preceding case. At the end of IP ($t_I = 350$ ns), the surface temperature is ~1000 K below the melting point of the stainless steel. Also, lower thermal gradients ($\nabla_{N \to SS} \sim 300$ K μm^{-1}) and heating speed ($V_{N \to SS} \sim 4$ K ns^{-1}) were found.

In both cases a fast cooling down process can be appreciated.

Figure 4 shows the thermal evolution of nitrogen implanted titanium (part (a)) and copper (part (b)) targets for a distance location of $\ell = 100$ mm. It can be seen in titanium that the surface temperature should be higher than the melting point at the end of IP showing the presence of an evaporation process. In contrast, for the copper case, the peak surface temperature is considerably lower: ~360 K. The same thermal behaviour differences result in the thermal gradient which turns out to be for Ti $\nabla_{N \to Ti} \sim 650$ K μm^{-1} and for copper $\nabla_{N \to Cu} \sim 31$ K μm^{-1}, and for the heating speeds which for Ti and Cu were $V_{N \to Ti} \sim 7$ K ns^{-1} and $V_{N \to Cu} \sim 2$ K ns^{-1}, respectively. This behaviour is in agreement with the differences between the thermal parameters of the two materials.

Based on the model presented it is possible to analyse the calculated energy deposition profiles.

Figure 5 shows the temporal dependence of the energy delivered into a stainless steel target by nitrogen ions for the $\ell = 40$ mm (curve A) and $\ell = 100$ mm (curve B) cases. The reduction in the deposited energy observed in curve B is a consequence of the reduction of the ion fluence due to the beam conical geometry, and the flux reduction due to the increase in the temporal width by the differentiated ion time of flight.

Figure 6 shows the delivered energy in stainless steel as a function of the depth for nitrogen ions for the $\ell = 40$ mm (curve B) cases, and for argon ions for the $\ell = 100$ mm (curve C) case. From these figures it can be seen that almost all the energy is deposited into the first 0.1 μm below the surface, a thickness that corresponds to the projected range of ions with energy lower than 100 keV for nitrogen and 200 keV for argon [9]. These results suggest that the assumption of considering ion energy between 20 and 500 keV is appropriate.

The radiation losses, on the other hand, can be estimated from the temperature values obtained. The radiation of thermal energy is a very complex problem since the emissivity of a given material depends on its composition, surface morphology and production method. However, based on the nitrogen implanted stainless steel results and considering the emissivity of polished steel as 0.55 [15], a value of 3×10^{-3} J cm^{-2} of radiated energy during 1 μs during the cooling process can be estimated. In this situation the surface temperature at the end of IP is 2800 K (figure 2(b)) and the calculated total energy received by the target during the IP is ~1 J cm^{-2}. This radiated energy is several orders of magnitude below the energy received from the ion beams, and it is possible to conclude that the radiated energy in the cooling stage is negligible compared with the energy transferred by the ion beams.

6. Conclusions

Surface profiles of thermal evolution of targets irradiated with pulsed ion beams generated with plasma focus were calculated using numerical simulation. The model used was based on the physical and geometrical characteristics of the ion beams, the single-ion–solid interaction, the thermal properties of selected materials, and the neglect of the thermal loss by the surface through processes such

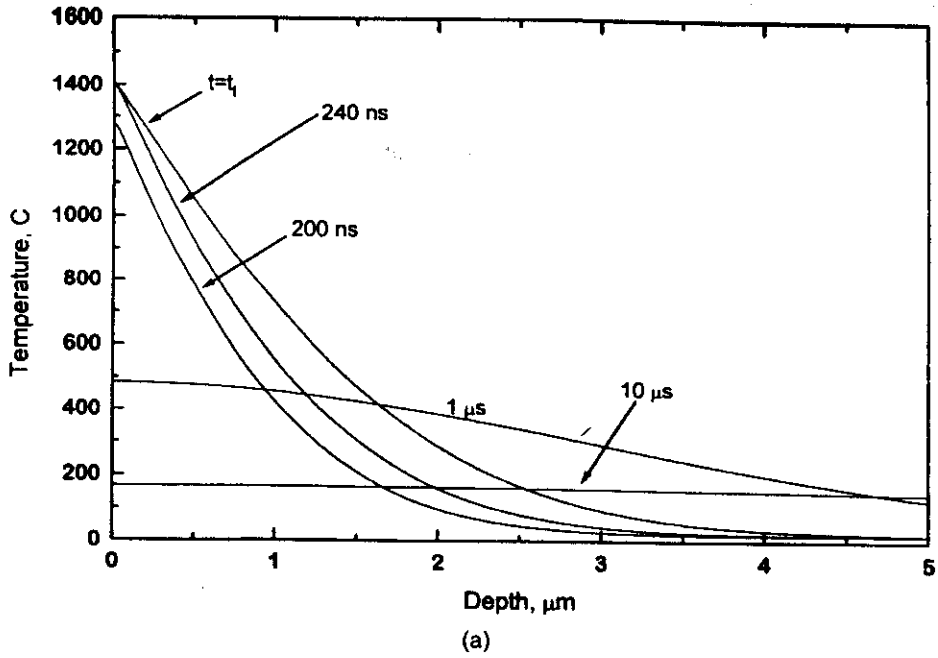

(a)

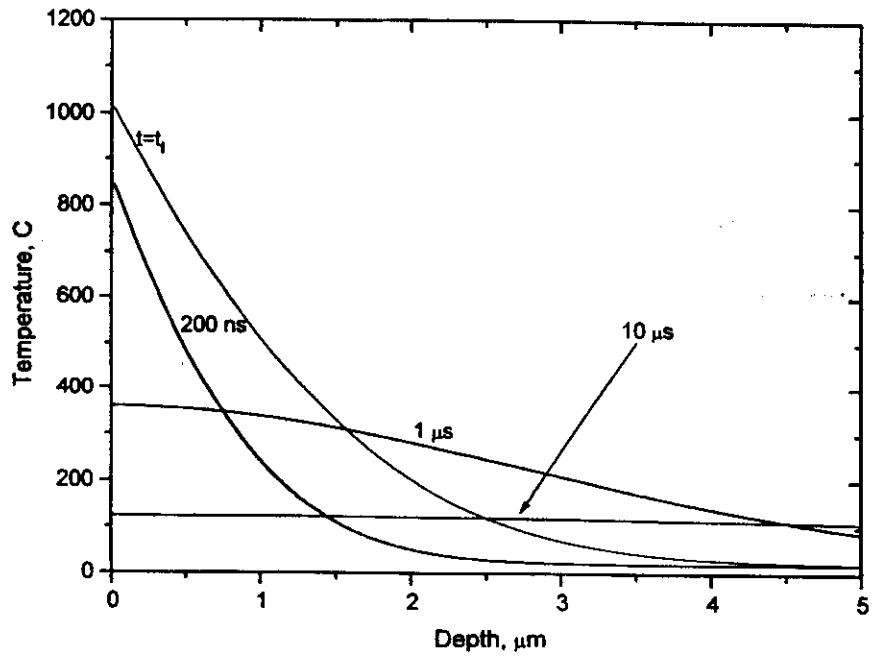

(b)

Figure 3. Thermal evolution of nitrogen implanted stainless steel: (a) $\ell = 80$ mm, $t_r \sim 300$ ns, (b) $\ell \sim 100$ mm, $t_r = 350$ ns.

as radiation and convection. In addition, and with the purpose of ion beam flux and fluence quantification, the α parameter in equation (2) was adjusted to fit with the energy requirements to reach the melting temperature at the surface level of the stainless steel, for the particular experimental situation in which the surface of a sample of such material was observed as being slightly damaged due to an incipient melting process.

In spite of the extremely short duration of the process of implantation and the small size of the affected region, which makes the simultaneous experimental measurements and time survey of such temperature profiles to corroborate the numerical calculations impossible, good agreement between calculations and the reported experimental implantation results was found. After the fitting (to fix the α parameter) data for one specific experimental situation (ion species, implantation distance and implanted material), no contradiction was found with the results for other experimental situations. The extremely high surface damage observed in titanium nitrogen implanted samples, the variation of the degree of surface damage in stainless steel samples located at different distances from the ion source, and the lack of damage in copper samples are examples of this.

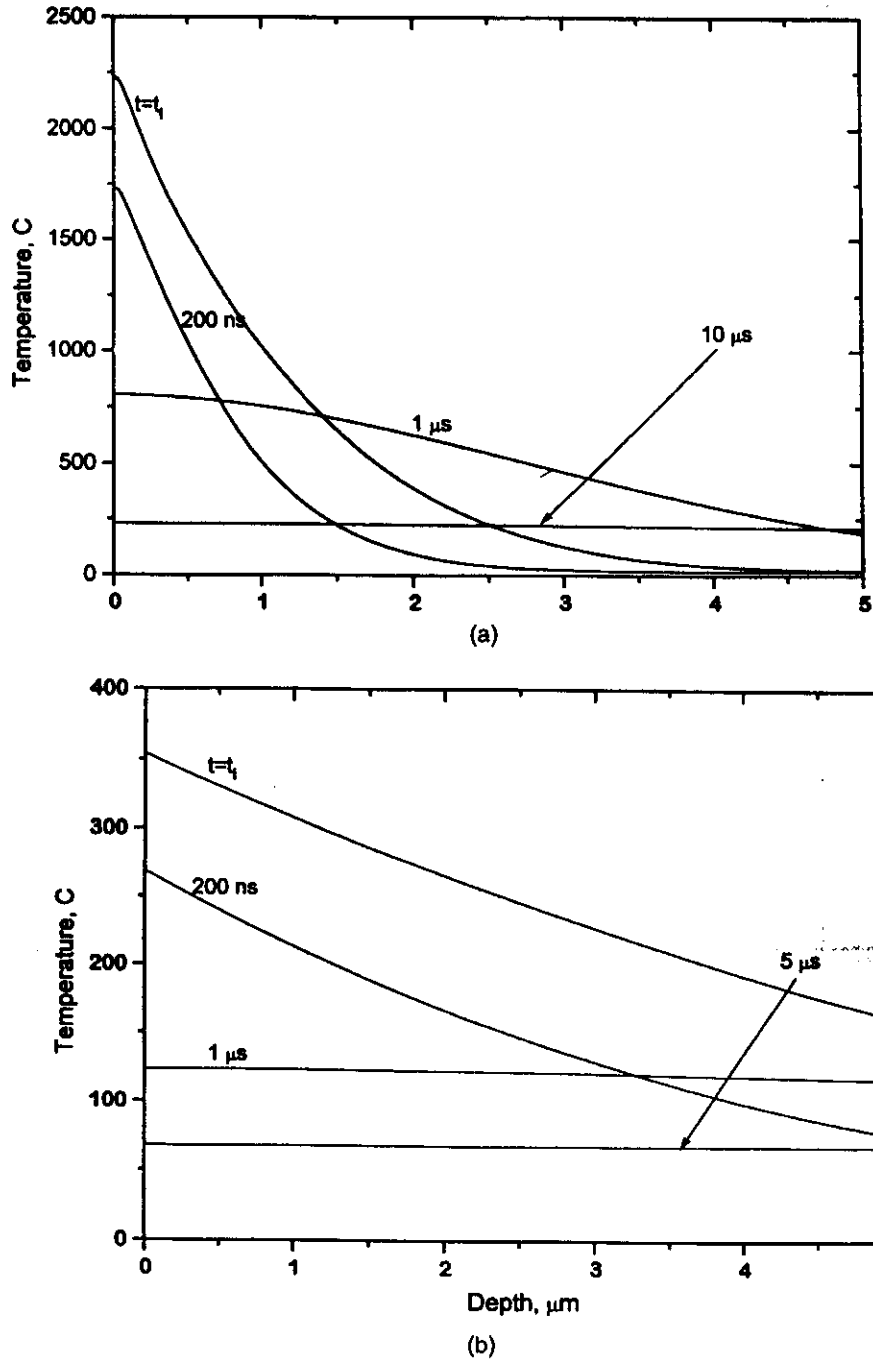

Figure 4. Thermal evolution of nitrogen implanted titanium (part a) and copper (part b), ℓ = 100 mm, $t_r \sim 350$ ns.

More qualitatively, the residual deformation analysis [16] showed the existence of a strong fast heating as an explanation of the induced concave surface deformation after pulsed ion beam implantation. Specifically, the maximum deformation reported in the reference for stainless steel, which is of ~ 3 μm, can be explained through the temperature evolution profile results obtained in this work. These profiles show that temperatures can be high enough, some time during the implantation process, down to depths ~ 3 μm, inducing an excess at the fluence limit of the material due to thermal stresses.

Under our calculation conditions, the results showed that a strong thermal shock takes place during the ion beam incidence consisting of a fast heating and strong temperature gradients (which in the stainless steel case can be of ~ 10 K ns^{-1} and ~ 700 K μm^{-1} respectively), and reaching peak temperatures which can produce melting and even vaporization of thin surface layers of material. This strong heating process has a depth of incidence of several micrometers into the material, and it is followed by a fast cooling down (through a thermal conduction process to the sample bulk) which leads to its thermal relaxation within a few microseconds.

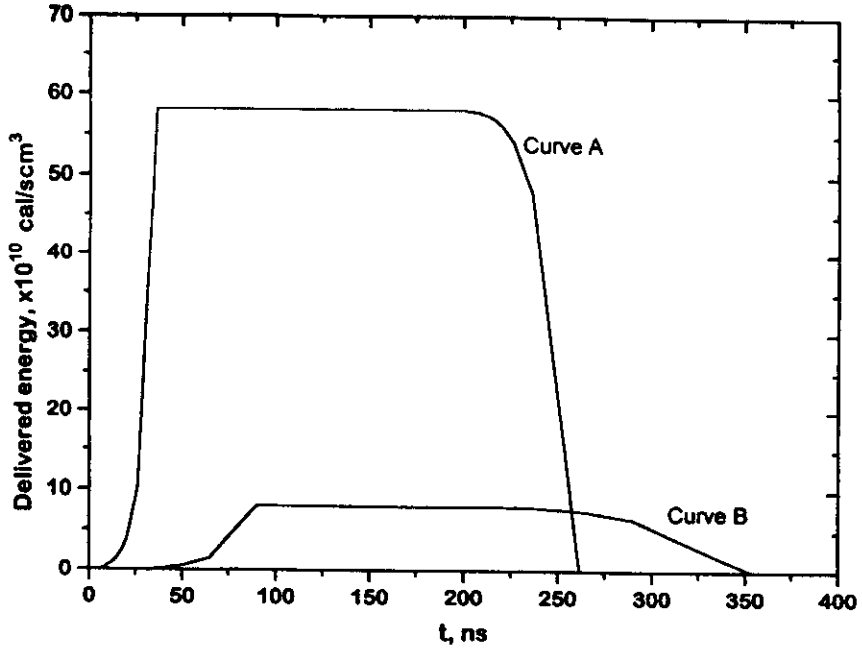

Figure 5. Energy delivered to the target as a function of time during the IP for nitrogen implanted stainless steel for (A) ℓ = 40 mm and (B) ℓ = 100 mm.

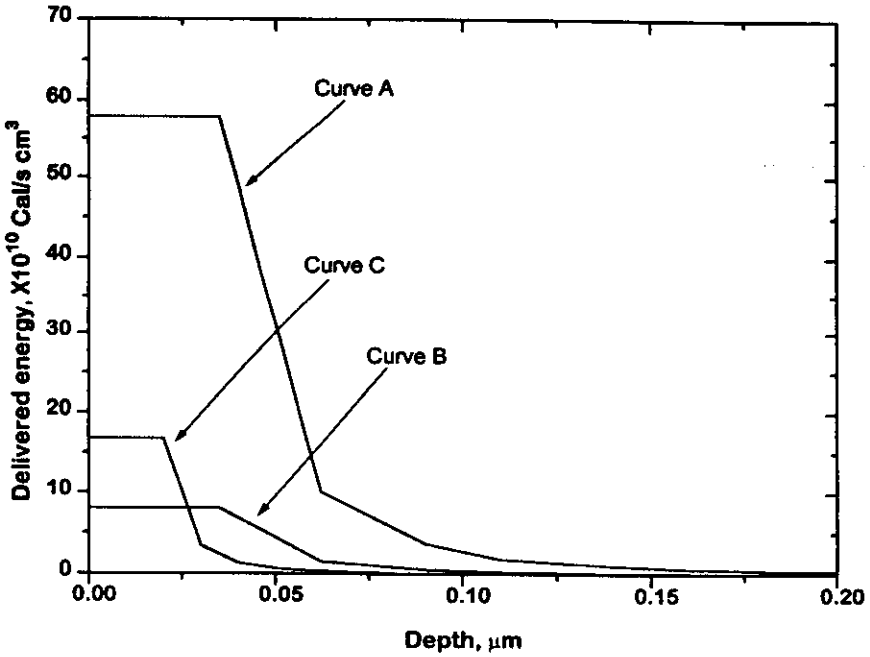

Figure 6. Energy delivered to the target as a function of depth in stainless steel for (A) nitrogen, ℓ = 40 mm; (B) nitrogen, ℓ = 100 mm, and (C) argon, ℓ = 100 mm.

Fast heating and cooling processes of similar characteristics were also observed using numerical calculations for targets irradiated with monoenergetic pulsed ion and electron beams and high power laser beams [17–21].

In spite of the interesting results in the tribological improvement of different materials under this type of surface treatment, the physical process sustained is only partially understood. More work has to be done for a full comprehension of the mechanisms involved in surface layer modifications through the combined effect of the ion implantation and the thermal shock associated with the pulsed nature of the beams.

Acknowledgments

This work was performed under CONICET grant BID-PID No 222, International Atomic Energy Agency research contract 6477/RB, and International Centre for Theoretical Physics TWAS research grant MP 90-090.

References

[1] Mather J W 1965 *Phys. Cont. Nucl. Res. IAEA, Culham* **C-21/80** 2
[2] Filipov N V, Filipova T I and Vigmogradov V P 1962 *Nucl. Fusion Suppl.* **2** 577
[3] Feugeas J, Llonch E, de González C O and Galambos G 1988 *J. Appl. Phys.* **64** 2648
[4] Feugeas J, de González C O, Nieto M, Peyronel M F and Sánchez G 1990 *Brazilian J. Vac. Appl.* **9** 118
[5] Feugeas J, de González C O and Sánchez G 1994 *Radiat. Eff. Defects Solids* **128** 267
[6] Kondoh Y, Shimoda K and Hirano K 1981 *Japan. J. Appl. Phys.* **20** 2648
[7] Stygar W, Gerdin G, Venneri F and Mandrekas J 1982 *Nucl. Fusion* **22** 1161
[8] Jäger U and Herold H 1987 *Nucl. Fusion* **27** 407
[9] Ziegler J F, Biersack J P and Littmark U 1985 *The Stopping and Ranges of Ions in Matter* ed J F Ziegler (New York: Pergamon)
[10] Kern D 1980 *Procesos de Termotransferencia* (Mexico City, Mexico: CEAC)
[11] Feugeas J, Sánchez G, Grigioni G and de González C O 1992 *Proc. Mater. Res. Soc. Symp.: Materials Modification by Energetic Atoms and Ions* ed K Grabowski *et al* (San Francisco: Materials Research Society) 389
[12] Lambri O A, Sánchez G, Feugeas J and Povolo F 1996 *J. Mater. Sci. Lett.* **15** 672–4
[13] Lambri O A, Sánchez G, Feugeas J and Povolo F 1995 *Surf. Coatings Technol.* **70** 191
[14] Sánchez G 1990 *Surface of Steels under Pulsed Ion Implantation–Instituto de Física Rosario Internal Report*
[15] Weast R C 1980 *Handbook of Chemistry and Physics* (Boca Raton, FL: Chemical Rubber Company)
[16] Brühl S P, Sánchez G, Storti M, Cardona A, Feugeas J N and Kaufmann G H 1995 *J. Phys. D: Appl. Phys.* **28** 1655
[17] Garrido C, León B and Peréz-Amor M 1991 *J. Appl. Phys.* **69** 1133
[18] Kou S 1982 *Metall. Trans.* A **13** 363
[19] Third C E, Weinberg F and Young L 1991 *J. Appl. Phys.* **69** 8037
[20] Mazumder J and Steen W M 1980 *J. Appl. Phys.* **51** 941
[21] Curzon A E 1989 *J. Phys. D: Appl. Phys.* **22** 295

MATERIALS RESEARCH SOCIETY SYMPOSIUM PROCEEDINGS VOLUME 354

Beam-Solid Interactions for Materials Synthesis and Characterization

Symposium held November 28-December 2, 1994, Boston, Massachusetts, U.S.A.

EDITORS:

Dale C. Jacobson
AT&T Bell Laboratories
Murray Hill, New Jersey, U.S.A.

David E. Luzzi
University of Pennsylvania
Philadelphia, Pennsylvania, U.S.A.

Tony F. Heinz
Columbia University
New York, New York, U.S.A.

Masaya Iwaki
The Institute of Physical and Chemical Research
Wako, Saitama, Japan

MRS
MATERIALS RESEARCH SOCIETY
Pittsburgh, Pennsylvania

ELASTICITY SHEAR MODULUS MODIFICATION BY IMPULSIVE ION IMPLANTATION

JORGE N. FEUGEAS*, O.A. LAMBRI*, G. GRIGIONI*, G. SANCHEZ* AND F. POVOLO**

*Instituto de Física Rosario (CONICET-UNR), Bv. 27 de Febrero 210 Bis., 2000 Rosario, Argentina.

**Comisión Nacional de Energía Atómica, Av. del Libertador 8250, Buenos Aires, Argentina.

ABSTRACT

Samples of pure copper were argon ion irradiated using a Plasma Gun operated in the detonation mode. The irradiated copper samples were studied by means of the Mechanical Dynamical Spectroscopy technique.

The results show an anomalous behavior in the Elasticity Shear Modulus, consisting in an abrupt jump in its value at ~840K, repeated in the running up as well as in the running down part of the temperature cycling. A Damping Peak at that temperature was also observed.

INTRODUCTION

The composition of the surface layers and the tribological properties of different types of steels and titanium, proved to be strongly modified by pulsed ion beam implantation with nitrogen.

Different types of iron nitridings were developed driving to a relevant reduction in the wear rate and friction force in AISI 304 Stainless Steel [1] and M2 High Speed Steel [2].

An important improvement in the microhardness of pure titanium with TiN_x development with a stoichiometry ($0.8 < x < 1.1$) corresponding to hard compounds was also observed after pulsed nitrogen implantation [3].

Nevertheless, most of the results must be attributed not only to a single ion implantation process but to the combined effect of an ion implantation process plus a strong thermal effect due to the short time duration of the beam pulses [3].

In this paper the effect of pulsed argon irradiation of pure copper is analyzed using the Mechanical Dynamical Spectroscopy method (MDS).

The MDS is a non microscopic technique employed for studying the kinetics of defects in metals and their interactions. This very sensitive technique, permits simultaneous study of the dissipative phenomena which are being activated (damping processes) and the elastic modulus solicited in function of the temperature.

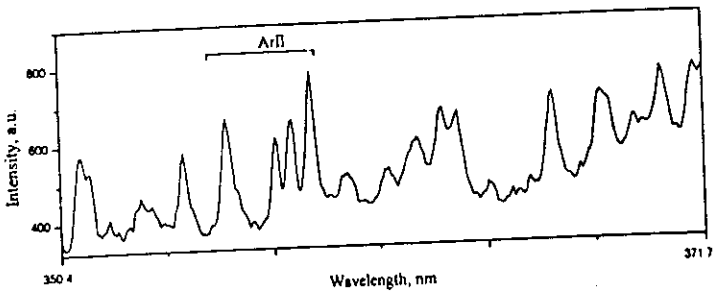

Figure 1: Wide spectrum of the emission light taken with an OMA III.

EXPERIMENTAL PROCEDURE

The pulsed argon irradiation was performed with a Plasma Gun operated in the detonation mode (Plasma Focus)[4,5]. This device accelerates pulsed ion beams with a fluence f= 10^{13} cm^{-2}, with a pulse time duration Δt between 300 and 500ns, and with an energy spectral law $dN/dE \sim E^{-3.4}$ (20keV<E<500keV) [6], being N the number of ions with energy E. Higher fluences F can be obtained by the accumulation of a predetermined number n of single pulses with fluences f (F=n·f).

The sample surface also receives the influence of a highly activated plasma cloud (of Ar in this case) which arrives immediately after the ion beam in each shot. This plasma cloud reaches the target when it is still at high temperature. In Figure 1, a visible light spectrum of the plasma in the implantation region can be seen, shown high intensity peaks of ArII (singly ionized argon emission lines).

The samples were made of electrolytic high purity polycrystalline copper, as strips of 30mm x 4.5mm x 0.3mm, all cut in the same rolling direction. The internal stresses were released, previous Ar irradiation, heating the samples up to 1073K, under vacuum (10^{-4} Torr), during three different times: 1 hour (samples type S1), 5 hours (samples type S5), and 15 hours (samples type S15).

The MDS measurements were carried out with a torsion pendulum of the inverted type with the continuous variable moment of inertia in remote way under high vacuum [7], belonging to IFIR. The MDS measurements were performed under high vacuum in the free decay method through a data acquisition system, with the running up temperature having a velocity of 0.5K/min in the range of 300K-1130K. The natural frequency at room temperature was $\sim 0.6 s^{-1}$. The maximum samples' strain was 4×10^{-5}.

All the samples were implanted with 100 pulses with Δt=500ns and f=10^{13} cm^{-2}, giving a total fluence F=10^{15} cm^{-2}.

RESULTS

In Figure 2, the Damping Spectrum (DS) and the Elasticity Shear Modulus (ESM) of an unimplanted S1 type Copper sample are shown. The damping spectrum is in agreement with the already known in which two peaks at 534K and 650K [8] appear, while the ESM shows a correct thermodynamic behavior with the temperature.

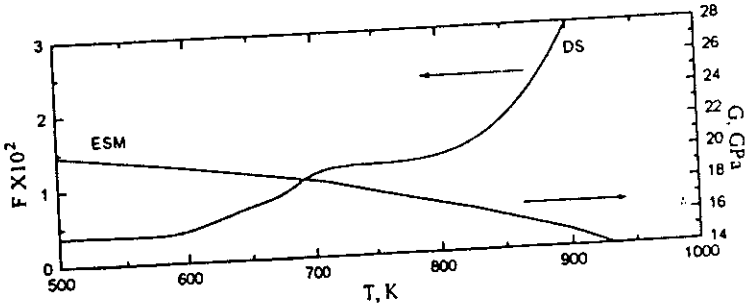

Figure 2: Dumping Peaks and Elastic Shear Modulus variation with temperature for unirradiated Copper sample type S1.

In Figure 3, both DS and ESM for Ar irradiated S1 type copper samples are presented, corresponding to tests performed within 48 hours after irradiation. In the damping spectrum, a little relaxation peak appears at 840K, the temperature at which an anomalous behavior in the ESM temperature cycling is also observed. Effectively, in the same figure and in the running up part of the thermal cycling, a sharp jump of ~20% to higher ESM values was observed at a temperature of ~850K. This jump was repeated (~22% in this case) in the running down part of the thermal cycling, but at a slightly lower temperature value (~820K).

Nevertheless, the same sample tested one week later did not show either the jump in the ESM, or the damping peak in the DS.

In Figure 4, the DS and ESM results of the Ar irradiated S5 Type copper samples are shown. They correspond to tests performed within the first 48 hours after irradiation, and the jump (~20% in this case) at ~840K in the ESM was also present.

For S15 Type Ar irradiated samples a similar behavior was also found, with a jump in the ESM of ~5% at 840K (Figure 5). In both cases (S5 and S15 Type samples) the ESM jumps and the damping peaks disappear completely in tests performed a week after the

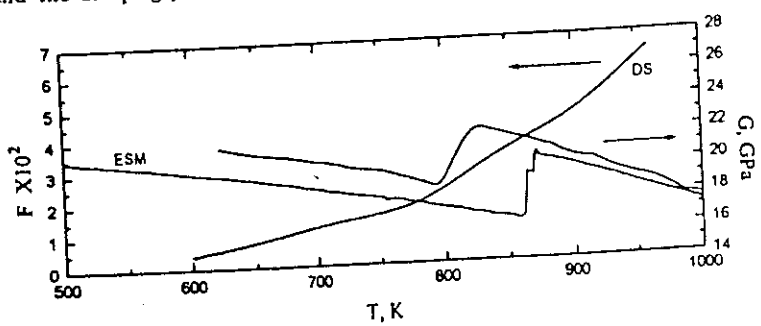

Figure 3: Dumping Peaks and Elastic Shear Modulus variation with temperature for Ar irradiated Copper sample type S1.

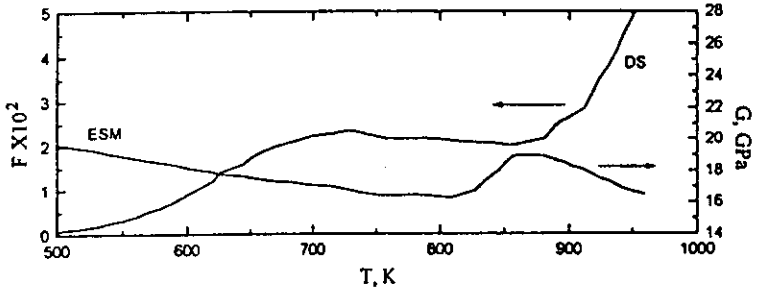

Figure 4: Dumping Peaks and Elastic Shear Modulus variation with temperature for Ar irradiated Copper sample type S5.

irradiation process.

DISCUSSION AND CONCLUSIONS

The results of Ar irradiation showed the modification of the copper surface layer deep enough to modify the Elastic Shear Modulus, consisting in an increasing in the whole thermal cycle, plus an anomalous jump at ~840K. These jumps are only present within the first two days after irradiation, disappearing completely after a week. In addition, a dependence on the magnitude of the ESM jumps with the duration of the thermal treatment was found, being larger for shorter thermal treatment times. The analysis of the damping peak in the MDS relaxation tests showed also a peak at ~840K, which disappears after a week of irradiation.

A similar anomalous effect in the ESM was reported by B. Beyer et al [9] in strongly deformed samples. In that work, ESM jumps were found but only in the temperature running up part of the thermal cycle. Also, damping peaks were observed in the DS analysis, peaks which decrease in amplitude with successive DS temperature cycling.

In our case, to find an explanation for this anomalous behavior, two principal factors

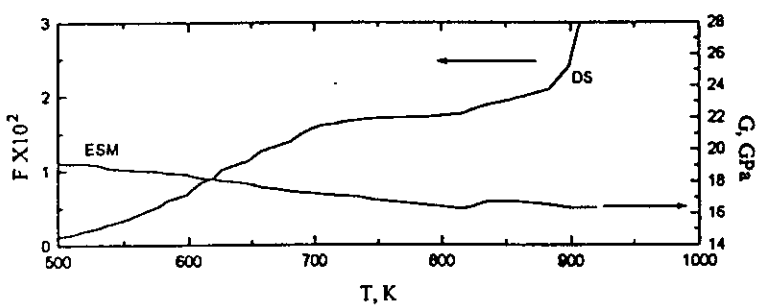

Figure 5: Dumping Peaks and Elastic Shear Modulus variation with temperature for Ar irradiated Copper sample type S15

have to be taken into account: a) the strong thermal effect induced in the surface layers due to the short duration of the Ar ion beam pulses (which generates gradients of temperature $\geq$1000K/μm, peak surface temperatures of ~800K, with heating speeds of ~10K/ns) [3]; and b) the very large radiation damage produced by Ar irradiation, according to TRIM calculations [10].

The first effect can reach depths >2μm, whereas the second, which is related with the Ar ion range in Cu, will not go deeper than 0.4μm.

The fact that the anomalous effect occurs for a temperature close to the recrystallization of Cu, suggests the idea of a mechanism based on the growth of new oriented crystal grains, or a change in texture, due to the previously mentioned physical perturbation in the surface layers. To this effect, the distortion induced in the grain boundaries and the dislocation structures at significant depths in the sample, must also be conditioned.Nevertheless, all these arguments can explain the ESM first jump (in the running up part of the thermal cycle), i.e. associated with a recrystallization process, but not as well the inverse jump which takes place during the cooling down part of the cycle.

Taking into account the thermal effect and the residual stresses and deformations induced in the surface layers [11] a process of amorphization can also be considered.

The fact that no equivalent effects were observed when nitrogen ions were used, can be associated with the smaller size nitrogen ion [12] which perturbs the Cu net in minor degree than argon ions. More work has to be done to allow full explanation of this anomalous phenomenon.

ACKNOWLEDGMENTS

We are grateful to A. Muñoz for his invaluable collaboration in the laboratory work. Work partially supported by CONICET (Argentina), Grant PI-BID No. 222/92; IAEA (Austria), Research Contract No. RC/6477/R1/RB; and Antorchas Foundation.

REFERENCES

[1] J. Feugeas, E. Llonch, C. O. de Gonzalez and G. Galambos, J. Appl. Phys. 64 (5), 2648 (1988).

[2] J. Feugeas, C.O. de Gonzalez, M.F. Peyronel and G. Sanchez. Brasilian of Vacuum Applications, 9 (2), 118 (1990).

[3] J. Feugeas, G. Sanchez, G. Grigioni and C.O. de Gonzalez. in Materials Modification by Energetic Atoms and Ions, edited by K.S.Grabowski, S.A Barnett, S.M.Rossnagel and K.Wasa (Mat. Res. Soc. Proc. 268, San Francisco, CA, 1992) pp 389

[4] J.W. Mather. Plasma Physics and Cont. Nucl. Research, IAEA, Culham, C-21/80, 2 (1965).

[5] W. Bostick, V. Nardi and W. Prior. Annals of the New York Academy of Sciences, 251, 2 (1975).

[6] W.Stygar, G. Gerdin and F. Venneri, Nucl. Fus. 22 (9), 1161 (1982).

[7] F. Povolo, B. Molinas and O. Lambri, Il Nuovo Cimento 14D, (1992) N2.

[8] G.M. Ashmarin, M.Y. Golubev, N.Y. Naumova and A.V. Shlismonva. Proc. of Internal Friction and Attenuation in Solids, International Academic Publishers, Beijin, China 133

(1990).
[9] B. Beyer, E.M. Herbst and J. Wieting, Mat. Science Forum 119-121, 385 (1993).
[10] J.F. Ziegler, J.P. Biersack and U. Littmark. The Stopping and Range of Ions in Solids (Pergamon Press, New York, 1985).
[11] J. Feugeas, S. Brühl, G. Sanchez and G. Kaufmann. MRS Fall Meeting, Boston, Massachussetts, U. S. A., 28 November-2 December 1994.
[12] O.A. Lambri, G. Sanchez, J. Feugeas and F. Povolo, Surface and Coating Technology (in press).

MICROSTRUCTURAL EVOLUTION DURING ION BEAM ASSISTED DEPOSITION

GRAHAM K. HUBLER, Naval Research Laboratory, Code 6670, Washington, DC 20375

ABSTRACT

The advantages of energetic deposition are low temperature processing, oriented or single crystal films, high phase purity, high density and good adhesion to substrates. The time and spatial scales over which the atoms arrange themselves on a surface are not easy accessed experimentally. Therefore, these advantages are customarily verified by ex-situ examination of films after deposition is complete, which gives little information on atomic scale processes that lead to the listed advantages. The addition of energy to the deposition flux effects surface processes that are otherwise only controllable by changing the substrate temperature. Thus, understanding the mechanisms by which energetic atoms alter surface processes in analogy with thermal effects is of paramount interest for optimization of the deposition parameters. This review summarizes the state of knowledge on the effects of energetic ions on film formation. For high quality, defect free films, the energy must be controlled in the energy region of 5 eV to 30 eV. Below about 5 eV, the energy is ineffective for changing the physical processes, and above about 30 eV, defects are added to the film by displacement damage that cannot anneal out due to low temperature of the deposition. Models for the composition and chemistry of films energetically deposited are progressing well, while models for prediction of the phases that form are almost nonexistent. Molecular dynamics provide the best information, but only a handful of cases have been simulated.

INTRODUCTION

Energetic deposition techniques, including ion beam assisted deposition (IBAD), are playing an increasing role in the processing of advanced electronic and photonic materials and protective coatings. There are fundamental physical processes common to energetic all deposition methods. The mechanisms by which these physical processes lead to phase formation are under intense investigation.[1,2] New fundamental studies on the effects of energetic atoms on surfaces by molecular dynamics simulations and Monte-Carlo simulations are contributing to the understanding of thin film growth as well as experiments that reveal relationships between deposition variables and the phases that form. This paper covers the above topics by first establishing the "ideal" conditions for deposition of a film, and then indicating how energetic deposition attempts to approximate these conditions.

THE VACUUM DEPOSITION PROCESS

To fabricate a thin film by vacuum deposition, atomic species are produced in vapor form and condensed onto a substrate. The process of film formation is completed in picoseconds to nanoseconds. There are few in situ techniques for observation of the condensation process on these time scales and with atomic resolution that allow observation of film formation. The films are usually examined in situ or ex situ after a specified film thickness is deposited. Control over this process is exercised by only three first order vapor parameters and one first order substrate parameter.[3] In this context a first-order parameter is a variable that we can control to influence the outcome of the deposition. The vapor parameters are the absolute arrival rates of the film atoms, R_i, where i can be 1 to 6 or more, the chamber pressure, P, and the energy of the deposition flux, E. The substrate parameter is the substrate temperature, T. Vacuum deposition techniques differ primarily in the manner in which the deposition flux is generated and, therefore, differ in how each one controls R_i, P and E. The substrate temperature, T, is the primary factor that determines the crystalline phase of the deposited film. Other substrate parameters such as the crystallinity,

Mat. Res. Soc. Symp. Proc. Vol. 354 © 1995 Materials Research Society

MATERIALS RESEARCH SOCIETY SYMPOSIUM PROCEEDINGS VOLUME 354

Beam-Solid Interactions for Materials Synthesis and Characterization

Symposium held November 28-December 2, 1994, Boston, Massachusetts, U.S.A.

EDITORS:

Dale C. Jacobson
AT&T Bell Laboratories
Murray Hill, New Jersey, U.S.A.

David E. Luzzi
University of Pennsylvania
Philadelphia, Pennsylvania, U.S.A.

Tony F. Heinz
Columbia University
New York, New York, U.S.A.

Masaya Iwaki
The Institute of Physical and Chemical Research
Wako, Saitama, Japan

MRS
MATERIALS RESEARCH SOCIETY
Pittsburgh, Pennsylvania

RESIDUAL DEFORMATIONS INDUCED BY THE THERMAL SHOCK DURING PULSED ION IMPLANTATION

JORGE N. FEUGEAS, S. P. BRÜHL, G. SANCHEZ AND G. H. KAUFMANN
Instituto de Física Rosario (CONICET-UNR),
Bv. 27 de Febrero 210 bis, 2000 Rosario, Argentina

ABSTRACT

Samples of AISI 316 Stainless Steel were nitrogen and argon ion implanted with pulsed beams generated with a Plasma Gun operated in the detonation mode. The residual deformations induced by the beams were studied by double exposure (before and after implantation) holographic interferometry.

The results showed residual deformations corresponding to a concave situation, with the total value depending on the number of single pulses accumulated. A saturation in the deformation is observed when the number of pulses is ≥ 20. A model of the process of pulsed irradiation (based on the strong thermal effect due to the short duration of pulses) and the state of stresses induced in the surface layers is presented.

INTRODUCTION

The surface treatment of materials by pulsed ion implantation, is a technique which combines a pure implantation process [1] with a thermal process due to the thermal shock associated with the short duration of the beam pulses [2], both effects being responsible for the composition, structure and properties modifications of the surface layers.

Recent results in the measurement of residual stresses, induced under pulsed ion implantation in steel samples, showed their modification from a compressive to a tensile state with an affected layer of $\sim$ 3 μm in depth [3]. In addition, measurements of residual deformations using the holographic interferometry technique, showed that the impulsive ion implantation process provokes a concave deformation [4].

In this work new results on residual deformations measurements are presented, with an analysis and a model on the thermal mechanism that explain this effect.

EXPERIMENTAL

Samples of AISI 316 Stainles Steel consisting in plates of 68 x 68 x 4 mm^3, stress relieved by a conventional heat treatment under vacuum, were nitrogen and argon ion implanted under different conditions in a 14 mm diameter area (by covering with a hollowed titanium foil) in the central region of the surface.

Mat. Res. Soc. Symp. Proc. Vol. 354 © 1995 Materials Research Society

The ion implanter is a Plasma Gun operated in the detonation mode (Plasma Focus) [4], generating ion beam pulses with a fluence $f = 3 \times 10^{14}\, cm^{-2}$, with an energy spectral law given by $dN/dE \sim E^{-3.4}$ (where N is the number of ions with energy E, valid for 20 $keV < E < 500keV$, and with a pulse time duration $\Delta t = 400\ ns$ [2]. Higher fluences F can be obtained by the accumulation of a predetermined number n of ion beam pulses ($F = nf$). The implanter allows for ion beams shots at a rate of two per minute. The deformations were measured using the holographic interferometry method which consists in a double hologram exposition (using a $\lambda = 0.633\,\mu m$ He-Ne laser light) recorded on a holographic plate (one before and a second after the implantation), and counting the interference lines in the resulting fringe pattern [3]. The diagram of the experimental set-up is presented in figure 1. The normal displacement w can be determined by $w = S\lambda/2$, where $S = 1, 2, 3, ...$ is the order of the bright fringes and λ the laser wave length. The sign of the deformation (concavity or convexity) can be determined by the addition of carrier fringes [6], which in our case were introduced by producing controlled small angle tilts to the sample plates between exposures.

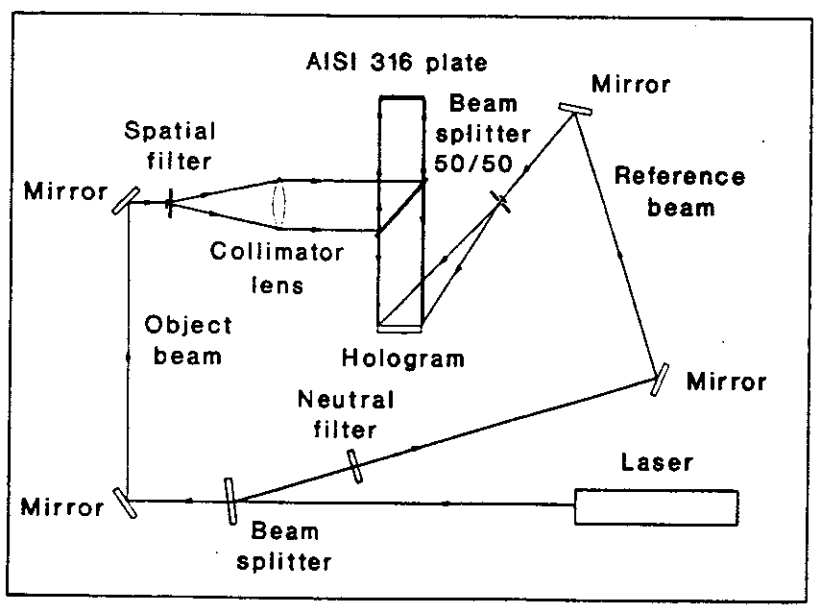

Figure 1: Holographic set-up to measure residual deformations.

EXPERIMENTAL RESULTS

To evaluate the residual deformations accumulation with the number n of single ion beams, different samples were studied in the following way: 1st. holographic exposure, sample implanted with n' ion beam pulses; 2nd. holographic exposure, sample implanted with an extra n'' ion beam pulses. In consequence, the fringe pattern recorded will correspond to the residual deformation induced by the effect of n'' ion beam pulses, on a previously implanted sample with n'. As an example, in figure 2 an interferogram corresponding to a $n' = 0$ and $n'' = 3$ experiment is presented, showing $S = 8$ bright lines, corresponding to a deformation $w = 2,56\ \mu m$. The experiment corresponds to Ar ion beams irradiation.

The results showed that for $n' < 10$, the induced deformation w by $n'' = 3$ ion beam pulses is almost proportional to n'. This effect is strongly reduced for $10 < n' < 20$, being almost negligible for $n' > 20$. This saturation effect was corroborated in tests in which $n' = 50$ and $n'' = 10$, where no fringe patterns were observed.

Taking into account that the lasting time between beam pulses is $\sim$ 0.5 minutes, and that the second holographic exposure takes (sample removal from the implantation chamber plus sample relocation in the holographic setup) approximately 15 minutes, the lasting time of the whole measurement process was $\sim$ 45 minutes.

The experiments did not show significative differences between argon and nitrogen ion beam irradiation.

In reference [3] an equivalent accumulative effect in the residual stresses induced by successive ion beam pulses incidence was already observed, showing in this case a gradual transition from the compressive state in the unimplanted sample, to a tensile state after nitrogen pulsed ion implantation.

Figure 2: Fringe pattern of an holographic interferogram corresponding to an experiment of Ar ion implantation (n'=0 and n''=3).

TEMPERATURE PROFILES

Using the ion beam characteristics (fluence per pulse, energy spectrum, pulse time duration), the thermal properties of the AISI 316 Stainless Steel (heat conduction, heat capacity, temperature of the melting point) and supposing that each ion transfers its kinetic energy uniformly in its track during penetration, stopping at a depth equal to the corresponding range [7]; the temperature profile in depth and its time evolution during the implantation (ion beam pulse time duration) and after (cooling down) were calculated using the finite differences method [8]. In figure 3 the results for nitrogen ion beam (part a-) and argon ion beam (part b-) pulses are presented. The high peak temperatures reached in the surface ($> 1000\ K$), the high heating speed ($\sim\ 3\ K/ns$), the strong gradient of temperature generated under the surface ($\sim\ 1000\ K/\mu m$) and the also high cooling speed, showing the relevance of the thermal effect (thermal shock).

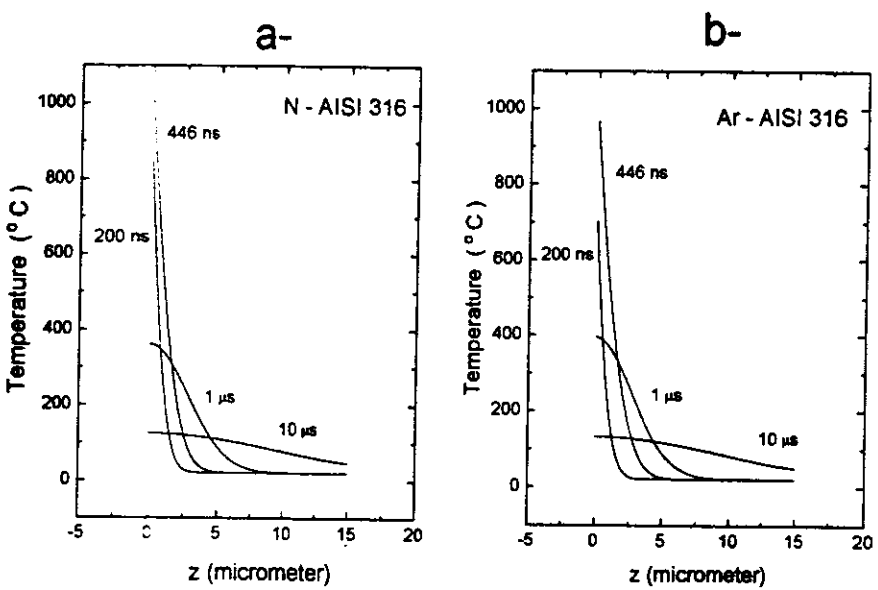

Figure 3: Temperature profile temporal evolution for nitrogen (part a-) and argon (part b-) ion beams.

DISCUSSION AND CONCLUSIONS

The temperature effect on the surface layers is of extremely high importance as can be seen from the results presented in the preceeding section.

Considering both, the tensile state of the induced residual stress and the concavity in the induced residual deformation, an explanation can be found considering exclusively the thermal effect.

During the ion beam pulse incidence, the surface layers are heated up to considerably high temperatures, letting the lower layers and the periphery of the disc area of incident ions to be cooler. On the heated disc, surrounded by the cooler substrate, a state of stresses given by [9] will be developed.

$$\sigma = \frac{Y\,\alpha\,\Delta T}{(1-\nu)} \tag{1}$$

where Y is the Young Modulus, α is the thermal expansion coefficient, ΔT is the temperature increment and ν, the Poisson ratio. When ΔT is high enough, the fluence limit of the material can be reached and surpassed, leading to a plastic deformation. When the implantation ends, this disc begins to cool down, originating a tensile stress which, for samples with relatively small thicknesses, induces a concave deformation.

This qualitative description of the process was used to the modelization and the computation, by numerical simulation [10], of the resiual deformations induced by a single ion beam. Nevertheless, the numerical simulation based on this model, applied to successive ion beam pulses incidence, do not foresee accumulative effects.

When a second ion beam reaches the surface, taking into account that the lasting time between ion beam pulses is $> 30\ s$, it will find the sample at room temperature (as can be seen in the temperature profiles of figure 3.

The symmetric effect predicted by the model (the plastic deformation due to the compressive stress induced during the heating is compensated by a plastic deformation due to tensile stress during the cooling stage), which is the cause of the non accumulative effect, is in fact broken by several factors related with the nature of the process, not considered in the model. These factors are: a- the extremely short duration of the thermal process (high speeds of heating and cooling); b- the difference between the speed of heating ($\sim\ 3\ K/ns$) and the speed of cooling ($\sim\ 1\ K/ns$); c- the cumulative disorder in the crystal due to ion interactions with the lattice atoms; d- the increasing amount of impurities and compounds developed during each ion beam pulse interaction with the sample.

Among these factors, the most probable can be associated to the high velocity of the process (a-) which can avoid the complete plastic deformation of the affected layer, conducting to a partial residual stresses state stabilization, process which will be gradually completed with the following ion beams pulses. The difference between the heating and cooling ve-

locities can also play a role giving more time to the recuperation than to the induction of compressive states, difference which will also be attenuated with the following ion beams.

Nevertheless, all these arguments are speculations, and more work has to be done introducing modifications in the model to allow the inclusion of those considerations.

ACKNOWLEDGMENTS

We are grateful to A. Muñoz for his invaluable collaboration in the laboratory work. This work was partially supported by CONICET (Argentina), Grant PID-BID No. 222/92; IAEA (Austria), Research Contract No. RC/6477/R1/RB.

REFERENCES

[1] G. Dearnaley, Surf. Eng., 7, 127 (1991).

[2] J. Feugeas, G. Sanchez, G. Grigioni and C. O. de González. in Materials Modification by Energetic Atoms and Ions, edited by K. S. Grabowski, S. A. Barnett, S. M. Rossnagel and K. Wasa (Mat. Res. Soc. Proc. 268, San Francisco, CA, 1992) pp. 389

[3] A. A. Pochettino. J. Feugeas, M. Ortiz and G. Sánchez in Residual Stresses III, edited by H. Fujiwara, T. Abe and K. Tanaka (Elsevier Applied Science, 1992), pp. 833.

[4] G. H. Kaufmann. S. P. Brühl and J. N. Feugeas. Surface and Coating Technology (in press).

[5] J. W. Mather. Plasma Physics and Cont. Nucl. Research, IAEA, Culham, C-21/80, Vol. 2 (1965).

[6] D. R. Matthys, T. D. Dudderar and J. A. Gilbert. Exp. Mech., 28, 86 (1988).

[7] J. F. Ziegler, J. P. Biersack and U. Littmark. The Stopping and Range of Ions in Solids (Pergamon Press. New York, 1985).

[8] G. Sánchez. G. Grigioni and J. Feugeas, Surface and Coating Technology (in press).

[9] S. Timoshenko and J. M. Goodier, 2nd. ed. Theory of Elasticity (McGraw-Hill, New York, 1951).

[10] S. P. Brühl, G. Sánchez, M. Storti, A. Cardona, J. N. Feugeas and G. H. Kaufmann (submitted to Journal of Physics D: Applied Physics).

J. Phys. D: Appl. Phys. 28 (1995) 1655–1660. Printed in the UK

Generation of residual deformations by pulsed ion implantation

S P Brühl†, G Sánchez†, M Storti‡, A Cardona‡, J N Feugeas† and G H Kaufmann†

† Instituto de Física Rosario, Boulevard 27 de Febrero 210 bis, 2000 Rosario, Argentina
‡ Instituto de Desarrollo Tecnólogico para la Industria Química, Güemes 3450, 3000 Santa Fe, Argentina

Received 19 October 1994, in final form 23 March 1995

Abstract. The generation of residual deformations on AISI 316 stainless steel submitted to pulsed ion implantation by means of a plasma focus device was investigated. It is shown that the residual deformation can be attributed to thermal stresses induced in the target by the strong and fast heating process due to the accelerated ions. A numerical simulation is presented as an attempt to explain the generation of these deformations. The model is based on the computation of the temperature distribution in the implanted zone and the calculation of the induced thermal stresses. The mechanical response of the whole specimen is then evaluated using the finite-element method. Numerical results are compared with those measured by means of a holographic method and reasonable agreement is obtained.

1. Introduction

Ion beam processing is a well-established technique by which the composition, structure and properties of the near surface of many materials can be modified. The main advantage of this process is the ability of introducing any element into any solid independently of thermodynamic constraints. There are many results in the literature showing important improvements in metal surface hardening and tribological properties [1].

The accelerators commonly used in ion implantation emit monoenergetic pulsed or continuous ion beams. Feugeas *et al* [2] recently reported the use of a plasma focus device as an ion implanter which provides pulsed ion beams with a continuous energy spectrum. Using this pulsed implanter, the ability of nitrogen ion implantation to improve tribological properties such as resistance to wear and friction in tool and austenitic steels has been proved [3–5].

The interpretation of the surface changes introduced by the implantation with a plasma focus device requires the combination of two aspects of the ion–solid interaction phenomena. The first aspect is the superposition of many single and isolated ion–target interaction processes, such as inelastic collisions with electrons or elastic ones with nuclei of the material. The second aspect is the collective effects generated by the high ion flux which produces in a reduced volume a strong and fast heating process with an important influence on the final ion distribution, concentration and chemical bonding [6]. These mechanisms combined with the plasma environment produce an important thermal effect on the target which is added to the pure implantation process. The structural modifications introduced to the implanted region induce irreversible deformations in the material and consequently generate residual stresses. Although these residual stresses were measured in steel specimens by an x-ray diffraction method [7], this technique does not offer a global macroscopic view of the residual deformation field.

Kaufmann *et al* [8] recently presented a holographic method which allows the measurement of residual deformations over the whole surface of an implanted specimen. Holographic interferometry is a widely applied technique for the full-field evaluation of mechanical surface deformations in different materials and has the ability to measure small displacements to wavelength accuracy. Measurements of residual deformations performed in nitrogen-implanted stainless steel specimens showed the generation of residual deformations of some importance and suggested the idea of developing a model to explain the generation of these deformations. This model is based on the computation of temperatures in the specimen due to the surface heating, work which had already been presented by some of the authors [9].

This paper reports a numerical simulation of the generation of residual deformations induced by the plasma focus implanter BD-I developed by the Plasma Physics Group of the Instituto de Física Rosario. This simulation is a first attempt to explain the mechanism

0022-3727/95/081655+06$19.50

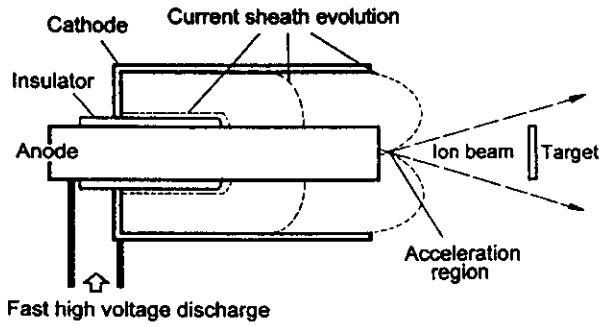

Figure 1. The BD-I plasma focus device.

of fast heating and the subsequent creation of stresses which cause the surface residual deformation that is experimentally observed. It is shown that results obtained from the numerical simulation presented here are in reasonable agreement with those experimentally obtained using the mentioned holographic technique.

2. Previous results

Specimens implanted with nitrogen by using the BD-I device were studied by means of the holographic method described in [8]. Using this method, it was shown that ion implantation introduced a deformation field throughout the specimen and not only over the area upon which ions directly impacted. Fringe patterns obtained using the mentioned holographic method were fairly concentric and followed the symmetry of the ion beam. The direction of the deformation induced by the accelerated ions was determined through the introduction of carrier fringes between the two exposures which generate the hologram [10]. It was determined that the effect of the ion implantation was to produce not only a depression over the surface, but also a flexion of the whole specimen.

Experiments performed with argon ions showed the generation of similar fringe patterns to those obtained with nitrogen. These results indicate that the formation of precipitates would not be the main mechanism involved in the generation of the observed residual deformation [7]. It must also be considered that, due to the low doses (about 10^{13} cm^{-2}) used in the argon implantation, argon retention and bubble formation are negligible processes [11]. Therefore, the generation of thermal stresses is a mechanism which can produce residual stresses and residual deformations that are due to the thermal gradients induced by the thermal shock [12] during the ion implantation process with the plasma focus device.

To understand the origin of such thermal effect, a brief description of the plasma focus device BD-I is given below. The device is shown schematically in figure 1.

Basically, a plasma focus device consists of two co-axial cylindrical electrodes, with a pure low-pressure gas filling the inter-electrodic volume. The electrode system, open at one end and closed at the other by a co-axial pyrex pipe glass insulator, is connected to a capacitor bank through a spark-gap switch. In particular, the BD-I system works with a 4 μF capacitor bank charged to a maximum voltage of 25 kV. The energy stored in the capacitors (about 1 kJ) is discharged through the central electrode by closing the switch. The discharge produces a current sheath between the two electrodes, which begins (in the breakdown stage) on the insulator surface as a gliding discharge. By the interaction between the current j in the sheath and the self-induced magnetic field B, a Lorentz force ($F \propto j \times B$) appears on the current sheath, pushing it to the open end of the electrode system. Once at the end, the current sheath collapses, generating a dense plasma column in front of the inner electrode (anode) and on the system axis. If the system is optimized (in terms of its geometry and physical parameters), then in such a plasma column Rayleigh–Taylor instabilities occur, which produce the acceleration of ion beams in the direction shown in figure 1.

For implantation purposes, the target is placed in front of the system at a distance l from the focus, as is shown in figure 1. The ion beam has conic geometry with a solid angle of about 40°. Thus the cross section of the beam at a distance l from the focus is

$$\sigma_l = \pi(l \tan 20°)^2. \tag{1}$$

The ion beam has a continuous energy spectrum for energies between 20 and 500 keV and follows the spectral law [13]

$$\frac{dN}{dE} \propto E^{-3.4} \tag{2}$$

where N is the number of ions with an energy E. The temporal width of the beam can be estimated to be between 250 and 500 ns, depending on the distance l.

The fluence f per pulse can be estimated to be between 10^{13} and 10^{14} ions cm^{-2}, depending on the distance l. Higher fluences F can be obtained by accumulation of a pre-determined number of successive pulses.

Taking into account the short duration of the ion beam, during its interaction with the target, a fast energy release takes place into the material, inducing an also fast increase in the temperature of a thin layer (< 1 μm) in the material near the surface. The described characteristics of such a thermal effect (high temperatures and thermal gradients) make almost impossible any direct measurement of the thermal evolution of the target, basically due to the temporal and spatial high-resolution requirements. In this work, a numerical treatment of the problem is presented in order to evaluate the thermal evolution and its surface effects.

3. Numerical simulation

To investigate numerically the generation of residual deformations due to the thermal effect associated with the pulsed ion implantation process, it was considered that the thermal field is uncoupled from the mechanical

one. Thus, the numerical simulation is divided into two steps: first, the temperature distribution is calculated and second, these results are used as input to evaluate the mechanical response of the specimen and the induced residual deformations.

To be able to compare the numerical results with the experimental measurements reported [10, 14], the boundary conditions were chosen similar to the experimental ones. A circular specimen of 68 mm diameter and 4 mm thickness was analysed. It was assumed that the specimen was implanted on one face over a centred circular area of 14 mm diameter. The origin of the coordinate system was located at the specimen's centre with axes x and y lying over the implanted face. The material chosen was stainless steel AISI 316 and the implantation conditions were one pulse of argon ions with a fluence $f = 7\times10^{13}$ cm^{-2}. Because of the symmetry of the specimen and the ion beam, the problem was considered as an axisymmetric one.

3.1. Evaluation of the temperature distribution

The temperature distribution $T(z, t)$ as a function of depth and time generated by the pulse of accelerated ions was calculated from the one-dimensional heat equation with an external energy source. This calculation was performed by means of the finite-difference method and is reported in [12], so only a brief description is given here.

To simplify the calculations several assumptions were made. As boundary conditions, it was assumed that there were no convection or radiation losses in both edges of the specimen and only the contribution of the ion beam was taken into account for the surface exposed to the beam. Thermal constants and density were used as functions of temperature and radiation damage was neglected. The ion distribution in the beam's cross section was considered uniform. The ion distribution in time was also considered uniform, that is, at any time there are ions with all energies in the interval 20–500 keV. The calculation starts with the target at room temperature and the energy conduction occurs only in the depth direction. In the radial direction the temperature was assumed to be uniform, so there was no radial conduction.

The energy release was assumed uniform along the path of the ion into the target until it stopped. In the heat conduction equation, the external energy source was taken as the energy flux carried by the ion beam. To calculate this term, which depends on the characteristics of the ion beam described before, the energy interval of validity of the spectral law of equation (2) (20–500 keV) was sub-divided into small sub-intervals of amplitude ΔE. For each sub-interval, the number of ions n_j, the mean energy value per ion e_j and the time elapsed during the ions–specimen interaction $\Delta\tau_j$ was found.

The depth at which the ion stops in the specimen, called the range, is a function of the ion mass, the ion energy and the specimen density. To evaluate the range

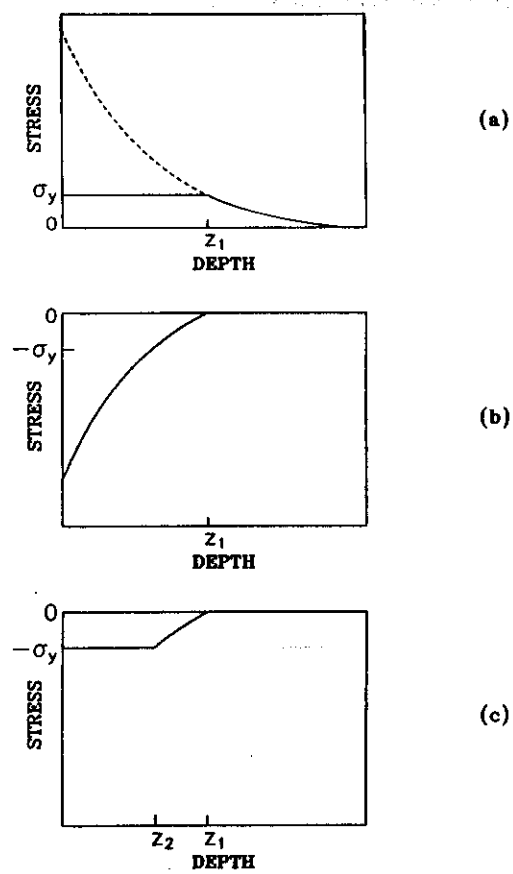

Figure 2. (a) Thermal stresses developed during heating and their relaxation to the yield stress σ_y, (b) addition of the stress distribution generated during cooling and that shown in figure 1(a) and (c) the final stress distribution.

of the ions, the TRIM code was used [15]. For the n_j ions of each energy sub-interval a mean range $\langle R_p\rangle_j$ can be defined as

$$\langle R_p\rangle_j = \tfrac{1}{2}(R_p^{j+1} + R_p^j) \tag{3}$$

where R_p^{j+1} and R_p^j are the ranges of ions with energies E_{j+1} and E_j, respectively, calculated by the TRIM code.

Then, the energy flux $\dot{q}_j$ delivered by the ions of the jth sub-interval into the surface layer was expressed as

$$\dot{q}_j = \frac{n_j e_j}{\Delta\tau_j \langle R_p\rangle_j \sigma_l} \tag{4}$$

where the beam's cross section σ_l is given by equation (1).

The energy delivery into the surface layer was assumed uniform since the ion penetrates into the surface until it stops at its range. Then, a portion of material at a depth D into the specimen will receive energy from those ions with range $\langle R_p\rangle_j \geqslant D$. This can be written as:

$$Q_D = \sum \dot{q}_j \tag{5}$$

where Q_D is the energy delivered at a depth D into the material, $\dot{q}_j$ is given by equation (4) and the summation is extended over those j for which $\langle R_p\rangle_j \geqslant D$. In the finite-difference calculation, the external energy released at each node is obtained from equation (5) [12].

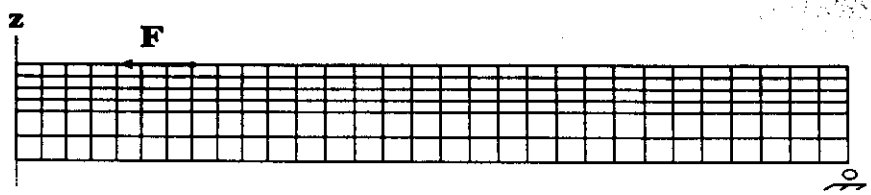

Figure 3. The mesh used in the finite-element simulation.

3.2. Evaluation of the residual deformation

The temperature distribution computed according to the procedure of section 3.1 was used as input for the evaluation of thermal stresses and residual deformations. The developed thermal stresses at a given point depend mainly on the maximum temperature reached at any time at that point. Heat-transfer computations generated the temperature profiles at different times, allowing one to evaluate the evolution of the maximum temperatures as a function of depth. An elastic–plastic material behaviour was assumed.

The temperature penetration depth is of the order of a few micrometres, whereas the implanted zone is 14 mm in diameter. Therefore, only a very thin disc of material at the surface is affected by the thermal expansion. The model assumed that the end faces of the dilated disc are traction-free and that the rest of the specimen reacts only with a radial force distributed all over its external cylindrical surface. For a circular plate with a prescribed distribution of eigenstrains caused by thermal expansion, thermal stresses are easily obtained. Considering an elasto-plastic behaviour of the rest of the specimen, a two-step analysis was made. The first step consisted in the calculation of the residual stresses after heating and cooling, caused by a clamped disc of thickness approximately equal to the penetration depth. In the second step, residual deformations throughout the specimen were computed by making a linear elastic analysis, with loading equal to the radial clamping force computed from the residual stress distribution obtained in the first step.

Stresses for a clamped disc submitted to a uniform temperature increment are [16]

$$\sigma = \frac{Y\alpha\Delta T}{1-\nu} \tag{6}$$

where Y is the Young modulus, α is the thermal expansion coefficient, ΔT is the temperature increment and ν is the Poisson ratio.

Using this model, a simplified nonlinear calculation was performed for the following temperature variation history: (i) heating from room temperature up to the evolution of maximum temperatures and (ii) cooling from the maximum temperature until room temperature had again been reached. During heating, the stress state attains the yield value σ_y. The material yields in the z direction and the radial stress remains equal to σ_y up to a certain depth z_1 (figure 2(a)). When cooling occurs, a thermal traction of equal magnitude but opposite sign to that shown in figure 2(a) is generated as depicted in figure 2(b). Again, in this last distribution some points below a certain depth z_2 exhibited stresses that exceed the yield limit σ_y. The final stress distribution takes the form shown in figure 2(c).

As heating and cooling occur in less than 3 μs the temperature-dependence of the mechanical constants of the material was neglected. Y and ν were considered constant with mean values between 100 and 200 °C for the calculation of the deformations.

The second step of the calculation is the evaluation of residual deformations using the finite-element method. A linear elastic two-dimensional axisymmetric analysis was made, with a mesh consisting of 180 isoparametric eight-node elements (figure 3). Since depth z_1 is very small compared to the specimen width, the effect of the dilated disc on the specimen was simulated by means of nodal forces located on the surface at the boundary of the implanted zone, as is shown in figure 3. This radial force was calculated by integrating the radial stresses in depth and over the perimeter of the implanted zone.

4. Results and discussion

Plots of the temperature distribution as functions of depth z are shown in figure 4 for different times. The plot for time 200 ns corresponds to the heating phase. The time 466 ns is called the implantation time: it is the time at which the last ion of the pulsed beam reaches the specimen. The other plots at 900, 2000, 6000 and 20 000 ns correspond to the cooling phase. It can be observed that a strong thermal gradient of about 900 °C μm^{-1} is developed at the implantation time. A fast cooling down is also noted, with almost complete thermal relaxation after several microseconds.

The radiation of thermal energy is a very complex problem since the emissivity of a material depends on the composition, surface morphology and the method of its production [17, 18]. However, it is possible to make an estimation of the energy lost by this mechanism. Considering the emissivity of polished steel as 0.55 [18], the energy radiated during 2 μs is about 3×10^{-4} J cm^{-2} whereas the energy absorbed by the specimen during the implantation process is about 0.4 J cm^{-2}, confirming that the radiation losses during the cooling stage are negligible. The evolution of the maximum temperatures reached during the process at any point is shown in figure 5.

The final residual stress distribution was calculated by means of the procedures described in section 3.2. Even though figure 2 is out of scale, we can appreciate

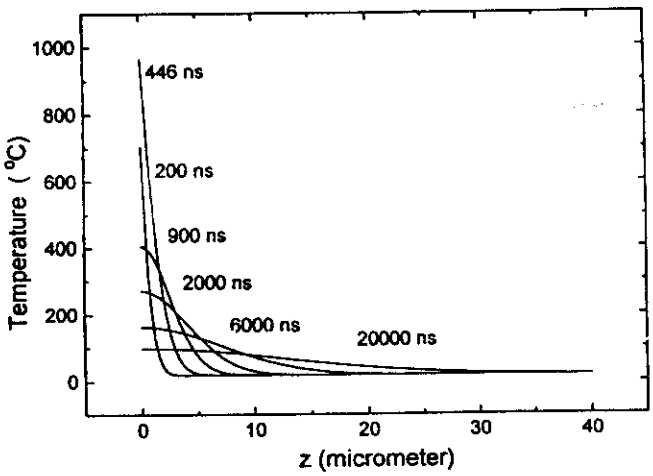

Figure 4. Temperature distribution curves as functions of depth for different times.

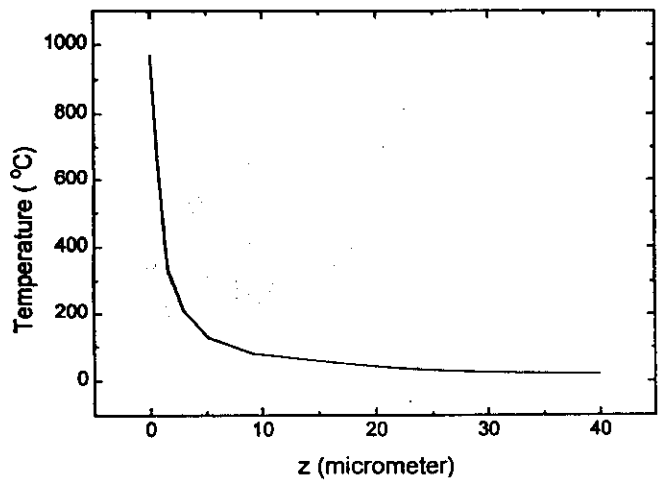

Figure 5. The evolution of maximum temperatures with respect to z.

that the final stress distribution is almost constant inside the implanted zone and is followed by a fast relaxation for increasing depth values.

By integrating the radial stress over the perimeter of the implanted disc and up to the temperature penetration, a total radial force of 87 N was obtained. This force was used in the finite-element simulation to obtain the residual deformation field over the whole specimen.

The out-of-plane displacement w of the surface is plotted in figure 6 as a function of r/a,where r and a are the radial coordinate and the radius of the implanted zone, respectively. For comparison, the mean experimental displacement evaluated with holographic method reported in [14] for a single argon discharge is also plotted in figure 6.

In this simulation, thermal stresses were considered the only mechanism involved in the generation of the residual deformations. Other mechanisms such as production of defects or dislocations were not taken into account. It must be considered that, according to the spectral law described by equation (2), the mean energy per ion in the implantation process is about 35 keV. Ions of this energy produce mostly defects in a layer about

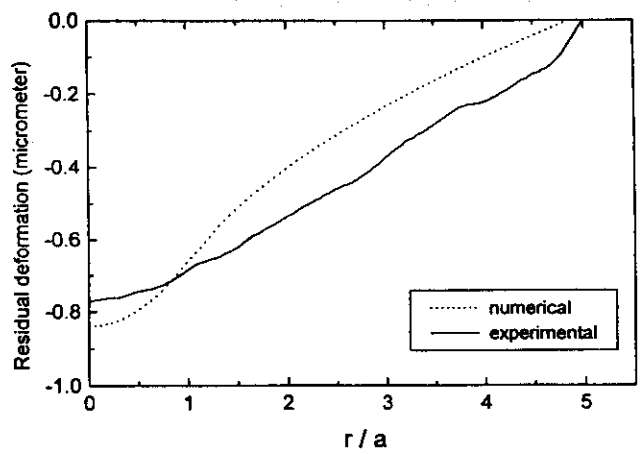

Figure 6. A comparison between experimental and numerical out-of-plane residual displacements.

200 Å deep, which is the penetration range of 35 keV ions [15]. As can be seen in figure 4, the thermal effect is extended over a layer thickness of about 40 000 Å. Therefore, the contribution of strains caused by defects can be neglected.

When the implantation process was carried out with monoenergetic ions in a low-current device, Auleytner *et al* [19] observed residual stresses due to dislocations created at the edge between implanted and unimplanted layers. However during the implantation with the plasma focus device, the continuous energy spectrum of the accelerated ions, which gives a smoothly decreasing ion concentration distribution, and the thermal effect do not indicate the formation of a sharpened interface between implanted and unimplanted layers. Consequently, it is possible to affirm that thermal stresses are the main source of the generation of residual deformations in the case of argon-irradiated stainless steel in the BD-I device.

Possible sources of errors in the numerical simulation can be related to a variation in the fluence of accelerated ions from shot to shot, which was assumed constant in the temperature calculation. A random variation in the number of ions emitted per discharge is always present during the normal operation of the plasma focus device. Also, the temperature distribution was assumed uniform over the whole implanted area and this is difficult to achieve with only one discharge because of the non-uniform spatial distribution of ions.

5. Conclusions

Based on experimental results and the characteristics of ion beams emitted in plasma focus devices, it was assumed that residual deformations induced in steel specimens by ion implantation with the BD-I device are mainly due to the thermal effect developed by the ultra-short pulsed ion beams. A numerical model of this thermal effect has been developed, which explains the generation of the residual deformations due to thermal stresses. A nonlinear elastic analysis was necessary because these thermal stresses exceed the material yield limit. Also, the computation of stress and yielding at the

implanted zone was uncoupled from the computation of the residual deformations of the whole specimen. This uncoupling was possible since yielding occurs only in a very narrow layer beneath the implanted zone. Although several assumptions were made to simplify the problems of temperature and deformation computations, the model predicts a specimen deformation field similar in form and magnitude to that observed experimentally.

Acknowledgments

This work was performed under CONICET grants PID-BID 0222, 0225 and 0238 and was also partially granted by the International Atomic Energy Agency (Research Contract 6477/RB) and the ICTP Trieste (Research Grant MP 90-090).

References

[1] Poate J M, Foti G and Jacobson D C (eds) 1983 *Surface Modification and Alloying by Laser, Electron and Ion Beams* (New York: Plenum)
[2] Feugeas J N, Llonch E C, O de González C and Galambos G 1988 *J. Appl. Phys.* **64** 2648
[3] Feugeas J N, O de González C, Ferrer J, Nieto M, Peyronel M F and Sánchez G 1990 *Brazilian J. Vacuum Appl.* **9** 118
[4] Feugeas J, Sánchez G, Grigioni G and O de González C 1992 *Mater. Res. Soc. Symp. Proc.* vol 268 (Pittsburgh, PA: Materials Research Society) p 389
[5] Feugeas J, O de González C, Hermida J, Nieto M, Peyronel M F and Sánchez G 1990 *Proc. IV Latin American Workshop on Plasma Physics, Buenos Aires, 16–27 July 1990* p 150
[6] Dearnaley G 1991 *Surf. Eng.* **7** 127
[7] Pochettino A A, Feugeas J N, Ortiz M and Sánchez G 1991 *Proc. 3rd Int. Conf. on Residual Stresses, Tokushima, 1991*
[8] Kaufmann G H, Feugeas J N, Marino B and Galizzi G 1991 *Appl. Opt.* **30** 85
[9] Feugeas J, Sánchez G, Grigioni G, O de González C, Pochettino A 1993 *Proc. Industrial Applications of Plasma Physics. Varenna, 2–11 September 1992* ed G Bonizzoni *et al* (Bologna: Società Italiana di Fisica)
[10] Kaufmann G H, Brühl S P, Galizzi G E and Feugeas J N 1995 *Opt. Laser Technol.* **27** 57
[11] Foerster C E, Amaral L, Behar M, Vazquez A and Fichtner P F P 1994 Thermal behaviour of bubbles and nitrides in a Cr-rich steel, private communication
[12] Sánchez G, Grigioni G and Feugeas J 1995 *Surf. Coatings Technol.* **70** 181
[13] Stygar W, Gerdin G, Venneri F and Mandrekas J 1982 *Nucl. Fusion* **22** 1161
[14] Kaufmann G H, Brühl S P and Feugeas J N 1995 *Surf. Coatings Technol.* **70** 187
[15] Ziegler J F, Biersack J P and Littmark U 1985 *The Stopping and Range of Ions in Solids* (New York: Pergamon)
[16] Timoshenko S and Goodier J M 1951 *Theory of Elasticity* 2nd ed (New York: McGraw-Hill)
[17] Jakob M 1949 *Heat Transfer* (New York: Wiley)
[18] Weast R 1980 *CRC Handbook of Chemistry and Physics* (Boca Raton, FL: CRC)
[19] Auleytner J and Morawiec J 1993 *Phys. Status Solidi* a **138** 403

Surface and Coatings Technology, 70 (1995) 181–186

Thermal effect of ion implantation with ultra-short ion beams

G. Sánchez, G. Grigioni and J. Feugeas

Instituto de Física Rosario (CONICET-UNR), Bv. 27 de Febrero 210 bis, 2000 Rosario (Argentina)

Abstract

Ion implantation with plasma guns operated in the detonation mode presents several differences from normally used low current ion implanter systems.

The most important differences are the high power of the beams generated with the plasma guns owing to their pulsed nature on one hand, and the plasma environment in which the target is immersed during the process of implantation on the other hand. Both effects were studied in this work.

The temperature profiles and their evolutions during and after nitrogen implantation in pure titanium, stainless steel and copper were investigated by using the finite differences method. The calculation for nitrogen ion implantation (fluence of 10^{13} cm^{-2} and pulse time of 400 ns) in pure titanium, shows melting layers of 20 nm after the first 200 ns of implantation, with a fast cooling after the end of implantation. Thermal gradients of 1000 K μm^{-1} and a heating rate of 5 K ns^{-1} were also observed.

Optical spectroscopy observations (real time spectroscopy) of the implantation region show a highly activated nitrogen plasma.

Both effects can be of extreme importance in several applications such as, for example, titanium nitriding because of an extra temperature assisted absorption by the getter effect.

1. Introduction

Ion implantation has been shown to be a powerful technique for the surface treatment of materials. Different concepts and devices have been developed with results both for research purposes and for industrial applications, which are widely described in the literature.

A different procedure for pulsed ion implantation has been developed by the Plasma Physics Group of the Instituto de Física Rosario. The accelerator (the BD-I device described elsewhere [1]) produces ion beams of short time duration, between 300 ns and 500 ns, with a continuous ion energy spectrum between 20 keV and 500 keV and fluences of approx. 10^{14} cm^{-2}. These beams are generated in a medium of highly ionized plasma of the same species of ions as those of the beam.

The resulting high power of the beam produces an extra collective effect, when used in ion implantation processes, that has to be added to the one due to the superposition of many single ion–solid interactions. These collective effects, combined with the plasma environment supported by the targets during ion implantation, are analyzed in this paper.

2. Ion beam characteristics

The ion beam is accelerated during the development of a Raleigh Taylor instability in a highly densified small plasma column (plasma focus, 1 mm diameter and 6 mm length), generated during the collapse of a plasma current sheath in a plasma gun discharge operated in the detonation mode [2]. The accelerated ions and the ions of the plasma are of the same species as the atoms of the filling gas of the coaxial interelectrodic space in the experiment.

The ion beams accelerated in such a small region have a conic geometry with a solid angle of 40° [2,3]. The acceleration time is approx, 200 ns and the energy spectrum of the ions follows the spectral law [2]:

$$\frac{dN}{dE} \propto E^{-3.4} \tag{1}$$

where N is the number of ions with energy E, with the condition $20\ \text{keV} < E < 500\ \text{keV}$. The total number of ions emitted per discharge is 1×10^{15}. This value was measured using a Faraday cup and calorimetric methods by their location at different distances downstream from the acceleration region. Specifically, the spectral law was measured with a Thompson spectrometer [2, 4], through time of flight [5,6] and by activation techniques [3]. The targets to be implanted, located downstream, receive a fluence which will depend on the distance l target–plasma focus, owing to the conic geometry of the beam. The cross-section σ_l of the conic beam is determined through the expression

$$\sigma_l = \pi(l \tan 20^0)^2 \tag{2}$$

The temporal length of the beam at the target surface will also depend on the distance l, owing to the time-of-

0257–8972/95/$9.50
SSDI 0257-8972(94)02265-R

flight ions spreading originated in their wide energy spectrum.

The remaining current sheath generated during the discharge, precursor of the plasma focus formation, is ejected downstream, reaching the target surface approximately 300 ns [5,6] after the ion beam incidence. This plasma environment can interact with the target becoming part—in major or minor degree—of the modifications of the surface layers.

3. Spectroscopic observation of the plasma

The emission spectrum of the plasma, originated as a current sheath during the discharge, was observed during nitrogen ion implantation. The experimental set-up shown in Fig. 1 consists of a triple grating monochromator with an optical multichannel analyzer (1024 cooled photodiodes) with a time resolution per spectrum of 30 ms (OMA III from Princeton Applied Research). The plasma was observed from outside the discharge chamber through a glass window, focalizing a region 10 cm downstream from the plasma focus (distance normally used in ion implantation processes) and locating the monochromator slit 70 cm from the window.

The experiment was done with the laboratory in complete darkness. The OMA was triggered 0.5 s before firing the accelerator and the acquisition system was set to operate (set in the mode of continuous sweeping) for 1 s. Taking into account that the full process of the discharge (breakdown, plasma focus formation, plasma propagation, etc.) lasts for about 1 μs, the recording of the spectrum will occur in one of the photodiode scanning sweeps. The others (approximately 30 sweeps) will record the addition of the radiation background of the laboratory, which will be added to the spectrum. The radiation background intensity was checked by allowing the OMA to run in conditions similar to the one previously described but without firing the experiment, thus given a negligible value.

The result of one spectrogram appears in Fig. 2 where it is possible to see the nitrogen emission lines NI, NII and NIII.

4. Numeric simulation of the thermal effect

Owing to the technical difficulties in measuring the temperature evolution of an extremely thin layer (thickness of the order of a micrometer) in time lapses of only several microseconds, it was evaluated by the finite differences method. The ion beam characteristics, the ion–solid interaction parameters and the thermal properties of the target material were used for the specific cases of nitrogen ions in steel, copper and titanium.

The one-dimensional heat conduction equation with an external energy source was resolved by finite differences. This method was applied by dividing the target (spatial domain) into small elements Δx, the temporal domain in small elements Δt and the energy interval of the ions (20–500 keV) in subintervals ΔE. To perform the calculations, it was necessary to find the number of ions in each subinterval, and the energy transported by them, and to calculate the energy delivered into the

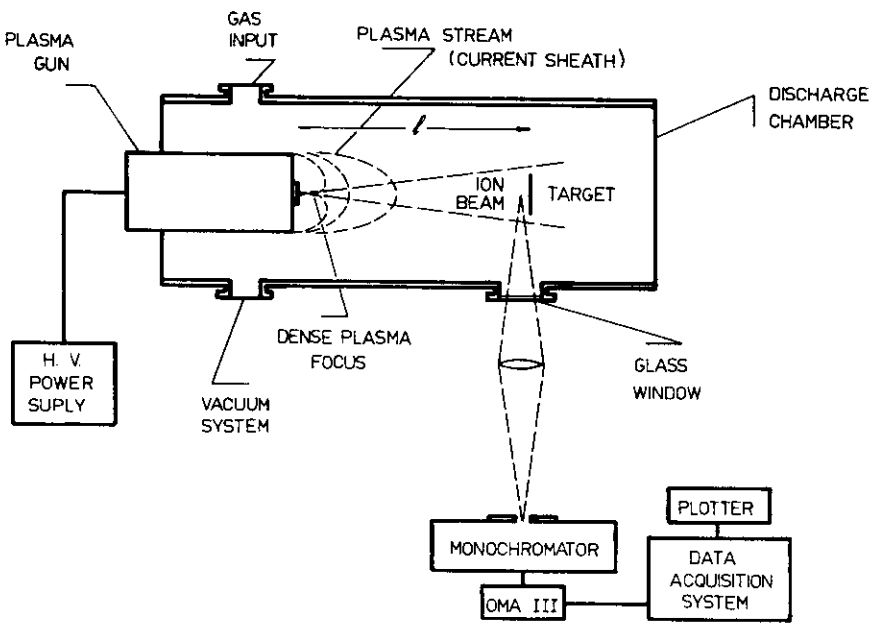

Fig. 1. Pulsed ion implanter scheme.

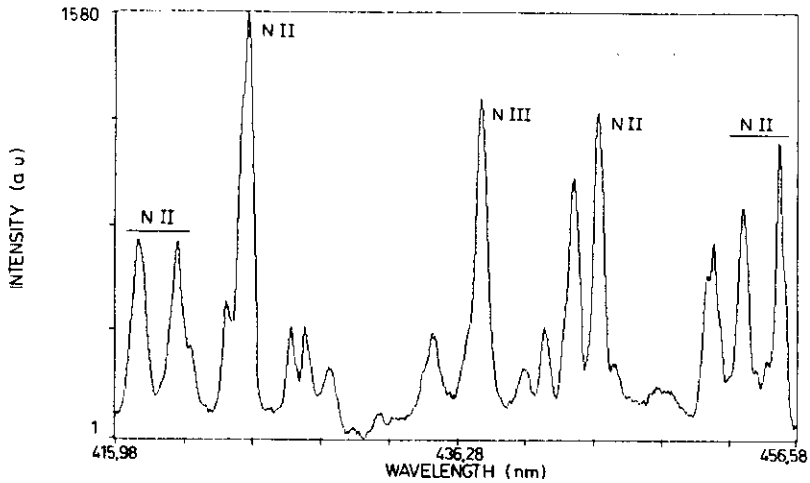

Fig. 2. Spectrogram of the target environment during nitrogen implantation.

target. After that, the temperature of each element of the spatial domain was calculated.

The temporal domain is the interval during which the thermal evolution of the target is studied, and includes the implantation time, which is determined by the temporal width of the ion beams. By the model presented, the heating and cooling profiles were calculated at every instant.

The one-dimensional heat conduction equation can be written as

$$\frac{\partial^2 T}{\partial x^2}+\frac{\dot{q}}{k}=\frac{1}{a}\frac{\partial T}{\partial t} \tag{3}$$

Where x denotes the depth into the target ($x=0$ at the surface), t is the time, k is the thermal conductivity of the material and a is the thermal diffusivity of the material.

The finite differences method [7] was applied to resolve eqn. (3). A node was assigned to each spatial subdomain, the distance between nodes being Δx. The temperature in the node i at the time t can be calculated as

$$T_i^t=\frac{1}{M}(T_{i-1}^{t-1}+T_{i+1}^{t-1})+\left(1-\frac{2}{M}\right)T_i^{t-1}+\dot{Q}_i^{t-1} \tag{4}$$

where

$$M=\frac{\Delta x^2}{a\Delta t} \tag{5}$$

$$a=\frac{k}{\rho c_p} \tag{6}$$

$$\dot{Q}_i^{t-1}=\frac{\dot{\mathcal{Q}}_i^{t-1}\Delta x^2}{kM} \tag{7}$$

where ρ is the density and c_p the specific heat of the material.

In the calculation of T_i^t was considered that the node i has received in the instant $t-1$ an energy flux $\dot{\mathcal{Q}}_i^{t-1}$. As can be seen from eqn. (4), the temperature T_i^t is a function of the temperature of node i and its neighbors ($i-1$ and $i+1$) in the instant of time $t-1$. The finite differences method ensures convergency if

$$M>2 \tag{8}$$

For a node which has not received energy, eqn. (4) becomes

$$T_i^t=\frac{1}{M}(T_{i-1}^{t-1}+T_{i+1}^{t-1})+\left(1-\frac{2}{M}\right)T_i^{t-1} \tag{9}$$

In the first approximation, thermal insulation on the surface is supposed and convection and radiation losses are neglected. Therefore the temperature for a surface node (node 0), which interacts with the beams, is

$$T_0^t=\left(1-\frac{2}{M}\right)T_0^t+\frac{2}{M}T_1^{t-1}+\frac{2}{M}\dot{Q}_i^{t-1} \tag{10}$$

and for the last node of the target (node m, at the opposite surface to that of node 0) is

$$T_m^t=\left(1-\frac{2}{M}\right)T_{m-1}^{t-1}+\frac{2}{M}T_m^{t-1} \tag{11}$$

In eqn. (7) $\dot{\mathcal{Q}}_i^{t-1}$, which is the energy flux given by the ion beams to the ith node at the instant $t-1$, can be written as

$$\dot{\mathcal{Q}}_i^t=\sum_{j=i}^{j=n}\dot{q}_j^{t-1} \tag{12}$$

where n is the number of energy subintervals. To obtain eqn. (12) we assume that the ions deliver their kinetic energy to the target uniformly in their tracks during their penetration into the target, stopping at a depth equal to the corresponding range. In the summation

only the energy flux of those ions which stop at a depth equal to or deeper than those corresponding to the ith node are considered.

The quantity $\dot{q}_j^{t\,-1}$ is the energy flux carried by the ions with energy in the jth energy subinterval. To find an expression for this quantity, as was expressed previously, it is necessary to divide the energy interval, which in our experiments is 20–500 keV, into small subintervals ΔE. For each subinterval the number of ions, the energy transported by them, and the energy flux delivered to the sample are calculated using the spectral law of the beam (eqn. (1)). A detailed description of the calculation is given in ref. 8.

The final expression for $\dot{q}_j^{t\,-1}$ results in

$$\dot{q}_j^{t\,-1} = \frac{n_j e_j}{\Delta\tau_j \Delta x \sigma_l} \tag{13}$$

All the quantities are referred to the jth energy subinterval: n_j is the number of ions, e_j is the mean energy value per ion and σ_l is the cross-section of the conic beam at a distance l from the focus given by eqn. (2). In eqn. (13) $\Delta\tau_j$ represents the time during which the interaction between the ions of such subinterval with the target takes place. Δx is the mean layer thickness taken as an average from those affected by the ions, which were calculated using the TRIM code [8,9].

To perform a calculation, we start by arbitrarily fixing ΔE. Automatically Δx is determined as was defined for eqn. (13) and Δt through the eqns. (5), (6) and (8). Taking into account ΔE, Δx, Δt, the $\dot{q}_j^{t\,-1}$ values, given by eqn. (13) and the thermal properties of the material, temperature profiles can then be calculated at every time by using eqns. (4)–(12). In the calculations, the dependence on the temperature of the thermal properties of the material is considered, taking in eqn. (5) $\Delta x \equiv \Delta x$.

The phase changes are modeled by keeping the temperature fixed at the melting (solidification) point in the nodes, until their associated mass is completely melted (solidified). Once the node is completely melted the calculations are continued using the thermal properties of the liquid mass in the same way as for the solid case. In the case where a node reaches the evaporation temperature, the calculation is aborted.

5. Results

For calculation purposes, we selected the conditions normally used in ion beam implantation: nitrogen ion beam with a fluence of 10^{13} cm^{-2} and pulse time length of 400 ns. As targets, three different materials were selected: pure titanium, stainless steel and pure copper.

The results for titanium are plotted in Fig. 3. They correspond to a family of curves, temperature *vs.* depth, at different instants of time during and after implantation (cooling-down stage after the arrival of the last ion of the beam).

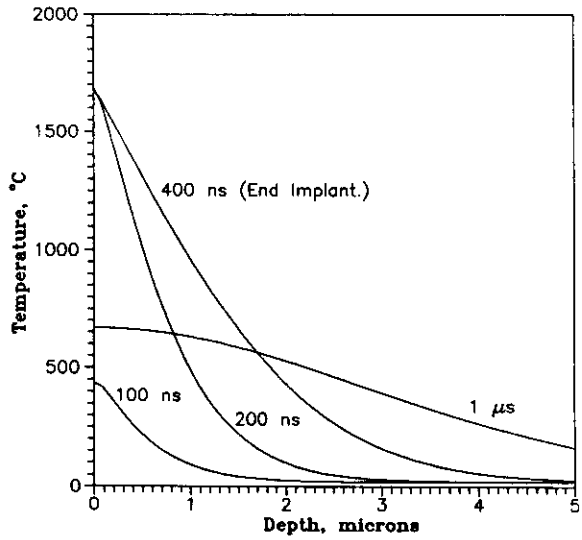

Fig. 3. Temperature profiles of nitrogen implanted titanium. Single pulse fluence 10^{13} ions cm^{-2}. Pulse time length 400 ns.

Several features in this case can be pointed out. First, the titanium melting temperature in the surface is reached during the first 200 ns, up to a depth of 20 nm after the following 200 ns. Second, the surface temperature decreases very fast after the implantation, reaching 650 °C only 600 ns after the arrival of the last ion of the beam. Finally, a high thermal gradient of about 1000 K μm^{-1} and an equally high rate of heating of about 5 K ns^{-1} can be observed.

In Fig. 4 the results for stainless steel are plotted. The curves are similar to those for titanium except that, in this case, the steel melting temperature is not reached at

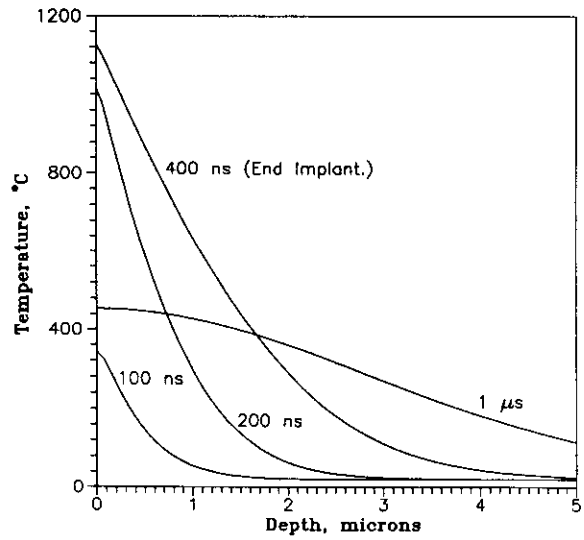

Fig. 4. Temperature profiles of nitrogen implanted austenitic stainless steel. Single pulse fluence 10^{13} ions cm^{-2}. Pulse time length 400 ns.

any time. The peak temperature is 1120 °C, which is reached at the end of implantation (400 ns) in the target surface.

Finally, in Fig. 5 the results for copper are presented showing a remarkably lower peak temperature (only 365 °C at the end of the implantation) and a lower temperature gradient in comparison with the preceding cases. Both effects can be attributed to the high thermal conductivity of copper, which improves the cooling down process through thermal conduction to the target bulk.

6. Discussion and conclusions

The process of the pulsed ion implantation described shows important differences with respect to the conventional systems used as much in research as in technological applications. These differences can be summarized by two relevant factors: (i) the strong thermal effect that is added to a single ion implantation process; (ii) the highly activated plasma that reaches the surface of the target immediately after the ion beam.

The strong thermal effect provokes a fast surface heating during the implantation, elevating the surface temperature to values that can be as high as to provoke the melting down and even the evaporation of the surface layers. The short time duration of the process provokes strong temperature gradients from the surface to the bulk of the sample during the implantation, with an additional fast cooling down process after the implantation which virtually leaves the sample at room temperature in only a few tens of microseconds.

The plasma cloud arrives to the target approximately 300 ns after the end of implantation [6] when the temperature of the surface, owing to its interaction with the ion beam, is still high. This process can be advantageous in certain cases, such as in surface nitriding processes, because the high temperature can help extra nitrogen absorption through the surface and nitrogen diffusion toward deeper layers.

With this kind of pulsed implanter, in which the ion beam fluence is relatively low, it is possible to obtain higher values of fluences by the accumulation of successive single shots. Normally this process can be done in a sequence of one or two ion beam pulses per second. Taking into account that the target cools down in only tens of microseconds, in this sequence every ion beam pulse will reach the surface at room temperature, repeating a similar thermal process each time. This means that the nitrogen concentration profile in the surface layers, implanted by preceding pulses, will suffer a redistribution owing to the thermal effect when a new pulse arrives. This can result in a higher penetration depth and a better uniformity in the profile of concentration [10]. In particular, for the case of nitrogen implantation in titanium, the combined effect of temperature and highly activated plasma from this process results in implanted layers with a high and uniform concentration of nitrogen and the development of titanium nitride compounds with desirable stoichiometry, for example, for surface hardening [10,11].

Finally, the ion implantation process using this repetitive pulsed method presents interesting results that can be taken into account principally as a potential alternative for material surface treatment for tribological purposes.

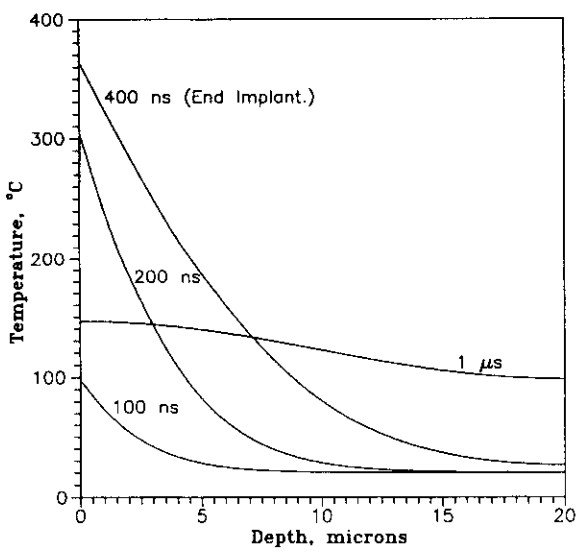

Fig. 5. Temperature profiles of nitrogen implanted copper. Single pulse fluence 10^{13} ions cm^{-2}. Pulse time length 400 ns.

Acknowledgments

We are grateful to A. Muñoz for his collaboration in the experimental work. Work was performed under CONICET Grant BID-PID No. 222, IAEA Research Contract No. RC/6477/R1/RB, and International Centre for Theoretical Physics TWAS Research Grant No. MP 90-090.

References

1 J. Feugeas, E. Llonch, C. O. de González and G. Galambos, *J. Appl. Phys.*, *64* (5) (1988) 2648.
2 W. Stygar, G. Gerdin and F. Venneri, *Nucl. Fus.*, *22* (9) (1982) 1161.
3 Y. Kondoh, K. Shimoda and K. Hirano, *Jpn. J. Appl. Phys.*, *20* (2) (1981) 393.
4 M. J. Rhee, *Appl. Phys. Lett.*, *37* (1980) 906.
5 V. Nardi, W. Bostick, J. Feugeas, W. Prior and C. Cortesse, *Nucl. Fus.*, *2* (1979) 143.
6 W. Bostick, V. Nardi, J. Feugeas and W. Prior, *Energy Storage*

Compression and Switching II, Plenum, New York, 1983, pp. 257–287.
7 D. Kern, *Procesos de Transferencia de Calor*, Compañía Editorial Continental S.A., Mexico, 1980.
8 J. Feugeas and G. Sánchez, work in preparation, 1994.
9 J. F. Ziegler, J. P. Biersack and U. Littmark, *The Stopping and Range of Ions in Solids*, Pergamon, New York, 1985.
10 J. Feugeas, G. Sánchez, G. Grigioni and C. O. de Gonzale, in K. Grabowski (ed.), *Proc. Mater. Res. Soc. Symp., Materials Modification by Energetic Atoms and Ions, San Francisco, CA, April 1992*, Materials Research Society, Pittsburgh, PA, Vol. 268, 1992, p. 389.
11 J. Feugeas, C. O. de Gonzalez and G. Sánchez. *Radiat. Eff. Defects Solids*, (1993) in press.

Reprinted from

SURFACE & COATINGS TECHNOLOGY

Surface and Coatings Technology 110 (1998) 13–18

Hydrogen permeation modification of 4140 steel by ion nitriding with pulsed plasmas

Pablo Bruzzoni [a], Sonia P. Brühl [b], Bernardo J.A. Gómez [b], Liliana Nosei [c], María Ortiz [a], Jorge N. Feugeas [b,*]

[a] *CNEA, Unidad de Actividad Materiales, CC 32 Suc. 64B, 1464 Buenos Aires, Argentina*
[b] *Instituto de Física Rosario (UNR-CONICET), Bv. 27 de Febrero, 210 bis. 2000 Rosario, Argentina*
[c] *Instituto de Mecánica Aplicada y Estructuras (UNR), Riobamba 245 bis. 2000 Rosario, Argentina*

Received 15 April 1998; accepted 7 June 1998

ELSEVIER

SURFACE AND COATINGS TECHNOLOGY

Scope
The increasing requirement for high technology materials with specific performance characteristics in various types of environments has dictated that these materials possess near-surface properties different from their bulk properties. This journal is a principal forum for the interchange of information on the science, technology and applications of thin and thick coatings and modified surfaces which alter the properties of materials. The scope includes all types of coatings and surface modification techniques (including physical vapour deposition, chemical vapour deposition, electroplating and surface modification by directed energy techniques). Of particular emphasis are the emerging advanced processes such as thermal spraying, sputter deposition, activated reactive evaporation, ion plating, molecular beam epitaxy, ion implantation and pulsed laser surface deposition. Contributions range from original scientific articles concerned with applied research or direct applications of coatings to reviews of current technology in specific areas. Papers are solicited on topics which include one or more of the following areas: (1) characterization of coatings and modified surfaces, which includes the determination of composition, structure, adhesion, and internal stresses; (2) the application of coatings and modified surfaces to alter the mechanical, chemical or optical properties of materials. Mechanical properties include friction, wear, erosion, hardness and load bearing capacity. Chemical properties include corrosion and oxidation. Optical and electro-optical properties include reflectivity, selective absorption and electroluminescence. Particular emphasis is also placed on the emerging surface engineering technologies and coatings with a diversity of applications such as diamond, diamond-like carbon, and cubic boron nitride. Other interdisciplinary areas include thermal barrier coatings and coatings for biomedical applications and materials conservation.

Abstracting/Indexing Services
This journal is cited by the following services:
Engineering Index, FIZ Karlsruhe, Metal Finishing Abstracts, Current Contents — Engineering, Technology and Applied Sciences, Physikalische Berichte, Cambridge Scientific Abstracts, Chemical Abstracts, Fluid Abstracts, Metals Abstracts, Physics Abstracts, PASCAL/Centre National de Recherche Scientifique, Solid State Abstracts.

Pre-publication abstracts of articles in *Surface and Coatings Technology* and other related journals are now available weekly in electronic form via CoDAS, a new direct alerting service in condensed matter and materials science run jointly by Elsevier Science and Institute of Physics Publishing. For details on a free one-month subscription contact Paul Bancroft on fax +44 1179 294318 or e-mail bancroft@ioppublishing.co.uk.

Publication Information
Surface and Coatings Technology (ISSN 0257-8972). For 1999 volumes 109–121 are scheduled for publication. Subscription prices are available upon request from the Publisher. Subscriptions are accepted on a prepaid basis only and are entered on a calendar year basis. Issues are sent by surface mail except to the following countries where Air delivery via SAL mail is ensured: Argentina, Australia, Brazil, Canada, Hong Kong, India, Israel, Japan, Malaysia, Mexico, New Zealand, Pakistan, PR China, Singapore, South Africa, South Korea, Taiwan, Thailand, USA. For all other countries airmail rates are available upon request. Claims for missing issues should be made within six months of our publication (mailing) date.

Orders, claims and product enquiries: please contact the Customer Support Department at the Regional Sales Office nearest you:

New York: Elsevier Science, PO Box 945, New York, NY 10159-0945, USA;
phone: (+1) (212) 633 3730 [toll free number for North American customers: 1-888-4ES-INFO (437-4636)];
fax: (+1) (212) 633 3680;
e-mail: usinfo-f@elsevier.com

Amsterdam: Elsevier Science, PO Box 211, 1000 AE Amsterdam, The Netherlands;
phone: (+31) 20 4853757; fax: (+31) 20 4853432;
e-mail: nlinfo-f@elsevier.nl

Tokyo: Elsevier Science, 9-15 Higashi-Azabu 1-chome, Minato-ku, Tokyo 106-0044, Japan;
phone: (+81) (3) 5561 5033; fax: (+81) (3) 5561 5047;
e-mail: info@elsevier.co.jp

Singapore: Elsevier Science, No. 1 Temasek Avenue, #17-01 Millenia Tower, Singapore 039192;
phone: (+65) 434 3727; fax: (+65) 337 2230;
e-mail: asiainfo@elsevier.com.sg

Rio de Janeiro: Elsevier Science, Rua Sete de Setembro 111/16 Andar, 20050-002 Centro, Rio de Janeiro - RJ, Brazil;
phone: (+55) (21) 509 5340; fax: (+55) (21) 507 1991;
e-mail: elsevier@campus.com.br [Note (Latin America): for orders, claims and help desk information, please contact the Regional Sales Office in New York as listed above]

US mailing notice—*Surface and Coatings Technology* (ISSN 0257-8972) is published monthly by Elsevier Science S.A. (PO Box 564, 1001 Lausanne). Annual subscription price in the USA is US$ 4622.00 (valid in North, Central and South America), including air speed delivery. Second class postage rate is paid at Jamaica, NY 11431.
USA POSTMASTER: Send address changes to *Surface and Coatings Technology* Publications Expediting, Inc., 200 Meacham Avenue, Elmont, NY 11003.
AIRFREIGHT AND MAILING in the USA by Publications Expediting.

ELSEVIER

Surface and Coatings Technology 110 (1998) 13–18

SURFACE & COATINGS TECHNOLOGY

Hydrogen permeation modification of 4140 steel by ion nitriding with pulsed plasmas

Pablo Bruzzoni [a], Sonia P. Brühl [b], Bernardo J.A. Gómez [b], Liliana Nosei [c], María Ortiz [a], Jorge N. Feugeas [b,*]

[a] *CNEA, Unidad de Actividad Materiales, CC 32 Suc. 64B, 1464 Buenos Aires, Argentina*
[b] *Instituto de Física Rosario (UNR-CONICET), Bv. 27 de Febrero, 210 bis, 2000 Rosario, Argentina*
[c] *Instituto de Mecánica Aplicada y Estructuras (UNR), Riobamba 245 bis, 2000 Rosario, Argentina*

Received 15 April 1998; accepted 7 June 1998

Abstract

It is widely known that the hydrogen in steel produces embrittlement. This effect may cause the failure of the elements (confining walls, mechanical parts, etc.) whose surfaces are in contact with this gas or with processes in which hydrogen is continuously generated. In this work it is shown that the ion nitriding of the surface of AISI 4140 is a good mechanism to act as a barrier against hydrogen permeation in its bulk. The ion nitriding was performed using a square wave DC glow discharge. The development of a compound layer of iron nitrides was observed as the cause of the hydrogen permeation reduction. For equal duration of treatment, thicker compound layers were developed in higher discharge/post-discharge ratios in the square wave of the applied voltage onto the sample (cathode), with a greater reduction of hydrogen permeation coefficient as a consequence. Nevertheless, the permeation was not reduced to zero in any of the treatment conditions used. The results of the analysis of the permeation tests and the image of the photomicrographs showed that the existence of cracks, fractures, failures, etc. in the compound layer (pre-existing in the AISI 4140 steel) could be the cause of the residual hydrogen permeation. This can be attributed to the movement of the hydrogen through these defects diffusing through the original α-Fe phase of the non-treated steel.

Keywords: Barrier layer; Diffusion; Hydrogen; Ion nitriding; Permeation; Pulsed plasma

1. Introduction

Hydrogen, as an interstitial element in steel, produces a detrimental effect, principally through the modification of the mechanical properties of the material, inducing embrittlement. Hydrogen may also enhance the damage kinetics associated with failure by stress corrosion cracking, corrosion fatigue and creep. For this reason, several efforts have been made to design surface-engineered hydrogen contamination barrier layers, using coating methodologies (CVD, PVD) or surface modification techniques such as ion implantation or plasma nitriding, in order to reduce the hydrogen diffusion coefficient. Metal nitrides, as ionic compounds, are expected to present very low hydrogen diffusion rates and to be suitable for this purpose, i.e. protective nitride layers are already used on steels to prevent corrosion [1], and they can act simultaneously as hydrogen barriers in corrosive environments. Another possible application of nitride layers is as tritium barriers in prospective nuclear fusion systems [2,3]. Tritium is a radioactive hydrogen isotope and its permeation through the steel wall of the containers of fusion systems must be avoided.

One of the most recent techniques used in surface modification is ion nitriding [4,5], which is essentially a process of thermochemical diffusion assisted by plasma, which generates a layer of iron nitrides and nitrogen in solution that can reach depths of 500 μm or more. In this work, we use a nitriding process based on pulsed DC discharge, varying the time ratio between the discharge and the post-discharge, in a mixture of nitrogen and hydrogen in different proportions and varying the time ratio, in each pulse, between the discharge and the post-discharge [6]. To evaluate the hydrogen permeation the hydrogen electrochemical permeation technique was

* Corresponding author. Fax: +54 41 821772; e-mail: feugeas@ifir.ifir.edu.ar

0257-8972/98/$ - see front matter
PII S0257-8972(98)00540-4

used, which is one of the best techniques to evaluate the effectiveness of such barriers, due to its high sensibility and the simplicity of the equipment involved. The surfaces were characterized by X-ray diffraction and optical metallography under the surface at different depths.

2. Experimental

2.1. Ion nitriding

Nitriding was performed using the equipment developed by the Plasma Physics Group at IFIR. A schematic illustration of the nitriding plasma reactor is shown in Fig. 1. The reactor consists of one stainless steel circular plane electrode 6 mm thick and 35 mm in diameter (sample holder) located inside the cavity of the other, a cylindrical cage 50 mm in diameter and 130 mm in length built in a stainless steel grid. The sample electrode was negatively biased (cathode) and the cage (anode) was at ground potential. The electrodes were located in a cylindrical Pyrex glass vacuum chamber (70 mm in diameter and 290 mm in length). It is possible to monitor the active species generated in the glow discharge by plasma emission spectroscopy [7].

The cathode was connected to the power supply through a cylindrical hollowed stainless steel rod which permitted the introduction of a thermocouple to monitor the temperature of the electrode in the plasma region. The rod was completely covered by a Pyrex pipe, avoiding plasma generation along its surface, and ensuring that the discharge was generated only around the surface of the cathode planar disc (25 cm^2).

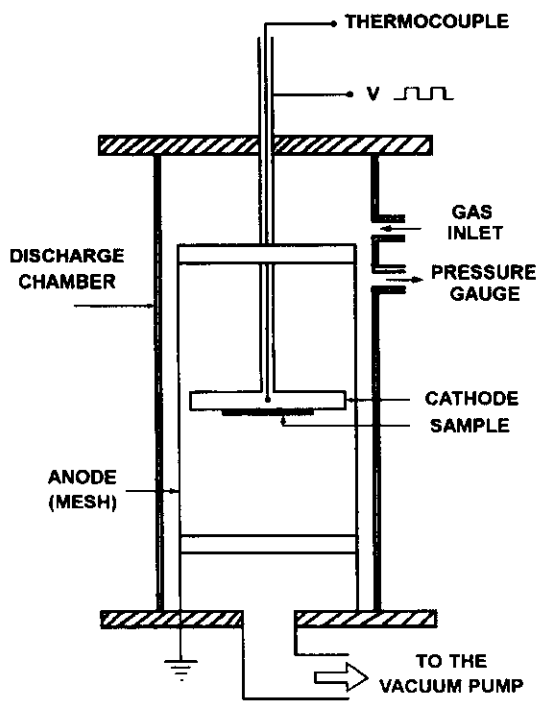

Fig. 1. Schematic diagram of the ion nitriding reactor.

The voltage applied to the cathode was a square wave 450 V in amplitude with a frequency of 100 Hz, and a variable ratio between the discharge (negatively biased electrode) and the post-discharge (zero potential electrode). In our work we used two different ratios (percentage discharge/post-discharge): (i) 50/50 and (ii) 65/35. The current density on the sample during the active part of the cycle of the discharge was kept constant at a value of 4.2 mA cm^{-2}.

Prior to introducing the process gases, the chamber was evacuated to a base pressure of 15 mTorr (2 Pa). In our work we use a flowing gaseous mixture of N_2 and H_2 in two different proportions: (a) 80 vol% N_2 + 20 vol% H_2; (b) 80 vol% H_2 + 20 vol% N_2.

The permeation tests were performed on 30 mm diameter and 1.5 mm thick discs of AISI 4140 steel untreated and nitrided during 6 h under three different conditions.

Condition 1: 80% N_2–20% H_2, ratio discharge/post-discharge 50/50.

Condition 2: 80% N_2–20% H_2, ratio discharge/post-discharge 65/35.

Condition 3: 20% N_2–80% H_2, ratio discharge/post-discharge 50/50.

After the first 10 min of process, the temperature was stabilized at 460, 430 and 240 °C for conditions 1, 2 and 3 respectively. The hydrogen, necessary in the mixture for an efficient nitriding process [4,8], is not retained in the bulk at these temperatures because temperatures above 100 °C provoke hydrogen degassing.

2.2. Surface characterization

The surfaces of the sample were characterized using X-ray diffraction and optical metallography.

The X-ray diffraction analyses were performed using Cu Kα with monochromator (mean penetration depth ~5 μm) as incident radiation, and the analyses of the diffractograms were performed using the Lutteroti version of the Rietveld method [9].

2.3. Permeation tests

For the permeation tests a double cell method already described in ref. [10] was used, with a gaseous load of hydrogen at 1 atm and an electrochemical detection. The minimum current measured by this method is ~1 nA, which corresponds to a hydrogen flux of 10^{-10} cm^3 H_2 (PTN) s^{-1}. Before the permeation tests, the opposite surface of the sample (non-nitrided surface), which is the hydrogen exit surface in the permeation test, was electropolished to eliminate surface deformation induced by the abrasion. Then, a thin Pd film was electroplated on both sides of the membrane. Every sample was degassed in an oven (4 h, 100 °C). For each

sample the permeation–degassing transient was recorded for two different temperatures: 30 and 70 °C.

3. Results

3.1. Nature and structure of the nitride layers

In Fig. 2 several photomicrographs of nitrided layers can be seen. The surface layer nitrided under condition 3 did not show (for the maximum resolution used) changes with respect to the untreated one [part (e) of the figure]. On the contrary, important changes can be seen in the samples nitrided under condition 1 [parts (a) and (b)] and even more important when nitrided under condition 2 [parts (c) and (d)]. For the case of treatment under condition 1, a white layer of ~1 μm thickness in the surface followed by a layer with dispersed nitride particles of ~50 μm were developed onto the unmodified base material. A similar layer distribution can be seen at the surface treated under condition 2, but in this case the white layer and the diffusion layers had ~7–8 μm and ~100–150 μm respectively.

In Fig. 2(c) and 2(e) (photomicrographs observed

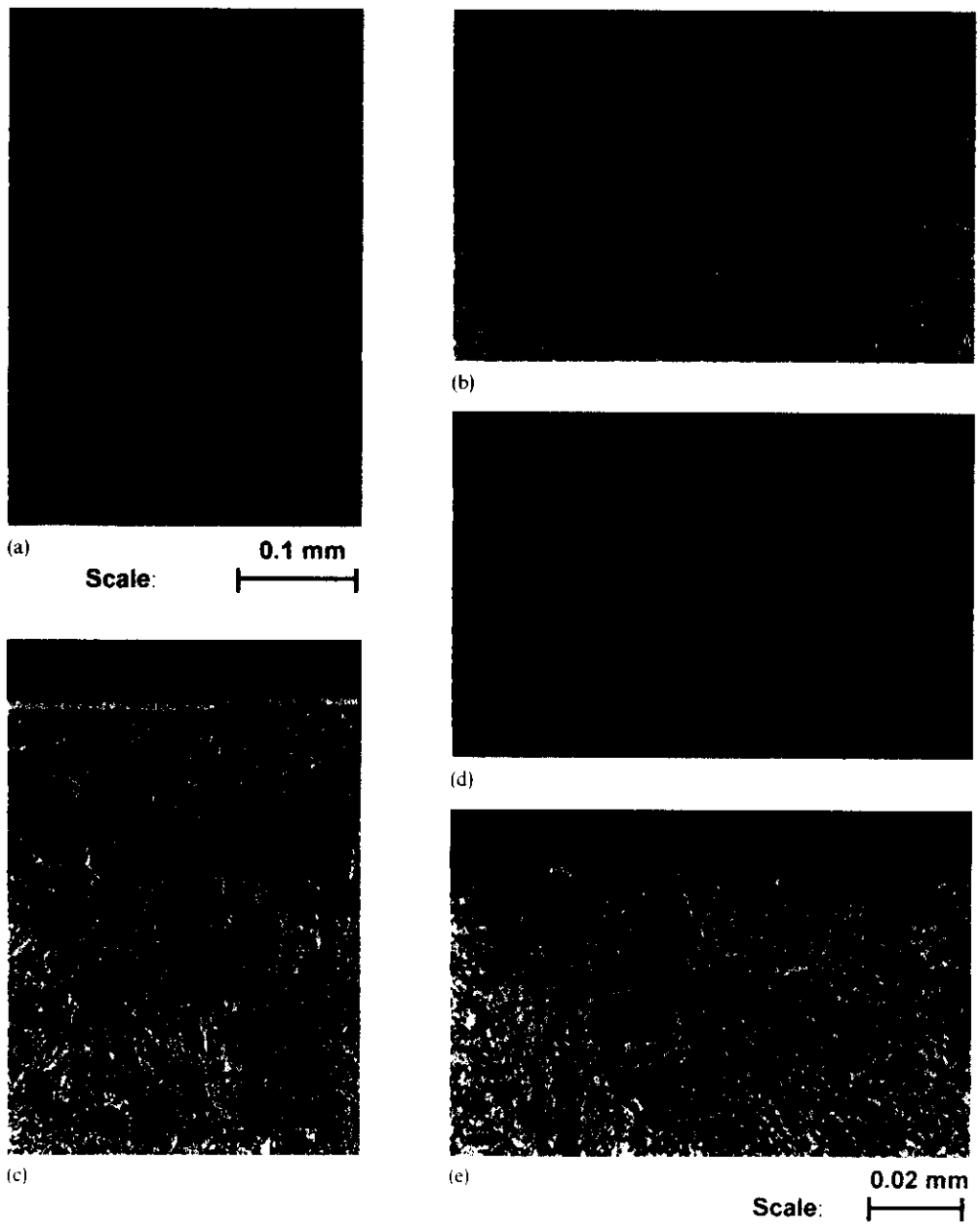

Fig. 2. Photomicrographs of the surface layers treated under different conditions: (a) 200× enlargement; (b) 800× enlargement, treated under condition 1; (c) 200× enlargement; (d) 800× enlargement, treated under condition 2; (e) 800× enlargement, treated under condition 3.

under maximum enlargement) it is possible to see some penetration of the white layer deeper into the material in determined boundary localized regions. These discontinuities can be associated with grain boundaries which facilitate the nitriding process, by going deeper into the bulk.

For a non-treated sample the X-ray diffractograms show peaks [Fig. 3(a)] corresponding largely to the α-Fe phase with a lattice parameter $a=2.8692$ Å and others corresponding to the cementite phase (~6 wt%). The width of the diffraction peaks shows a low level of microstrain ($\sim 1\times10^{-3}$), in accordance with a tempered material.

In Fig. 3(d), the result corresponding to a sample nitrided under condition 3 is presented. The diffractogram shows little variation with respect to the preceding case. The peaks due to α-Fe show a higher lattice parameter $a=2.8735$ Å, which can be attributed to two different effects: nitrogen dissolved in the lattice and the presence of residual macrostresses. Also, the measured microstrain values of $\sim 2\times10^{-3}$ were higher than that for the non-treated case. Nevertheless, it is also possible to observe the presence of peaks that could be attributed to a very thin (~0.02 μm) layer of the ϵ-Fe_3N (hexagonal phase).

The result corresponding to a sample nitrided under condition 1 is shown in Fig. 3(b). The α-Fe and two nitride compounds can be clearly identified. The α-Fe shows a lattice parameter $a=2.8713$ Å with a microstrain $\sim 3\times10^{-3}$. The two compounds conform to a surface layer ~1.5 μm thick and correspond to ϵ-Fe_3N (~33 wt%) and the cubic γ'-Fe_4N phase (~67 wt%). The relative intensities between the peaks show preferential lattice orientation (texture) for both phases. At a microstructural level it can be seen that the microstrain level of the ϵ-Fe_3N ($\sim 2\times10^{-3}$) is much higher than that of the γ'-Fe_4N ($\sim 10^{-6}$); in spite of that, the domain size shows a reverse behavior, with 900 Å for the ϵ-Fe_3N and ~40 Å for the γ'-Fe_4N. In addition, at $2\theta\sim45.7°$ a very wide peak corresponding to a very small particle size could be observed, which could indicate the presence of the α''-$Fe_{16}N_2$ phase.

Finally, the diffractogram corresponding to a sample nitrided under condition 2 can be seen in Fig. 3(c). In this case, the iron peaks were greatly reduced, indicating the presence of a thick nitride layer (6 μm). The compound layer was composed of the same nitrides as in the preceding case, but in a different proportion: 84 wt% for the ϵ-Fe_3N and 16 wt% for the γ'-Fe_4N. The microstrain and the domain size are similar to those measured for the preceding case (nitriding condition 1).

3.2. Permeation under steady state

The permeation tests were done using two samples for each different type of treatment (non-treated and nitrided under conditions 1, 2 and 3).

Fig. 4 shows the permeation coefficient (hydrogen flux in steady state, normalized to the sample thickness and the hydrogen pressure) related to the permeation coeffi-

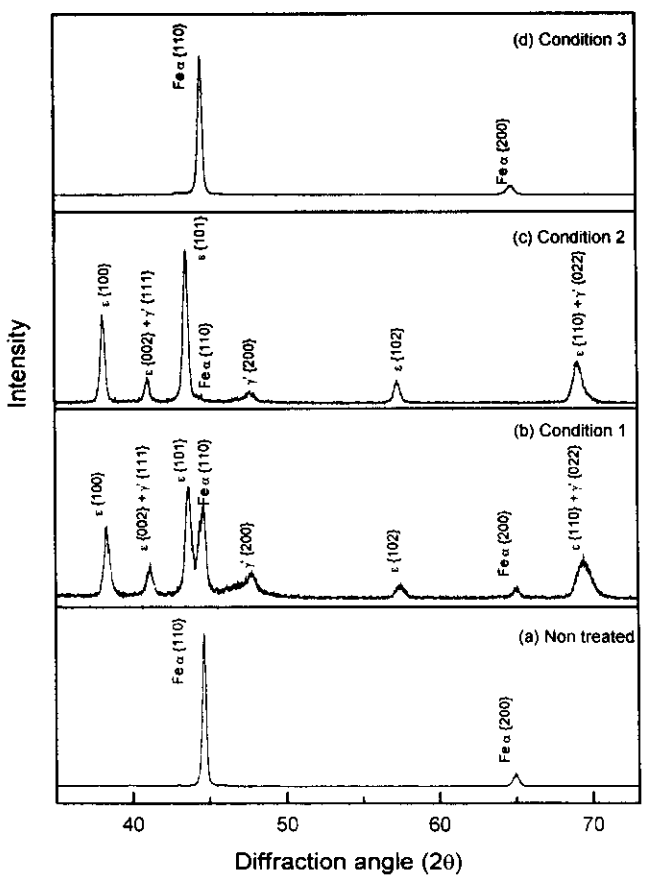

Fig. 3. Diffractograms of surface layers: (a) untreated surface; (b) surface nitrided under condition 1; (c) nitrided under condition 2; (d) nitrided under condition 3.

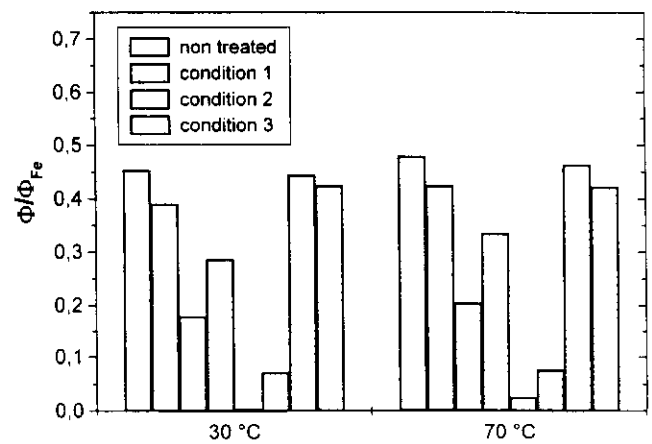

Fig. 4. Hydrogen permeation results. Permeation coefficients Φ_x referred to the annealed α-Fe coefficient Φ_{Fe} for the two testing temperatures used.

cient for annealed pure iron (as extracted from ref. [10], and expressed as the quotient between the stationary hydrogen flux for the sample tested divided by the stationary hydrogen flux for pure iron, Φ/Φ_{Fe}). For the non-treated material the observed values were ~50% from the pure Fe case, which corresponds to a typical commercial alloy.

The treatment under the nitriding condition 3 (80% H_2–20% N_2) did not produce any detectable reduction in the stationary flux of hydrogen.

Nevertheless, the treatment under nitriding condition 1 and condition 2 (80% N_2–20% H_2) provoked a clearly greater reduction in the steady state flux, the greater the ratio between the active part of the discharge with respect to the post-discharge (square wave applied voltage).

By looking at the results presented in Fig. 4, it is possible to see that there was an important dispersion between samples treated under similar conditions. Nevertheless, it is possible to note that for each sample, the ratio between the measured permeation and those corresponding to pure iron is almost constant despite temperature changes.

3.3. Permeation under non-steady state

In Table 1 the apparent diffusion coefficients computed through the "time lag" are shown. These values are the average from the rising and decay transients. The observed tendency of the diffusion coefficients for the samples nitrided under conditions 1 and 2 was similar to that observed for the permeation coefficients under steady state, with the lower diffusion coefficient corresponding to nitriding condition 2. Nevertheless, the apparent diffusion coefficient for the nitriding condition 3 had values slightly higher than those of the base material, a situation which was not observed for the permeation coefficients under steady state.

4. Discussion

The results corresponding to steady state hydrogen permeation coefficients (Φ/Φ_{Fe}) showed a reduction with respect to the measurement performed on the base material when the samples were nitrided under conditions 1 and 2. However, no modification was observed when samples were nitrided under condition 3.

Table 1
Apparent hydrogen diffusion coefficient in the 4140 steel. Calculated from the time lag of rising permeation transients

Treatment	D (30 °C) (10^{-6} cm^2 s^{-1})	D (70 °C) (10^{-6} cm^2 s^{-1})
Non-nitrided, as received	1.0–1.2	4.4–4.9
Non-nitrided, annealed (250 °C, 6 h)	1.7–1.9	7.5–8.2
Nitrided, condition 1	0.49–0.60	2.9–4.1
Nitrided, condition 2	0.053–0.19	0.17–1.5
Nitrided, condition 3	1.7–1.9	7.5–8.8

Nevertheless, as can be seen from Fig. 4 for each sample, the ratios between the Φ/Φ_{Fe} values (steady state hydrogen permeation coefficients) for the two temperatures tested (30 and 70 °C) were almost constant. Considering the cases in which the samples were nitrided under conditions 1 and 2, and the compound layers (composed of the ϵ-Fe_3N and γ'-Fe_4N phases) were developed on the surface, the behavior under the temperature modification of Φ (corresponding to the nitride layer) should be different from that of Φ_{Fe} (corresponding to pure iron) because of the different nature of the materials. On the contrary, a similar behavior was observed for both materials (iron nitrides and pure iron) under temperature modification. This fact suggests that the diffusion mechanism is governed by that corresponding to pure iron, and that the diffusion takes place only through the α phase pre-existing in the base material. In the compound layer, which should be totally hydrogen-tight, this can happen only through the existence of discontinuities like cracks, defects, failures, etc. in their structure.

The existence of cracks can be visualized in the opposite way: by observing Fig. 2(b) and 2(d) it is possible to see the selective nitriding process in determined regions under the almost uniform compound layer which develops tongs of nitrides which penetrate well into the diffusion zone. This effect is attributed to the easiest way that nitrogen passes through such discontinuities. The same process can be carried out by hydrogen during the hydrogen permeation tests.

On the other hand, the apparent diffusion measurements on ion nitrided samples under conditions 1 and 2 showed similar comparative behavior in the case of the steady state hydrogen permeation coefficient. For both cases, the apparent diffusion coefficient was reduced, with maximum attenuation for the case in which the percentage of discharge in the cycle was 65% (nitriding under condition 2). Nevertheless, the results observed for the ion samples nitrided under condition 3 showed that the apparent diffusion coefficient was slightly higher than that corresponding to the base material.

The apparent diffusion coefficient observed for the case in which samples were treated under ion nitriding conditions 1 and 2 can be originated not only in the compound layer of the surface, but also in the diffusion zone in which part of the nitrogen was dissolved into the lattice. This nitrogen interstitially located in the ferrite increases the lattice parameter of the α-Fe and eventually gives rise to the incipient formation of the α''-$Fe_{16}N_2$ phase, increasing at the same time the density of dislocations. These dislocations, which work as

hydrogen traps, contribute to the reduction of the apparent diffusion coefficient. The difference between both nitriding conditions is originated in the thickness of both layers (compound and diffusion zone), as can be observed in Fig. 2.

Nevertheless, this effect was not observed for the case of treatment under condition 3. The reason can probably be found in the high density of traps pre-existing in the base material, for which the apparent diffusion coefficient at 30 °C was ~80 times lower than that of the annealed pure iron [11] (see Table 1). The low increase in the apparent diffusion coefficient observed for the case of samples treated under condition 3 could be due to stress relief by heating (240 °C during 6 h) during the ion nitriding process. This hypothesis was assessed by subsequent permeation tests on the non-nitrided material subjected to the same thermal history (240 °C, 6 h) as in nitriding condition 3.

5. Conclusions

The surface treatment of steel AISI 4140 by ion nitriding with a DC pulsed glow discharge proved to be a process that can be used for barrier generation against hydrogen contamination of the bulk material.

By using a square wave voltage pulse of 100 Hz with 65% active time (discharge) and 35% post-discharge in an 80% N_2+20% H_2 gas mixture, with a 6 h treatment, the hydrogen permeation was reduced to below 10% of the value for untreated steel. Similar results were obtained for the two permeation test temperatures used: 30 and 70 °C.

The permeation reduction can be attributed to the ion nitriding compound ~7–8 μm thick layer (composed of a mixture of 84 wt% ϵ-Fe_3N and 16 wt% γ'-Fe_4N) followed by a 100–150 μm sublayer composed of nitrogen diffusion into the α-Fe matrix with some small crystals (thin acicular crystals) corresponding to the α''-$Fe_{16}N_2$ phase.

Lower discharge/post-discharge or lower N_2–H_2 concentration ratios during the ion nitriding process lead to thinner compound layers, resulting in higher hydrogen permeation.

The reason for which the permeation was not reduced even more than the observed 90% can be attributed to the fact that for this material (AISI 4140), the compound layer developed had some inhomogeneities consisting of cracks, defects, failures, fractures, etc. which exposed part of the α-Fe phase of the base material, thus allowing the hydrogen to permeate to the bulk.

Acknowledgement

This work was partially supported by IAEA (Research Contract No. ARG 9384 R1), Agencia Nacional de Promoción de la Investigación Científica y Tecnológica (PIP No. 602, 12/03/97), CONICET, the University of Rosario and Antorchas/Vitae (Project No. B-11487/6B002). The authors are indebted to Ing. Aldo Marenzana for his collaboration in the instrumentation of the experiments.

References

[1] T. Bell, Surf. Eng. 6 (1990) 31.
[2] T. Elleman, L.R. Zumwalt, C.P. Feng, T.S. Elleman, J. Nucl. Mater. B 8586 (1979) 1161.
[3] Sov. Atom. Energy 62 (1987) 65 (English translation).
[4] H. Michel, T. Czerwiec, M. Gantois, D. Ablitzer, A. Ricard, Surf. Coat. Technol. 72 (1995) 103.
[5] A. Çelik, S. Karadeniz, Surf. Coat. Technol. 80 (1996) 283.
[6] J. Bougdira, G. Henrion, M. Fabry, M. Demy, J.R. Coussenot, Mater. Sci. Eng. A 139 (1991) 15.
[7] S.P. Brühl, M.W. Russell, B.J. Gómez, G.M. Grigioni, J.N. Feugeas, A. Ricard, J. Phys. D: Appl. Phys. 30 (1997) 2917.
[8] B. Xu, Y. Zhang, Surf. Eng. 3 (1987) 226.
[9] L. Lutterotti, P. Scardi, J. Appl. Cryst. 25 (1992) 459.
[10] E. Riecke, K. Bohnenkamp, Z. Metallkde 75 (1984) 76.
[11] A.J. Kumnick, H.H. Johnson, Metall. Trans. 5 (1974) 1119.

Instructions for Authors

Submission of Papers

Manuscripts (original and two clear copies) should be submitted to one of the Editors:

for authors in the Americas

Dr. B. D. Sartwell, Surface Chemistry Branch, Naval Research Laboratory, Code 6170, Washington, DC 20375, USA;

and for authors elsewhere

Professor A. Matthews, Director, The Research Centre in Surface Engineering, The University of Hull, Cottingham Road, North Humberside, HU6 7RX, UK.

Contributions are accepted on the understanding that the authors have obtained the necessary authority for publication. Submission of a manuscript implies that it is not under consideration for publication elsewhere.

Types of contributions

— original papers
— invited or contributed reviews on specific topics
— brief communications on topics of immediate interest
— notices of meetings, symposia and short courses
— technical notes for "Current Industrial Practices" section

Languages

Papers will be published in English. Both English and US spelling are permitted, provided that spelling is consistent within an article.

Authors in Japan please note that information about how to have the English of your paper checked, corrected and improved (*before submission*) is available from: Elsevier Science K.K., Editorial Service, 1-9-15 Higashi Azabu, Minato-ku, Tokyo 106-0044, Japan; Tel.: +81 3 5561 5032; Fax: +81 3 5561 5045.

Manuscript preparation

Three copies of the manuscript should be submitted, in double-spaced typing on pages of uniform size with a wide margin on the left.

Some flexibility of presentation will be allowed but authors are urged to arrange the subject matter clearly under such headings as Introduction, Experimental details, Results, Discussion etc. Each paper should have an abstract of 100–200 words.

References should be numbered consecutively (numerals in square brackets) throughout the text and collected together in a reference list at the end of the paper. Journal titles should be abbreviated according to the Chemical Abstracts Service Source Index, 1970 edition, and supplements. The abbreviated title should be followed by volume number, year (in parentheses) and page number.

Submission of electronic text

The final text should be submitted on a 3.5 in or 5.25 in diskette (in addition to a hard copy with original figures). Double density (DD) or high density (HD) diskettes formatted for MS-DOS or Apple Macintosh compatibility are acceptable, but must be formatted to their capacity before the files are copied on to them. The files should be saved in the native format of the wordprocessing program used. Most popular wordprocessor file formats are acceptable. It is essential that the name and version of the wordprocessing program, type of computer on which the text was prepared, and format of the text files are clearly indicated.

Illustrations

Line drawings and cyclic or aromatic formulae should be in a form suitable for reproduction. They may be drawn in black ink on drawing paper (letter height, 3–5 mm), but the use of good quality computer-generated figures is encouraged. They should preferably all require the same degree of reduction, and should be submitted on paper of the same size as, or smaller than, the main text to prevent damage in transit. Photographs should be submitted as clear black-and-white prints on glossy paper. Each illustration must be clearly numbered.

Illustrations can be printed in colour when they are judged by the Editor to be essential to the presentation. The publisher and the author will each bear part of the extra costs involved. Further information concerning colour illustrations and the costs to the author can be obtained from the publisher.

Legends to the illustrations must be submitted in a separate list.

All tables and illustrations should be numbered consecutively and separately throughout the paper.

Proofs

Authors will receive proofs, which they are requested to correct and return as soon as possible. No new material may be inserted in the text at the time of proofreading. All joint communications must indicate the name and full postal address of the author to whom proofs should be sent.

Further information

All questions arising after the acceptance of manuscripts, especially those relating to proofs, should be directed to: Elsevier Science Ireland Ltd. Bay 15K, Shannon Industrial Estate, Shannon, Co. Clare, Ireland; Tel.: +353 61 471944; Fax: +353 61 472144.

The full and complete instructions to authors can be found on the World Wide Web: please visit our website which is accessible via the Elsevier Surfaces and Interfaces HomePage at http://www.elsevier.nl/locate/surfaces

Offprints

Twenty-five offprints will be supplied free of charge to the author(s). Additional offprints can be ordered at prices shown on the offprint order form which accompanies the proofs.

Radiation Effects and Defects in Solids, 1993, Vol. 25, pp. 00–00
Reprints available directly from the publisher
Photocopy permitted by license only

PULSED ION IMPLANTATION OF NITROGEN IN PURE TITANIUM

J. N. FEUGEAS AND G. SANCHEZ, C. O. DE GONZALEZ,
J. D. HERMIDA and G. SCORDIA

Instituto de Fisica Rosario (CONICET-UNR). Bv. 27 de Febrero 210 Bis, 2000 Rosario, Argentina, Comision Nacional de Energia Atomica, Av. del Libertador 8250, 1429 Buenos Aires, Argentina

(Received 5 October 1991)

High current, short length ion beam pulses appear to be a new alternative for surface property modification of solids, due to the combined effect of ion implantation with induced fast heating-cooling which this process presents. The repetitive pulsed nitrogen implantation (with a low energy plasma focus) of pure titanium with different pulse lengths (300 and 400 ns), and fluences per pulse ranging between 1.4×10^{14} and 1×10^{15}cm^{-2}, with total accumulated fluences between 7×10^{14} and 1.6×10^{16} showed a surface heating effect with important compositional and physical changes in the layers close to the surface.

XPS analysis showed $TiN_{0.8}$ formation independent of the total range of fluences used, with an increase in the superficial microhardness, when short pulse lengths were used. A correlation between the N/Ti concentration ratio, the binding energy difference ($Ti_{2p3/2}$-N_{1s}) and the x value in the stoichiometry of the TiN_x compound formed was observed for the long pulse length case.

Keywords: ion implantation—surface modification of solids—titanium—titanium nitride—XPS analyses—pulsed ion beams

INTRODUCTION

Ion implantation as a surface modification method has been used for many years in the microelectronic industry. More recently its field of application has been extended successfully to metallurgy with a large variety of processes where its use has become routine.

Nevertheless, continuous research in this field is still under way permitting discoveries in surface material property modification, new potential applications and also novel methods for ion implantation and related physical processes.[1,2]

The introduction of some atomic species into metal surfaces ~1 μm deep, permits superficial property modification without the characteristic bulk modifications of the material. In addition, a continuous interphase is generated between the superficial implanted layer and the unaltered material bulk, which does not present the adherence problems of other methods for surface treatment such as with thin film coatings. The basic problem consists of the adequate selection of the couple matrix-dopant plus the implantation conditions for obtaining certain desirable results in the surface modification of its properties, such as hardening, wear reduction, better resistance to corrosion, better fatigue resistance, etc.

Titanium, due to its light weight and high mechanical resistance, is of great interest in many industrial applications: aeronautical, biomedical (surgical implants) and nuclear (nuclear fusion reactor) areas. The possibility of titanium surface property improvement considering wear, hardness, corrosion, etc., without its bulk perturbation is of great importance. In this work we present the first results of ion implantation of nitrogen in pure titanium, using pulsed ion beams.

EXPERIMENTAL

Samples of T60 grade commercial titanium, with measured impurities of C: 0.10; 0: 0.40 and Fe: 0.35 % at. respectively, of $7 \times 14 \times 1$ mm, were surface prepared for ion implantation and surface analysis. The samples were mechanically polished with SiC paper and then electrolitically polished in lactic acid, SO_4H_2 and FH (50:20:30) mixture at 0°C with an applied voltage of 15 V for approximately ten minutes.

Nitrogen ion implantation was carried out with the pulsed ion beam accelerator BD-I (low energy plasma focus) of Instituto de Física Rosario described elsewhere.[3] This system provides a sequence of single beam pulses with a fluence f and time length Δt. A preselected total fluence can be obtained by the accumulation of a determined number of single pulses. The time lapse between pulses can be adjusted for any value greater than one second. The beam ions have an energy E which follows a continuous energy spectral law given by $dn/dE \sim E^{-3.4}$, where n is the number of ions with energy E ($E \geq 20$ keV).

In our work we used two different time length Δt and fluences f per pulse. **'A'** type samples were implanted with $\Delta t \sim 300$ ns and $f \sim 1 \times 10^{15} cm^{-2}$; and **'B'** type samples with $\Delta t \sim 400$ ns and $f \sim 1.4 \times 10^{14} cm^{-2}$ ion pulses respectively. The time lapse between pulses in all cases was ≥ 20 seconds. **'A'** type samples were implanted with total (accumulated) fluences of 0.1, 0.3, 0.5, 1.0 and $1.3 \times 10^{16} cm^{-2}$ respectively. **'B'** type samples were implanted with a total fluence of $7 \times 10^{14} cm^{-2}$.

The fast energy release on the target surface due to the short duration of the ion beam pulse competes with the equally fast heat conduction to the sample's bulk, generating high temperatures, strong temperature gradients in the surface layers and fast temperature variation in time[4] These effects may provoke the modification of the implanted species concentrations (from the preceedings pulses) due to diffusion processes, and also in some cases the superficial layer melt down. This thermal effect is added to the single ion implantation one for the resulting nitrogen concentration profile, marking a difference with low current (cold) ion beam implantation processes.

The acceleration process maintained in this device (BD-I) is originated during the collapse of a high current plasma column (due to Rayleigh-Taylor instability development). This high current filament of plasma (Plasma Focus) is generated in a focuzed coaxial discharge in a 0.2 Torr nitrogen gas atmosphere. This 0.2 Torr nitrogen environment is also the environment of the samples exposed to the ion beams. As a consequence of the plasma column collapse, in addition to the beam generation, a secondary plasma bubble with low energy associated particles (ions and electrons) is ejected. This low energy plasma reaches the sample's surface after the beam, acting for several microseconds (~3 μs)[5] The implanted samples were characterized using X Ray Photoelectron Spectroscopy (XPS) and X Ray Diffraction (XRD) techniques.

The XPS spectra were taken with an ESCA 3 MARK II Spectrometer (V. G. Scientific Limited) calibrated by assuming the binding energy (BE) of the $Au_{4f_{7/2}}$ peak at 83.9 eV with respect to the Fermi level. The Mg kα line without monochromatizing (1253.6 eV) was employed as incident radiation. The depth profiles were obtained by alternating sputtering with A^+ ions (5keV, 10 $\mu A/cm^2$) and measurements of the XPS spectra. The erosion rate was estimated to be 10 Å/min.

The XRD analysis was performed by a standard Philips Diffractometer with a horizontal goniometer. Cokα radiation and a graphite monochromator in the diffracted beam were used.

RESULTS

Surface Morphology

The surfaces of the implanted samples were observed with a scanning electron microscope (SEM). Observations of the 'A' type implanted samples show the existence of folds, craters and fissures distributed across the whole implanted region.

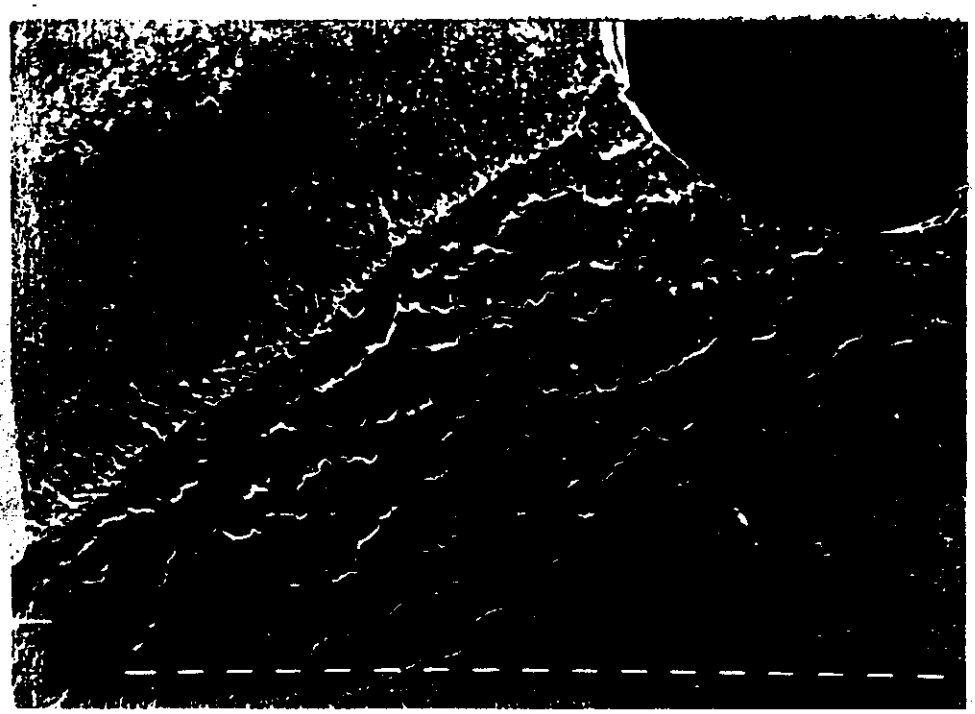

FIGURE 1 Scanning Electron Microscope photograph of an A Type implanted sample partially covered with a titanium foil. a) correspond to the non-implanted region (covered by the foil), and b) correspond to the nitrogen implanted region (uncovered).

In Figure 1 two regions of the same sample, region 'a' non implanted and region 'b' implanted, can be seen. The sample corresponds to an 'A' type implanted one, but partially covered with a 200 μm thick titanium foil. The whole implanted (uncovered) region has a wavy surface, showing the general appearance of a thin superficially molten layer. This hypothesis is confirmed by observation of Figure 2, where solidified drops of molten titanium, flowing during the fast energy deposition process of the ion pulse, can be seen in the edge of an implanted sample.

FIGURE 2 Scanning Electron Microscope photograph of an A Type implanted sample. The image corresponds to the edge of the sample, with the implanted surface slightly tilted to observe the frozen drops of melted titanium against the background of the (non implanted) sample edge.

Microhardness Measurements

The microhardness of implanted 'A'-type samples were studied for different fluences. The measurements were performed with an applied load of 20 g. The results were presented in Table I. Taking into account the fact that the indentation size was of the same order of magnitude as the affected thickness of the implantation, the measured microhardness corresponded to the implanted layer, the interphase and part of the unaltered substrate.

Nevertheless, the systematic higher values obtained in the implanted surfaces revealed a resulting hardness attributable to the nitrogen implantation.

TABLE I
HV microhardness (Kg/mm^2) of pure titanium and 'A' type implanted samples with different nitrogen fluences. Applied load: 20 g.

FLUENCE ($\times 10^{18}$cm^{-2})	non-impl.	0.1	0.3	0.5	1.0	1.3
MICROHARDNESS HV (kg.mm^{-2})	230	266	309	264	455	404

DRX Results

The Ti peaks of the irradiated samples in the 'A' conditions, appeared considerably broadened in relation to the ones of non-implanted samples. Furthermore, there was a significant change in the intensity ratio between different peaks. For the reference (non-implanted) sample, these ratios correspond to the usual (0002) rolling texture of HCP materials, while all the 'A' type irradiated samples correspond to a situation of random orientation of the grains. Instead, 'B' type samples maintained the rolling texture after implantation.

Also, other low intensity and very broad peaks, which do not correspond to the Ti diffraction pattern were detected. These peak intensities were higher for the samples irradiated with higher fluences, which means an increasing concentration of compounds. According to the d_{hkl} values, this can be assigned to several allotropic forms of TiO and Ti_8O_{15}. Nevertheless, there was no coincidence with the d_{hkl} Ti nitride values.

XPS Analysis

The atomic concentration of the surface elements was determined through XPS analysis using the calculation method described elsewhere.[6] High resolution narrow spectra of N_{1s}, Ti_{2p}, O_{1s} and C_{1s} were taken at different depths.

At the surface, the O_{1s} and C_{1s} signals were rather important. The C existence can be attributed to atmospheric contamination, and can be eliminated by ion sputtering showing that it consists of a very thin layer. The O_{1s} signal instead, is formed by two contributions: adsorbed oxigen (B.E. = 532.0 ± 0.1 eV) and oxides (B.E. = 530.4 ± 0.1 eV). The former, like C, is very superficial and can be eliminated by a few minutes of argon sputtering; however, the latter remain along the whole analyzed depth. The oxigen concentration varied in different samples between 7 and 14 atomic percent, depending on the implantation conditions.

In 'A' type samples, the atomic concentration of Ti (~48%at.) and N (~43%at.) and then its concentration ratio N/Ti (~0.9) remain constant throughout the 3000 Å deep layer analyzed, and for each of the fluences used.

Figure 3 shows the concentration depth profile for a 'B' type implanted sample. The XPS analysis in this case was carried out deeper within the sample in order to determine

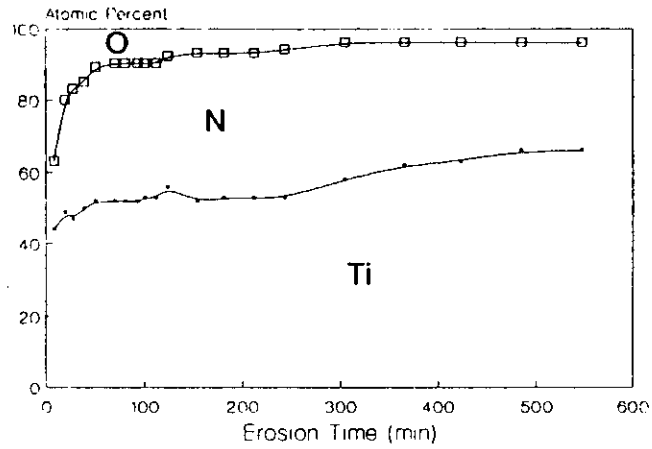

FIGURE 3 XPS analysis of the element concentration (atomic percent) with depth (argon erosion time) for a B Type implanted sample. One minute erosion corresponds to approximately 10 Å depth.

TABLE II
Binding energies of $Ti_{2p3/2}$ and N_{1s} peaks (eV). Analyzed depth: 2500Å

SAMPLE	$Ti_{2p3/2}$	N_{1s}	Δ ($Ti_{2p3/2}$—N_{1s})
TYPE 'A'	454.7	397.0	57.7
TYPE 'B'	454.5	397.0	57.5
PURE TITANIUM	453.8	399.0	54.8

the thickness of the implanted region. The N concentration (39%at.), lower than in the A sample cases, remains constant over the first 2400 Å. Below this depth, the concentration start to decrease reaching a 28%at. at 5400 Å, which corresponds to a N/Ti ratio variation between 0.75 and 0.5.

The binding energies of the $Ti_{2p3/2}$ and N_{1s} XPS peaks for implanted and non implanted samples are listed in Table II. The measured binding energies were the same for A samples, for all of the used fluences, remaining the N_{1s} peak in 397.0 ± 0.1 eV along the analyzed depth also for any of the used conditions. The chemical shift with respect to the pure elements indicates the nitride formation and, in low quantity, titanium oxides.

DISCUSSION

The analysis of the 'A' type samples (short time implantation pulses) by SEM revealed that the surfaces were severely damaged, as a consequence of surface melting. This effect, studied elsewere[4,7] can be explained by the fast energy release of the ion beam pulse, which is very sensitive to the implantation pulse length. This fast energy release provokes a fast temperature increase, followed by a fast cooling down through thermal conduction to the sample's bulk. This process orginates typical temperature gradients during the heating of ~1500 K/μm, and temperature evolution of ~15 K/ns and 5 K/ns during heating and cooling respectively.[4] The 20 second lapse time used between pulses during implantation, is long enough to ensure complete thermal relaxation of the sample. Consequently, for samples with sufficiently large masses, each ion beam pulse will find the surface at room temperature, initiating each time a new thermal cycle.

In fact, XRD measurements confirm the hypothesis of the surface melting because of the loss of the initial rolling texture, and the random orientation of the grains after implantation. Besides, the broadening of the XRD peaks can be attributed to the high microstrain concentration[8] originated by the interaction between the molten region and the unaffected grains during the cooling.

Looking at the nitrogen concentration, it can be seen from one side, that it is independent of the fluence in implanted 'A' type samples, and on the other, that their values are several times higher than those which can be deduced from the used fluences.

The independence of nitrogen concentration with the fluence (in 'A' type samples) differs from the results published by Takano *et al.*[9] in which they show a nitrogen concentration increasing with the fluence. Nevertheless they work with a low current, monoenergetic (60 keV) ion beam which does not present the fast heating-cooling process observed in our pulsed case. The possible reason for this difference can be attributed to the diffusion process induced by the strong temperature gradient generated during implantation.[10] This process can redistribute, in each pulse, the nitrogen implanted in the preceeding ones, inducing uniformity in the nitrogen concentration profile at least in the first analyzed 3000 Å.

A higher nitrogen concentration than the expected for the ion beam fluences used, can be attributed to the specific nature of the ion beam generation with plasma focus devices.

The low energy plasma bubble generated during the ion beam acceleration in the focus[5] arrives immediately after the ion beam reaching the target when it is still at high temperature. Normally this plasma does not perturb the target surface due to its low energy, as can be seen in the results of nitrogen implantation in steels.[5] Nevertheless, in our case where the sample material is titanium, the 'getter' effect of it over nitrogen provokes the nitrogen absorption which only will be finished by its eventual saturation. Successive implantation pulses (followed in each case by the plasma bubble) will help, by diffusion, the nitrogen migration deeper into the sample. It can be assumed that the nitrogen concentration will be as important as the thermal effect will become upon deepening.

The binding energy of the N_{1s} peak (397.0 eV) shows a 2 eV chemical shift through lower energies with respect to the pure element, coinciding with the energy position corresponding to nitrides of several elements.[11]

The $Ti_{2p_{3/2}}$ conserves its maximum at 454.7 eV for each of the 'A' type samples, with a slightly diminishing value for the 'B' type samples (Table II), where coincidentally, the nitrogen concentration is lower.

In the transition elements the nitrides, carbides and oxides can exist in a wide range of stoichiometries. Particularly the TiN_x can be obtained with $0.5 \leq x \leq 1.1$. This variety can be determined by the different chemical shifts induced by the different degrees of charge transfer among both elements.

Porte[12] worked on the systematic XPS study of the energetic positions of TiN_x compounds prepared in a wide range of stoichiometries. In his work he considered the ΔEb difference of binding energies between the $Ti_{2p_{3/2}}$ and the N_{1s} photopeaks, as more informative of the variations of the charge transfer, rather than the core-level shift. For the TiN ($x = 1$) stoichiometry, $\Delta Eb = 58.3$ eV, with increasing values for increasing values of x, reflecting the increase of charge transfer from Ti to N.

For the purpose of stoichiometric identification of the formed compound, we calculate the ΔEb values for the 'A' and 'B' type implanted samples. In the fourth column of Table II, the ΔEb values measured at 2500 Å are listed. For the 'A' type case, and for each fluence studied, the good definition of the $Ti_{2p_{3/2}}$ peak for different depths, such as the constant value measured for ΔEb, allows us to suppose the existence of a unique stoichiometric compounds TiN_x, with $x = 0.8$. The fact that this compound is largely found at all depths analyzed, matches well with the concentration rates N/Ti being constant with depth.

The constant nitrogen concentration (N/Ti ~ 0.9) observed for each of the totally accumulated fluences used for the 'A' type implanted samples, can be explained throughout the molten layer which, when overheated and with strong thermal gradients, can help the diffusion process (Soret diffusion) of the nitrogen, from the layers closer to the surface to deeper levels. This process occurs in each pulse and works on the concentration profile generated in the preceeding ones.

Also observed was a substoichiometric $TiN_{0.8}$ formation, which approaches the TiN composition. These nitridings are normally used for hard coating deposition,[13] and can be considered responsible for the observed hardening of the surface in our case. In spite of the thin layer affected by the ion implantation (some order of magnitude as that of the indentation size left in the microhardened measurement), which means that the measured microhardened area was affected by the substrate, the systematic higher values found indicate the development of a harder layer. The tendency toward an increase in microhardening with fluence (Table I), in spite of only one substoichiometric nitride formation and the missing variation in nitrogen concentration, can be attributed indeed to a possibly thicker affected layer.[14] This effect of deeper penetration could be the result of the successively induced thermal gradient diffusion processes per pulse, taking into account the correlation between total fluence and number of pulses. For the 'B' type case, Figure 4 represents the ΔEb variations with depth. Its value remains constant (57.5 eV) from surface

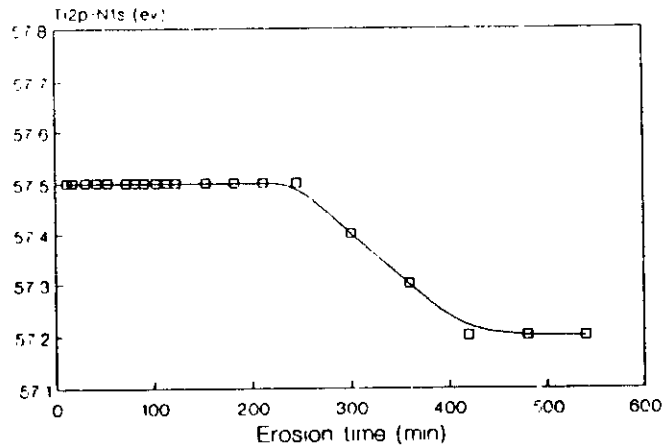

FIGURE 4 The difference in binding energies of the $Ti_{2p_{3/2}}$ and N_{1s} photopeaks (XPS) for the same sample of Figure 3, are plotted as a function of depth (argon erosion time). One minute of erosion time corresponds to approximately 10 Å depth.

to ~2400Å. Then it continuously decreases reaching a value of 57.2 eV at ~4200 Å depth. This behaviour is similar to that of the concentration ratio N/Ti, making evident the correlation between ΔEb and the stoichiometry. In this case, the ΔEb values[12] give a TiN_x stoichiometry with $x = 0.7$ for the surface layer, decreasing to $x = 0.5$ for deeper levels.

CONCLUSIONS

In pulsed ion implantation processes in general, the thermal effect is of great importance for the final properties of the implanted layers. In the case of the ion beams accelerated in plasma focus discharges, the plasma bubble generated by the beams, which normally do not perturb the surface target due to its low energy, can play an important role in getter materials like titanium. This effect can be seen in our case by the resulting nitrogen concentration, well above the levels which can be expected from the ion beam fluences used.

Also, the high temperature and thermal gradients generated in this case, allow for improvement in the uniformity of the nitrogen concentration, being deeper within the sample than after low current implantation processes.

On the other hand, nitrogen rich nitridings as high as $TiN_{0.8}$ can be obtained with relatively low implantation fluences. Such nitridings are responsible for surface hardening.

Finally, the correlation observed between the N/Ti concentration ratio and the increasing x in the stoichiometry of the developed TiN_x shows the possibility of hardening the surface layers at deeper levels.

The possibility of combining pulse length (temperature) with fluences, adds an attractive perspective for surface modification of materials to the pulsed ion implantation method.

ACKNOWLEDGEMENTS

We are grateful to S. Hild for his help in XPS measurements. Work partially supported by the IAEA under Research Contract No. 6477/RB, and the ICTP (Trieste, Italy) under TWAS Grant Contract No. MP 90-090.

REFERENCES

1. G. Dearnaley. Surface Engineering, 7, 127 (1991).
2. L. Guzman, G. K. Wolf and P. P. M. Procter, editors. 'Surface Modification of Metals by Ion Beams 6'. Vol. I and II. Elsevier Science Publishers. London and New York (1989).
3. J. Feugeas, E. Llonch, C. O. de Gonzalez and G. Galambos. *J. Appl. Phys.* 64, 2648 (1988).
4. J. Feugeas and G. Sanchez. Proc. IV Latinoamerican Workshop on Plasma Physics. (Organizers: Comision Nacional de Energia Atomica, Secretaria de Ciencia y Tecnica, International Atomic Energy Agency) Buenos Aires, Argentina. pp. 158 (1990).
5. W. Bostick, V. Nardi, J. N. Feugeas and W. Prior. Energy Storage, Compression and Switching. Vol. 2., 267. Plenum Press. New York and London. (1978).
6. C. O. de Gonzalez and E. A. Garcia. Anais do Coloquio Latinoamericano de Fisica de Superficies. Niteroi, Brasil. 203 (1980).
7. J. Piekoszewski, Z. Werner, J. Langner, L. Jakubowski, C. Poclrybniak and A. Harasiewicz. *Nuclear Instruments and Methods* 209/210, 477 (1983).
8. A. A. Pochettino, J. Feugeas, M. Ortiz and G. Sanchez. Proc. 3rd. International Conference on Residual Stresses. ICRS-3, Tokushima, Japan. (1991, in press).
9. I. Takano, S. Isobe, T. A. Sasaki and Y. Baba. *Appl. Surf. Science* 37, 25 (1989).
10. E. Rimini: in 'Surface Modification and Alloying by Laser, Ion and Electron Beams' (eds. J. M. Poate, G. Foti and D. C. Jacobson). Cap. 2, p. 15 (1983). NATO Conference Series. Plenum Press. New York and London.
11. B. M. Biwer and S. L. Bernasek. *J. Electron. Spectrosc. Relat. Phenom.* 40, 339 (1986).
12. L. Porte, L. Roux and J. Hanus. *Phys. Rev.* B28, 3214 (1983).
13. M. E. O'Hern, R. H. Parrish and W. C. Oliver. *Thin Solid Films*, 181, 357–363 (1989).
14. A. Thomas. Surface Engineering, 3, 2, 117 (1987).